



UNIVERSITÀ DEGLI STUDI DI MILANO

DEPARTMENT OF <DEPT OF UNIMI>

PHD SCHOOL IN
PHYSICS, ASTROPHYSICS AND APPLIED PHYSICS
CYCLE XXXV

Characterization of Non-Equilibrium Fluctuations during free-diffusion in highly- stratified solutions of glycerol and water

Disciplinary Scientific Sector < FIS/R17 >

PhD Thesis of:
Stefano Castellini

Director of the School: Prof. Matteo Paris
Supervisor of the Thesis: Prof. Alberto Vailati
Co-Supervisor of the Thesis: Prof. Marina Carpineti

A.Y. 2022-2023

Acknowledgements

I ringraziamenti bisogna farli bene o non farli. Dovrei fare mente locale di tutte le persone che in questi anni di dottorato mi sono stati vicini, mi hanno supportato. Devo dire che pensarci mi riempie di silenzio. Però mettermi a scrivere i nomi e cognomi della mia famiglia, tutta (anche Fabio dai), degli amici (me ne vengono in mente più di 100), Chiara (che è quasi in entrambe queste categorie), dei professori e colleghi... Insomma verrebbe fuori un elenco molto lungo. E sicuramente qualcuno rimarrebbe fuori. Tipo Gloria. E allora? Vi dedico una poesia, sapendo che se stai leggendo qui, siamo più che amici:

*Giù nello Stretto le onde schiumano
 come dicono qui. Il mare è mosso e meno male
 che non sono uscito. Sono contento d'aver pescato
 tutto il giorno a Morse Creek, trascinando avanti
 e indietro un Daradevil rosso. Non ho preso niente.
 Neanche un morso. Ma mi sta bene così. È stato bello!
 Avevo con me il temperino di tuo padre e sono stato seguito
 per un po' da una cagnetta che i padroni chiamavano Dixie.
 A volte mi sentivo così felice che dovevo smettere
 di pescare. A un certo punto mi sono sdraiato sulla sponda
 e ho chiuso gli occhi per ascoltare il rumore che faceva l'acqua
 e il vento che fischiava sulla cima degli alberi. Lo stesso vento
 che soffia giù nello Stretto, eppure è diverso.
 Per un po' mi son lasciato immaginare che ero morto
 e mi stava bene anche quello, almeno per un paio
 di minuti, finché non me ne sono ben reso conto: Morto.
 Mentre me ne stavo lì sdraiato a occhi chiusi,
 dopo essermi immaginato come sarebbe stato
 se non avessi davvero potuto più rialzarmi, ho pensato a te.
 Ho aperto gli occhi e mi sono alzato subito
 e son ritornato a esser contento.
 È che te ne sono grato, capisci. E te lo volevo dire.*

di Raymond Carver

Me la fece leggere un amico qualche anno fa. Mi stupì molto e descrive quello che provo nel pensarvi.

A Chiara, sarà una moglie paziente

Chapter 1

Introduction

This PhD thesis aims to present the research results obtained during the doctoral years in the field of non-equilibrium fluctuations.

The first objective of this work was to thoroughly characterize non-equilibrium concentration fluctuations that occur during isothermal processes of free diffusion. While non-equilibrium fluctuations in ideal systems (steady states, thin samples, small concentration gradients [90], [27]) are well-understood, this work focuses on investigating fluctuations in strongly non-ideal samples. The theoretical modeling of non-equilibrium fluctuations in the presence of large density gradients is challenging because an analytical description of the static and dynamic statistical properties of the fluctuations is not possible under these conditions. However, studying non-equilibrium fluctuations under these non-ideal conditions is crucial as most natural and technological diffusion processes occur under transient non-ideal conditions with large gradients.

The second objective was to gather preliminary measurements for studying fluctuations in nonisothermal systems, specifically during thermodiffusion. The investigated sample was a thermophilic suspension of nanoparticles heated from below. This case is particularly interesting due to the competing effects of the stabilizing flow induced by thermophoresis and the destabilizing flow caused by thermal convection and sedimentation processes, resulting in a complex stability diagram. The analysis of the interaction between these flows led to the discovery of a new traveling wave solution characterized by an anharmonic distribution of vertical velocity through the sample layer. In this thesis, we demonstrate that such propagating waves generate states that rapidly rotate around their axis and

gradually decrease in size until the system returns to a purely conductive flow-free state. The study of these spatially localized states is highly relevant in the field of pattern formation as they appear in various physical and biological systems [4], [47]. In the case of localized stationary convective states, they are referred to as convectons, and extensive research has been conducted on them from theoretical, computational, and experimental perspectives [53]. Furthermore, this study will enable us to explore non-equilibrium fluctuations in the absence of fluxes caused by these instabilities in future research.

During my doctoral studies, I also investigated the formation of convective patterns in an inclined layer of liquid water with poorly thermally conductive boundaries [16]. Although this study is not the main focus of my thesis, I will briefly summarize its key findings in this general introduction. The first significant discovery was that, above the convection threshold, a tilt greater than 14 mrad leads to a transition from a square pattern to longitudinal rolls. This behavior contrasts with the observed transitions between convective forms in the presence of inclined conductive boundaries, where the tilt angles are typically a few degrees. Additionally, longitudinal rolls were characterized, and a dimensionless wave vector of approximately 1.8 was observed, significantly smaller than the value of approximately 3.117 reported for large Prandtl number conducting boundaries. It was also observed that the transition between the two patterns (squares and rolls) can be triggered by dynamically changing the inclination of the fluid layer, and this transition is not symmetrical in the two directions. When starting from the horizontal configuration, the transition slowly progresses by demolishing the square structure and forming longitudinal rolls. Conversely, in the opposite direction, the transition rapidly progresses by forming a cross-roll structure perpendicular to the longitudinal rolls. While these results are not extensively discussed in my thesis, they are included for completeness and to provide an overview of the overall research conducted during my doctoral studies.

In this introduction, it is useful to contextualise the main phenomenon studied, starting with the fluctuations that occur in fluids at equilibrium. The theory of fluid fluctuations in thermodynamic equilibrium is well-established, as documented by [7]. Specifically, the magnitude of density fluctuations is directly proportional to the isothermal compressibility, while the intensity of concentration fluctuations in mixtures is proportional to the osmotic compressibility.

Moreover, the Onsager's regression hypothesis governs the decay of thermally-induced fluctuations. This hypothesis asserts that the rates of decay of fluctuations are determined by transport coefficients, which appear in the linear relationships between gradients and fluxes in out-of-equilibrium thermodynamics. Landau's fluctuating hydrodynamics provides a theoretical framework for investigating fluid fluctuations in thermodynamic equilibrium, as detailed by [50, 36]. Finally, light scattering and neutron scattering can be employed experimentally to investigate these fluctuations, as reported by [62].

In addition to equilibrium fluctuations, the scientific community has also extensively investigated Non-Equilibrium Fluctuations (NEF). The nature of thermal fluctuations in fluids and fluid mixtures that exist in states of thermodynamic non-equilibrium is a fascinating topic. It is known that non-equilibrium fluids can exhibit significant fluctuations associated to convection or turbulence patterns. However, a relatively new research topic is the investigation of fluctuations in fluids subjected to temperature gradients or shear, in the absence of convective patterns or turbulent flows.

About 70 years ago, Bogoliubov proposed a microscopic model for non-equilibrium phenomena in fluids [6]. According to his postulate, a fluid far from equilibrium would proceed towards a state of thermodynamic equilibrium in two phases. The first phase is a microscopic kinetic phase, which occurs on a time scale equivalent to the time between molecular collisions, which is of the same order as the duration of molecular collisions, particularly for dense or liquid fluids. In this phase, a local equilibrium is established. The second phase is a macroscopic hydrodynamic phase, during which the fluid evolves according to the hydrodynamic equations.

Implicit in this postulate is the idea that in a fluid of molecules with short-range forces there are no long-range dynamic correlations, unless the system is close to incipient thermodynamic or hydrodynamic instability.

The field of non-equilibrium statistical physics has revealed a flaw in the conventional understanding of molecular collisions. In this field, there are physical quantities such as mass, momentum and energy that are conserved during collisions, while there are others that behave differently and do not obey any local conservation laws. However, through various research, it has been discovered that the slow hydrodynamic modes associated with conserved quantities and the

fast modes associated with non-conserved quantities can interact and cause coupling between modes that results in long-range dynamical correlations.

This contradicts the traditional understanding of short-range dynamic correlations in fluids near the critical point, which proved insufficient when experiments revealed divergent thermal conductivity that could not be explained by Van Hove's theory of critical slowing of fluctuations based on thermodynamic considerations [72]. This observation led to the development of various theories based on the link between slow hydrodynamic modes and microscopic quantities known as "mode-coupling theory" [44].

In the 1980s, it was discovered that the mode-coupling theory predicted the existence of long-range fluctuations in fluids maintained in non-equilibrium steady states. This discovery was made by [46] and was later supported by other researchers such as [66], [79]. Specifically, when a fluid is subjected to a gradient of a given thermodynamic variable, e.g. concentration or temperature, this gradient generates a coupling between the component of the velocity fluctuations parallel to the gradient and the fluctuations of the thermodynamic quantity of which a gradient was created, leading to an algebraic divergence of the amplitude of fluctuations in the limit of small wave numbers (large spatial scales). This phenomenon is now considered a general feature of fluctuations in fluids in non-equilibrium steady states and is a manifestation of a general principle of generic scale invariance in non-equilibrium statistical mechanics. On Earth, the divergence of the intensity of non-equilibrium fluctuations for small wave numbers, i.e. for large wavelengths, in the presence of temperature or concentration gradients is prevented by gravity and finite size effects. Therefore, gravity and finite size effect play an important role in the wave-number dependence of fluctuations in fluids in non-equilibrium states [71, 81, 83]. Specifically with regard to gravity, if the region of a fluid affected by the velocity fluctuations is sufficiently large, buoyancy will return it to the same density layer from which the fluctuation originated, before the fluctuation gets dissolved by diffusion. Regarding this, experiments have been conducted in the absence of gravity and it has been discovered that the divergence of fluctuations is only inhibited by the physical size of the fluid itself in this case [84, 76, 31]. The GRADFLEX project of the European Space Agency (ESA) and the National Aeronautics and Space Administration (NASA) has provided convincing evidence that linearised hydrodynamics can accurately model the static and dynamic properties of fluctuations

under *ideal* non-equilibrium conditions, for example in steady-state diffusion processes driven by small macroscopic density gradients.

Recently, theoretical progress has been made also in the study of the role of giant fluctuations in high Schmidt number turbulent flows at the sub-Kolmogorov scale [34]. Using Kraichnan's model of turbulent advection, exact modelling of non-linear advection of concentration fluctuations has revealed that the static and dynamic structure functions exactly reproduce those obtained from linearised hydrodynamics [35]. Traditional calculation methods cannot be applied to simulations of non-equilibrium fluctuations due to the presence of a number of length and time scales spanning several orders of magnitude. However, over the past 15 years, the solution to this difficult problem has come through the development of staggered schemes based on the hydrodynamics of fluctuations [80]. Recently, these methods have been extended to non-isothermal systems, thus enabling the computational investigation of non-equilibrium fluctuations driven by Soret and Dufour effects [75].

In addition to theoretical nonlinear modelling, a quantitative understanding of non-equilibrium fluctuations under non-ideal conditions can be achieved through experiments and simulations. The European Space Agency's Giant Fluctuations and TechNES projects aim to explore non-equilibrium fluctuations in complex fluids during diffusion processes under microgravity conditions. These projects focus on examining transient and stationary processes in multi-component fluids, which on Earth face stability challenges due to the occurrence of double diffusion processes that lead to the onset of convective motions, even when an initially stable density profile is present.

The main topic of my work concerns the study of non-equilibrium concentration fluctuations during diffusion in water-glycerol mixtures subjected to strong concentration gradients. The thermophysical properties of a fluid mixture depend on its concentration, therefore, in the presence of strong stratification, non-linear terms appear in the diffusion equation. This results in a superposition of modes with different amplitudes and relaxation times arising from different fluid layers at any given wave number. To study non-equilibrium fluctuations, static and dynamic light scattering techniques are generally used, including recently developed near-field techniques [18] such as Near Field Scattering [42], Dynamic Shadowgraphy [30] and Differential Dynamic Microscopy [17]. These

optical methods work by illuminating the sample with a light beam and collecting scattered light from the sample on a matrix sensor. The light collected by the sensor is scattered by the sample the superposition of the contributions of the light scattered by the different layers of the sample, which can be characterised by different thermophysical properties depending on the local concentration.

In the presence of a small concentration gradient, the dependence of thermophysical properties on concentration can be neglected, but for larger gradients, the analysis of experimental data obtained with scattering techniques requires non-trivial modelling of the layered fluid properties. As a first approximation, it can be assumed that the contributions from the different layers are uncorrelated and modelling of the scattered intensity can be achieved by integrating the scattered light intensity across the sample thickness [82]. This approximation should be valid when the wave numbers are significantly larger than the finite size wave number $q_{fs} = 2\pi/h$ associated with the finite thickness h of the sample, even in the presence of a significant dependence of thermophysical properties on temperature or concentration [88].

More generally, non-equilibrium fluctuations are also expected to be correlated in the direction parallel to the gradient [10], with a correlation length of the order of $1/q$. Therefore, in order to correctly model scattered light at small wavelengths, it is necessary to take these long-range correlations into account, but this type of discussion is not carried out in this thesis.

In the main part of this study, we conducted experiments in an isothermal configuration with free diffusion. Specifically, we placed two solutions of water and glycerol, each with varying concentrations, in a stable configuration in which the denser mixture occupies the bottom of the sampling cell. To ensure accurate results, we used a three-dimensional junction cell that generated an interface between the two mixing phases free of unwanted disturbances. This method provided us with a unique opportunity to conduct precise experiments and collect reliable data.

The glycerol concentration strongly influences the viscosity and diffusion coefficient of the mixture, resulting in a highly non-linear concentration profile. Consequently, non-equilibrium concentration fluctuations exhibit a wide range of relaxation times at any wave number, leading to a non-exponential relaxation of the time correlation function at a fixed wave number. To solve this problem, we developed an empirical model for the time correlation function of scattered

light. Our analysis shows that the assumption of uniformly distributed relaxation times allows to determine an analytical expression of the time correlation function that provides an accurate description of the deviation from the single exponential relaxation (SE). This finding allowed us to fully describe the dynamics of the system at each wave number in terms of faster and slower relaxation times. We compared our results with traditional particle scaling methods commonly used in Dynamic Light Scattering to characterise the dispersion of relaxation times in polydisperse samples, such as the cumulant analysis and Schulz distribution. This work was recently published in the scientific journal *The Journal of Chemical Physics* [15].

In addition to examining fluctuations in isothermal systems as described above, we have laid the groundwork for studying fluctuations in mixtures subjected to thermal diffusion conditions. In particular, we aim to explore the nonequilibrium fluctuations (NEFs) that occur during thermodiffusion in a thermophilic suspension containing water and Ludox TMA. However, such a suspension is characterized by a complex stability diagram, and to study the fluctuations, it is essential to eliminate any convective instability.

Let us now briefly introduce the study of the stability diagram of a complex solution. This study is of interest because most dynamical processes occur in multiphase systems, and it is not surprising that contemporary problems in continuum mechanics involve the study of volumetrically coupled phenomena in materials with different physical properties, coexisting and operating in the same space. In the past decade, progress has been made in understanding the effects accompanying the flows of solid particles suspended in a continuous liquid medium through the results of numerous research efforts. These efforts are important for fundamental science that focuses on the description, simulation, design, and control of processes in colloids, as well as for the many applications of colloidal mixtures in areas such as the chemical, pharmaceutical, food, cosmetic, wastewater, medical technology, bioprocessing, and environmental engineering industries [43, 58].

A colloidal mixture contains dispersed phase particles with a diameter of about 10-100 nm. Similarly to the instability phenomenon observed for molecular binary mixtures in one of the most studied heat transfer problems (the Rayleigh-Benard problem), in a colloidal mixture layer subject to gravitational segregation

[74] an inhomogeneity of density, and consequently, a volume force that depends on thermal conditions and solid phase distribution, can occur. Thermal diffusion (Ludwig-Soret effect) in turn influences the relationship between concentration and temperature fields and bifurcations in colloidal systems. The great difference between the characteristic times of thermal and diffusive processes accounts for the interesting properties of convection in colloidal suspensions [19].

In convective currents of colloidal suspension with negative Soret number, numerous spatiotemporal structures have been observed. The specific direct motion of a heavy component toward a hot boundary of the layer weakens the buoyancy effect and generates growing oscillatory disturbances, the nonlinear evolution of which generates a variety of regimes. In colloidal mixtures, there is another segregation mechanism in which the heavy component migrates in the direction opposite to gravity. Depending on the initial conditions, the onset of convection can be related to the development of monotonic or oscillatory instability modes. Oscillations in the colloidal mixture have been observed experimentally over a long period of time (about one week) [33].

In addition to the foundation for a study of nonequilibrium fluctuations, recent experimental studies have highlighted the potential of the bistability of nanofluids with large negative separation ratio, such as the one studied in this work, to actively control heat transfer by switching from the conductive to the convective regime (and vice versa) by exploiting the thermophilic behavior of nanoparticles [5]. This work has thus generated another publication [14].

Finally, the thesis is organized as follows: firstly (chapter 2), we present the theory of non-equilibrium fluctuations, focusing on an ideal thin sample with a uniform concentration gradient. Chapter 3 introduces the optical technique used and the algorithms applied for the analysis of images. Chapter 4 proposes a new model for interpreting fluctuations in strongly stratified samples, with accompanying computational confirmations of our theory. In chapter 5, we compare our proposed model with numerical simulations of the ideal model for a thin sample and the Schulz distribution model. Chapters 6, 7 detail the experimental setup, measurement methods, and results of our model applied to the investigated samples. Finally, in chapter 8, we present the stability diagram for a mixture of water and Ludox, which serves as the basis for studying NEFs under temperature gradient conditions.

Chapter 2

Theory of non-equilibrium fluctuations

Out-of-equilibrium fluids exhibit collective behaviour, typical of complex systems, giving rise to various structures. When a non-equilibrium condition is applied to a fluid, such as the one obtained by imposing a temperature gradient, the local thermodynamic variables fluctuate in time around their average value. Actually, this also happens for fluids at equilibrium, but no order appears in this case: the fluctuations take the form of simple white noise, identical at every scale [90]. On the other hand, in the presence of a concentration or temperature gradient, the fluctuations have different mean squared amplitude at different wavenumbers q according to a well-defined scaling law $S(q) = \frac{S_0}{1 + (\frac{q}{q_{ro}})^4}$ [82], where q_{ro} is a characteristic wavenumber that depends on the acceleration of gravity. This is surprising if we think of the random nature of these fluctuations: there is a collective self-organisation in the fluid that determines a long-range order in these fluctuations. In this chapter I will discuss this phenomenon from a theoretical and experimental point of view, showing the most important results found in literature.

2.1 Fluid Dynamic Equations

This section presents the classical fluid-dynamic model, following the steps found in the book [50]. This model is based on two very important assumptions: first, the continuous medium hypothesis, which means that any small volume element

in the fluid is always supposed so large that it still contains a very large number of molecules; second, the local equilibrium hypothesis, which assumes that a system can be viewed as formed of subsystems where the rules of equilibrium thermodynamics apply. In the following paragraphs a Eulerian approach is used, which means that the reference system is fixed externally to the sample and the fluid particles move in these spatial and temporal coordinates. Thanks to these assumptions, we can introduce the three balance equations that describe the system.

2.1.1 Mass Balance Equation

The continuity equation describes the conservation of the mass within the fluid:

$$\frac{\partial \rho(\mathbf{r}, t)}{\partial t} + \mathbf{v} \cdot \nabla \rho(\mathbf{r}, t) = -\rho(\mathbf{r}, t) \nabla \cdot \mathbf{v}(\mathbf{r}, t) \quad (2.1)$$

where $\rho(\mathbf{r}, t)$ is the density that depends on the local position \mathbf{r} within the fluid and at the time t , \mathbf{v} is the local velocity of the fluid. The continuity equation means that the total mass of fluid contained in any volume under consideration can only vary due to the fluid motions that occur on entering or leaving the volume. Equation 2.1 is very general and is always valid for the phenomena we will discuss in this thesis (in the presence or absence of temperature gradients, for simple fluids or binary mixtures, this equation remains valid).

When the fluid under consideration is a binary mixture it is necessary to introduce a mass balance equation for each component. Calling $c(\mathbf{r}, t)_i$ the local concentration defined as the ratio of the mass of a certain species i to the total mass of the mixture contained in a unit volume, it follows directly that $\sum c(\mathbf{r}, t)_i = \frac{m_{tot}}{m_{tot}} = 1$. If the mixture is in equilibrium, the two species are evenly distributed and the concentration is the same at all points. The conservation of mass of each component of the mixture is expressed by the equation

$$\frac{d}{dt} c(\mathbf{r}, t) = \frac{\partial c}{\partial t} + \mathbf{v} \cdot \nabla c(\mathbf{r}, t) = 0 \quad (2.2)$$

In other words, the concentration of any fluid element remains unchanged during its state of motion. By using the equations 2.1 and 2.2, the following is also

verified

$$\frac{\partial}{\partial t}(c\rho) + \nabla \cdot (\mathbf{v}c\rho) = 0 \quad (2.3)$$

Where, to simplify the notation, I have eliminated the dependencies on \mathbf{r} and t . Turning to an integral form and applying Gauss's theorem to the right-hand side we obtain:

$$\frac{\partial}{\partial t} \int_V (c\rho) dV = - \oint_S (\mathbf{v}c\rho) ds \quad (2.4)$$

In this way it is clearly understood that the rate of change of a component in a certain volume is equal to the flux of the total volume through the surface (the velocity of the flux is the average velocity of the total mass).

When diffusion is taking place in addition to the *advective* motion of the fluid, it is necessary to add a term that accounts for the *relative* migration of the components; in this way, the integral form becomes

$$\frac{\partial}{\partial t} \int_V (c\rho) dV = - \oint_S (\mathbf{v}c\rho) ds - \oint_S \mathbf{i} ds \quad (2.5)$$

where \mathbf{i} is the density of the diffusion Flux.

Thus, in the presence of relative motion between species in the sample (e.g. in the presence of separation phenomena of two components of the sample) the \mathbf{i} flow term accounts for the fact that the concentration varies despite the local velocity of the fluid being zero. It is possible to turn back to a local form of the equation 2.5 to obtain the mass conservation equation for the diffusive phenomena that we will analyse later:

$$\frac{\partial}{\partial t}(c) + \mathbf{v} \cdot \nabla(c) + \frac{1}{\rho} \nabla \cdot (\mathbf{i}) \quad (2.6)$$

2.1.2 Equation of motion

To describe a fluid, it is essential to express not only the mass balance equation, but also the local momentum balance equation. Unlike in the previous section, for the equation of motion, no new terms need to be introduced to describe the

diffusive state. The classical equation of fluid dynamics remains useful to describe our specific case of a binary mixture in which the phenomenon of diffusion occurs

$$\frac{\partial \mathbf{v}}{\partial t} + (\mathbf{v} \cdot \nabla) \mathbf{v} = -\frac{\nabla p}{\rho} + \mathbf{g} + \nu \nabla^2 \mathbf{v} \quad (2.7)$$

where p is the pressure, g is the gravitational acceleration and ν is the kinematic viscosity. This equation means that the acceleration of any volume of fluid analysed (left-hand side term eq. 2.7) has three sources: pressure gradients giving rise to Archimede's thrust (first term of the right-hand side), the gravitational force (second term of the right-hand side) and the viscous force (third term of the right-hand side).

2.1.3 Diffusive Flux

An expression of the flux \mathbf{i} composed of the relative motions occurring within the sample due to the nonequilibrium state is given in this section. We assume that the nonequilibrium state is due to the presence of concentration and chemical potential gradients $\nabla \mu$ and ∇T , respectively; the value of the flux is therefore mathematically related to the intensity of these gradients. For simplicity, we assume that the flux depends linearly on these gradients, and therefore the following phenomenological equation is valid:

$$\mathbf{i} = -\alpha^* \nabla \mu - \beta^* \nabla T \quad (2.8)$$

where α^* and β^* are two phenomenological coefficients.

It is useful to write the chemical potential gradient as a function of the usual thermodynamic variables:

$$\nabla \mu = \left(\frac{\partial \mu}{\partial c} \right)_{p,T} \nabla c + \left(\frac{\partial \mu}{\partial T} \right)_{c,p} \nabla T + \left(\frac{\partial \mu}{\partial p} \right)_{c,T} \nabla p \quad (2.9)$$

now we can define the thermodynamic coefficients governing the linear dependencies:

$$D = \frac{\alpha^*}{\rho} \left(\frac{\partial \mu}{\partial c} \right)_{p,T} \quad (2.10)$$

$$\rho k_T \frac{D}{T} = \beta^* + \alpha^* \left(\frac{\partial \mu}{\partial T} \right)_{c,p} \quad (2.11)$$

$$\rho k_p = p \left(\frac{\partial \mu}{\partial p} \right)_{c,T} / \left(\frac{\partial \mu}{\partial c} \right)_{p,T} \quad (2.12)$$

where D is the mass diffusion coefficient that gives the value of the mass flux when only the concentration gradient is present. When a temperature gradient is present, a thermodiffusive term $\rho \frac{k_T D}{T} \nabla T$ appears in the total mass flux, where the coefficient $k_T D$ is called the thermal diffusion coefficient (k_t is the thermal diffusion ratio). Finally, replicating the reasoning done for the temperature gradient, when a pressure gradient is present the mass flux is defined by the barodiffusion coefficient $k_p D$ (k_p is the barodiffusion ratio). We can finally arrive at the expression for mass flux due to concentration, temperature and pressure gradients:

$$\mathbf{i} = -\rho D \left[\nabla c + \frac{k_T}{T} \nabla T + \frac{k_p}{p} \nabla p \right]. \quad (2.13)$$

We emphasize that the second term of the flow, the thermodiffusive term, is also called *Soret term*, since it comes from the effect of the same name. In this phenomenon, a mass flow is induced by the presence of a thermal gradient in the fluid. Usually, the coefficient characterizing this phenomenon is rewritten as $\frac{k_T}{T} = S_T c(1 - c)$, where S_T is the *Soret coefficient*, which measures the strenght of this effect.

2.2 Non Equilibrium Fluctuations

In the previous section we have introduced the equations of hydrodynamics that rule the macroscopic behavior of the fluid. However, in a fluid, the local thermodynamic quantities fluctuate in space and time. The linearization of the macroscopic equations allows to describe theoretically the dynamics of the fluctuations and to determine their correlation properties. These properties are fundamental because they are the only ones that can be measured experimentally with suitable optical techniques. For this paragraph I followed the steps detailed in [82]

2.2.1 Fluctuating Dynamics

Any physical quantity inherently has some uncertainty. This is usually due to several factors, particularly the sensitivity of the instrument used. In our case, because of the microscopic nature of the fluid, this uncertainty becomes intrinsic to the phenomenon we are studying and takes on a very interesting physical significance. I first write the fluid dynamic variables as the sum of a part expressing the mean value and another part indicating the fluctuation of the quantity in time and space:

$$c(\mathbf{x}, t) = \langle c(\mathbf{x}, t) \rangle + \delta c(\mathbf{x}, t) \quad (2.14)$$

$$\rho(\mathbf{x}, t) = \langle \rho(\mathbf{x}, t) \rangle + \delta \rho(\mathbf{x}, t) = \langle \rho(\mathbf{x}, t) \rangle + \rho \beta \delta c(\mathbf{x}, t) \quad (2.15)$$

$$\mathbf{v}(\mathbf{x}, t) = \langle \mathbf{v}(\mathbf{x}, t) \rangle + \delta \mathbf{v}(\mathbf{x}, t) = \delta \mathbf{v}(\mathbf{x}, t) \quad (2.16)$$

Where $\beta = \rho^{-1}(\partial \rho / \partial c)_{p, T}$ is the solutal expansion coefficient. Two assumptions appear in these equations: the first, in equation 2.15, is the Boussinesq approximation, where we have assumed that the density fluctuations are due exclusively to changes in concentration. Given that we will be investigating a system that consists of a binary mixture and will be conducting our study under isothermal conditions, it is reasonable to neglect any density fluctuations that may arise due to temperature variations. The second is that the fluid is at rest, and therefore the velocity field of equation 2.16 is composed exclusively of the fluctuating part.

Having written the variables in this way, we insert them into equations 2.6 and 2.7 and, assuming that fluctuations are small, eliminate second-order terms

$$\frac{\partial c}{\partial t} + \frac{1}{\rho} \nabla \cdot \mathbf{i} = -\frac{\partial \delta c}{\partial t} - \delta \mathbf{v} \cdot \nabla c - \frac{1}{\rho} \nabla \cdot \delta \mathbf{i} + \frac{1}{\rho} \beta \delta c \nabla \cdot \mathbf{i} + \nabla \cdot \mathbf{F} \quad (2.17)$$

$$\frac{\nabla p}{\rho} - \mathbf{g} = -\frac{\partial \delta \mathbf{v}}{\partial t} + \frac{1}{\rho} \beta \delta c \nabla p + v \nabla^2 \delta \mathbf{v} + \frac{1}{\rho} \nabla \cdot \mathbf{S} \quad (2.18)$$

In writing equations 2.17 and 2.18 have added extra terms source, $\nabla \cdot \mathbf{F}$ and $\frac{1}{\rho} \nabla \cdot \mathbf{S}$ respectively [51]. In these terms \mathbf{F} and \mathbf{S} represent random forces describing the spontaneous and random nature of the fluctuations in concentration and velocity.

These forces are always present in fluids (even for single-component fluids without thermal gradients) and we assume that they do not change their form when passing from a state of equilibrium to one of non-equilibrium: this is because they only account for very fast molecular processes and, at the molecular level, the presence of thermal or concentration gradients is totally negligible.

To complete the system of equations, it is necessary to also add the one describing the evolution of the macroscopic diffusive state:

$$\frac{\partial c}{\partial t} + \frac{1}{\rho} \nabla \cdot \mathbf{i} = 0 \quad (2.19)$$

We also impose $\nabla p = \rho \mathbf{g}$, which means that the pressure varies only due to the gravitational field. Applying these assumptions to the equations 2.17 and 2.18 we obtain:

$$\frac{\partial \delta c}{\partial t} = -\delta \mathbf{v} \cdot \nabla c - \frac{1}{\rho} \nabla \cdot \delta \mathbf{i} + \frac{1}{\rho} \beta \delta c \nabla \cdot \mathbf{i} + \nabla \cdot \mathbf{F} \quad (2.20)$$

$$\frac{\partial \delta \mathbf{v}}{\partial t} = \beta \mathbf{g} \delta c + \nu \nabla^2 \delta \mathbf{v} + \frac{1}{\rho} \nabla \cdot \mathbf{S} \quad (2.21)$$

In these equations, the link between velocity fluctuations and concentration fluctuations becomes apparent. Indeed, the term $\delta \mathbf{v} \cdot \nabla c$ of equation 2.20 shows that, in the presence of a concentration gradient, velocity fluctuations contribute to the dynamics of concentration fluctuations; conversely, the term $\beta \mathbf{g} \delta c$ of equation 2.21 shows that concentration fluctuations, in turn, are a source term for velocity fluctuations.

To conclude this part, it is necessary to write an expression for the fluctuating part of the mass flow $\delta \mathbf{i}$, so as to link this quantity to thermodynamic variables. To do this, I linearise equation 2.13, obtaining, in the case of isobaric and isothermal conditions.

$$\nabla \cdot \delta \mathbf{i} = -\rho D \nabla^2 \delta c + \beta \delta c \nabla \cdot \mathbf{i} + \beta \mathbf{i} \cdot \nabla \delta c - \rho \beta D \nabla \delta c \cdot \nabla c \quad (2.22)$$

In this way, with equations 2.20, 2.21 and 2.22, I have outlined the foundations (well known from the literature) for a study of the fluctuating part of the thermodynamic variables. In particular, I emphasise that, in the presence of concentration gradients (i.e. outside equilibrium), the fluctuating variables turn out to

have extra source terms determined by the presence of a macroscopic gradient, compared to equilibrium.

2.2.2 Structure Factor

In this part we will deal with the correlation properties of the fluctuations. It is necessary to elaborate on this topic, since with light scattering experiments one only has access to the correlation properties of the fluctuations and not directly to the 'pure' variables. In particular, it is interesting to observe these correlation properties of fluctuations in Fourier space and not in real space. We consider the practical case where a horizontal layer of a binary mixture is under the action of a concentration gradient parallel to \mathbf{g} . The system is investigated with scattering by shining an incident beam of radiation parallel to the gradient. For a system in which the incident light beam and the concentration is parallel to \mathbf{g} , the spatial Fourier Transform of the concentration fluctuations, becomes:

$$\delta c(\mathbf{q}, \omega)_{z,t} = \int dt \int c(\mathbf{x}, t) e^{i(\mathbf{q} \cdot \mathbf{x} - \omega t)} dx dy \quad (2.23)$$

where the wave vector \mathbf{q} is the one lying on the horizontal plane and ω is the time frequency. The subscripts z and t denote the z -coordinate and the macroscopic time instant we are considering. The variable \mathbf{x} denotes the (x, y) plane.

The kind of light scattering we analyze is Rayleigh scattering: incident light is deflected quasi-elastically by a fluctuation in the local refractive index of the fluid, with no appreciable change in the frequency of the light. Only velocity fluctuations parallel to the incident light beam contribute in these processes, and thus the transformed momentum equation (Eqn. 2.23) can be projected in the direction parallel to light beam (the vertical direction) by the projection operator $\mathbf{1} - \mathbf{q}\mathbf{q}$; projecting and transforming the equations 2.17 and 2.18 onto the horizontal plane we get:

$$\delta c_{\mathbf{q}, \omega}(i\omega + Dq^2) = -\delta \mathbf{u}_{\mathbf{q}, \omega} \cdot \nabla c(z, t) - i\mathbf{q} \cdot \mathbf{F}_{\mathbf{q}, \omega} \quad (2.24)$$

$$\delta \mathbf{u}_{\mathbf{q}, \omega}(i\omega + \nu q^2) = \beta \delta c_{\mathbf{q}, \omega} \mathbf{g} \cdot (\mathbf{1} - \mathbf{q}\mathbf{q}) - \frac{i}{\rho} \mathbf{q} \cdot \mathbf{S}_{\mathbf{q}, \omega} \cdot (\mathbf{1} - \mathbf{q}\mathbf{q}) \quad (2.25)$$

Where $(\mathbf{1}-\mathbf{q}\mathbf{q})$ is the projection operator on the vertical plane and \mathbf{u} is the velocity component perpendicular to \mathbf{q} .

By arranging the two equations 2.24 and 2.25, we obtain:

$$\begin{aligned} \delta c_{\mathbf{q},\omega} [(i\omega + Dq^2)(i\omega + vq^2) + \beta \mathbf{g} \cdot \nabla c(z,t)] = \\ -i(i\omega + vq^2)\mathbf{q} \cdot \mathbf{F}_{\mathbf{q},\omega} - \frac{i}{\rho} \mathbf{q} \cdot \mathbf{S}_{\mathbf{q},\omega} \cdot (\mathbf{1}-\mathbf{q}\mathbf{q}) \cdot \nabla c(z,t) \end{aligned} \quad (2.26)$$

Now that we have a set of algebraic equations, we can write the correlation properties of concentration fluctuations $\langle \delta c_{\mathbf{q},\omega} \delta c_{\mathbf{q},\omega}^* \rangle$.

To do the calculation we need to know the correlation properties of random forces. Assuming that \mathbf{F} and \mathbf{S} are not affected by the macroscopic out-of-equilibrium state, we obtain:

$$\langle F_{\mathbf{q},\omega} F_{\mathbf{q},\omega}^* \rangle = \frac{k_B T}{8\pi^4 \rho} D (\partial c / \partial \mu)_{p,t} \delta_{i,j} \delta(\mathbf{q}-\mathbf{q}') \delta(\omega - \omega') \quad (2.27)$$

$$\langle (\mathbf{q} \cdot \mathbf{S}_{\mathbf{q},\omega} \cdot (\mathbf{1}-\mathbf{q}\mathbf{q}) \cdot \nabla c(z,t)) (\mathbf{q} \cdot \mathbf{S}_{\mathbf{q},\omega}^* \cdot (\mathbf{1}-\mathbf{q}\mathbf{q}) \cdot \nabla c(z,t)) \rangle = \frac{k_B T}{8\pi^4} \rho v |\nabla c|^2 \quad (2.28)$$

$$\langle F_{\mathbf{q},\omega} S_{\mathbf{q}',\omega'}^* \rangle = 0 \quad (2.29)$$

Using equations 2.26, 2.27, 2.28 and 2.29 we can write the complete expression of the correlation function for concentration fluctuations:

$$\langle \delta c_{\mathbf{q},\omega} \delta c_{\mathbf{q},\omega}^* \rangle = \frac{k_B T}{8\pi^4 \rho} \left[\frac{(\omega^2 + v^2 q^4) D q^2 (\partial c / \partial \mu)_{p,t} + v q^2 |\nabla c(z,t)|^2}{|(i\omega + Dq^2)(i\omega + vq^2) - [R(q)/R_c] v D q^4|^2} \right] \quad (2.30)$$

Where $R(q)/R_c$ is the Rayleigh number ratio, which defines the convection threshold as the concentration gradients change

$$R(q)/R_c = \frac{\beta \mathbf{g} \cdot \nabla c(z,t)}{v D q^4} \quad (2.31)$$

Thanks to some mathematical manipulation and assuming that

$$D/\nu \ll 1 \quad (2.32)$$

$$\frac{-4R(q)D}{R_c\nu} \ll 1 \quad (2.33)$$

it is possible to reduce equation 2.30 to the sum of two Lorentzians. Both assumptions Eqn. 2.32 and Eqn.2.33 are justified by physical considerations. The first hypothesis is $D/\nu \ll 1$ where the quantity ν/D is called the Schmidt number Sc . This number is a non-dimensional parameter that represents the ratio between the momentum diffusivity (i.e. kinematic viscosity ν) and the mass diffusivity of a fluid D . It serves as a valuable tool for characterizing fluid flows in which there are concurrent momentum and mass diffusion convection processes. The first hypothesis, $D/\nu \ll 1$, is valid since the typical values for organic fluid mixtures are $\nu \sim 10^{-3} \frac{cm^2}{s}$ and $D \sim 10^{-5} \frac{cm^2}{s}$, all the cases studied in this thesis satisfy this hypothesis, while the second hypothesis, $\frac{-4R(q)D}{R_c\nu} \ll 1$, eliminates the possibility that the fluctuation spectrum has a propagating part [69], [70].

The first Lorentzian we find from the equation 2.30 has a width of $Dq^2[1 - R(q)/R_c]$, while the width of the second is νq^2 ; since $D \ll \nu$ we can assume that the wider Lorentzian is constant with respect to the other one. We can thus write:

$$\langle \delta c_{\mathbf{q},\omega} \delta c_{\mathbf{q},\omega}^* \rangle = S(q) \frac{2Dq^2[1 - R(q)/R_c]}{\omega^2 + (Dq^2[1 - R(q)/R_c])^2} \quad (2.34)$$

Where $S(q)$ is the static structure factor describing the time independent part of the correlation properties, defined as:

$$S(q) = S_{eq} \left[1 + \left(\frac{\nabla c(z,t)}{\nabla c_{grav}} - 1 \right) \frac{1}{1 + \left(\frac{q}{q_{ro}} \right)^4} \right] \quad (2.35)$$

Where the equilibrium static structure factor S_{eq} is defined as:

$$S_{eq} = \frac{k_b T}{16\pi^4 \rho} \left(\frac{\partial c}{\partial \mu} \right)_{p,T} \quad (2.36)$$

and the concentration gradient induced by the gravitational force at equilibrium ∇c_{grav} is defined as:

$$\nabla c_{grav} = -\frac{k_p}{p} \nabla p = \beta \mathbf{g} \left(\frac{\partial c}{\partial \mu} \right)_{p,T} \quad (2.37)$$

The roll-off wave vector q_{ro} represents the scale of the transition between a regime of the relaxation of fluctuations dominated by gravity at small wave vectors and one dominated by diffusion at large ones. Since we have defined $R(q)$ as in eq. 2.31, it follows that $R(q)/R_c = -(q/q_{ro})^4$ where q_{ro} is defined as:

$$q_{ro} = \left(\frac{\beta \mathbf{g} \cdot \nabla c}{\nu D} \right)^{1/4} \quad (2.38)$$

$S(q)$, described by the formula 2.35, provides us information about the mean squared amplitude of fluctuations at each wavenumber. On the other hand, if we want to know the dynamics of these fluctuations, it is necessary to analyze the second part of the equation 2.34, where the time frequency dependence ω appears:

$$g(q, \omega) = \frac{2Dq^2 [1 + (q_{ro}/q)^4]}{\omega^2 + (Dq^2 [1 + (q_{ro}/q)^4])^2} \quad (2.39)$$

For clarity, it is useful for us to move from the frequency domain to the time domain with a Fourier antitransform. I emphasize that the solution we derive is valid only in the case of a thin layer of fluid, in which the thermodynamic coefficients are approximately constant. Then, by transforming in ω we obtain that the correlation, fixed at a certain scale q , decays exponentially over time:

$$g(q, t) = e^{-\gamma(q)t} \quad (2.40)$$

where the relaxation rate $\gamma(q)$ represents the width of the Lorentzian Eqn. 2.39.

$$\gamma(q) = Dq^2[1 + (q_{ro}/q)^4] \quad (2.41)$$

In the relationship referenced as 2.41, two distinct regimes in the relaxation rates can be observed. For large wavenumbers where q is much greater than q_{ro} , the relaxation rate is proportional to the square of the wavenumber and is dominated by diffusion, i.e., $\gamma(q) \sim Dq^2$. On the other hand, for small wavenumbers, the relaxation rate is proportional to q_{ro} divided by the square of the wavenumber and is dominated by gravity, i.e., $\gamma(q) \sim Dq_{ro}/q^{-2}$.

In summary, in the previous paragraphs I have introduced the theoretical basis, needed to understand the concentration fluctuations that occur during diffusive processes in a thin sample. In particular, this last paragraph on the structure factor is crucial because it describes the quantities that we can access experimentally. These quantities are the static structure factor (eq. 2.35) and the correlation function (eq. 2.40), both of which can be measured using optical techniques that we will explain in the next paragraphs.

2.3 Experimental validation and open challenges

The theoretical predictions presented in the previous section have been confirmed experimentally by several works. In this section we summarize the most important results obtained both under the influence of gravity and when it is negligible.

2.3.1 Experimental results obtained on Earth.

To show the experimental confirmations, I chose to present the results reported in two representative papers, one regarding the static power spectrum and one for the dynamics of the fluctuations. Both of these articles have been a key benchmark for my work.

With regard to statics, it is useful to recall the results obtained by [81]. In this paper it is clearly observed that, during free diffusion occurring in a previously separated mixture, the concentration fluctuations are enormously more intense than when diffusion is absent; *free diffusion* refers to a diffusive process that is

not affected by boundary conditions. The authors created an initially sharp interface between two miscible fluids by letting a mixture separate in phase below the critical consolution temperature. As soon as the temperature is increased rapidly to the single-phase region, the two phase become miscible and a free diffusion process starts.

Fig. 2.1 shows a sequence of scattered intensity distributions as a function of q , taken at various times after the beginning of the diffusion process. These scattered intensity distributions represent a direct measure of the static structure factor $S(q)$. The strongest diffusion occurs for the first set (circles) obtained immediately after quenching in the single-phase region. The diffusion intensity diverges as q decreases, but the curves eventually saturate to a constant value at q smaller than the roll-off q value, which was defined in equation 2.38 .

As explained in the previous section, the value of q_{ro} determines the minimum wavenumber at which the effects of gravity are not felt. For lower q vectors, the strong divergence q^{-4} (Eqn.2.35) breaks down.

On the other hand, with regard to dynamics, I report the results developed by [30]. In this paper, fluctuations in a binary mixture of water and glycerol are studied. A layer of water and glycerol about 1 cm thick, 39% concentrated, and a layer of pure distilled water also 1 cm thick are brought into contact. In this configuration, the more concentrated layer is at the bottom, so the glycerol diffuses throughout the sample until the concentration is uniform. By studying the dynamics of the concentration fluctuations, it was possible to derive their decay rate γ at each q scale. Figure 2.2 shows the predicted and experimental results for this decay rate. As it can be seen, the prediction (Eqn.2.41) that the decay rate should reach a minimum near q_{ro} is correct. In a purely diffusive regime, the relaxation rates of the fluctuations should continue to decrease, as the wave vector decreases; this does not happen because of gravity, which, below a certain characteristic wavenumber q_{ro} , dampens the fluctuations by speeding up the relaxation rate. For this reason, in figure 2.2, it can be observed that at high q the decay rate is purely diffusive $\gamma = Dq^2$ while for low q the regime is typically gravity-gravitational $\gamma(q) \sim Dq_{ro}/q^{-2}$.

Both the statics and the dynamics of the fluctuations are affected by the gravity force. Being able to analyze NEFs so accurately, up to the very small wave

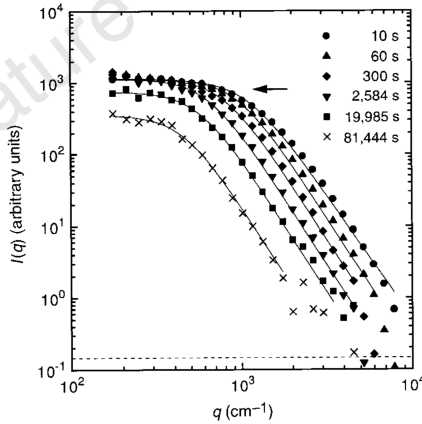


FIGURE 2.1: *Non-equilibrium scattered intensity distributions plotted as a function of the wavevector q at different times during the diffusion process. The solid line through the data is their best fit with equation 2.35. The dashed line is the reference equilibrium intensity scattered by the sample in its homogeneous state. The arrow marks is the level of the non-equilibrium forward scattered intensity at the plateau (small q). [81].*

vectors where gravity affects the fluctuations significantly, has prompted the scientific community to remove the limitations imposed by gravity and observe this phenomenon in its full spectrum. Regarding this, in the next section I will show the results obtained in the Gradflex space experiment of ESA and NASA that investigated these fluctuations under microgravity conditions during the FOTON M3 mission. The experimental determination of the time autocorrelation function of non-equilibrium concentration fluctuations during a free diffusion process [Croccolo et al. 1989] has confirmed that they decay exponentially in time (Fig.2.3)

In my doctoral work, I studied nonequilibrium concentration fluctuations during free diffusion of glycerol in water but for much higher glycerol concentrations than those presented in the article [30]. These high concentrations lead to the need to change the interpretative model of correlation properties. Indeed, we will see that, under the conditions I investigated, the data no longer present

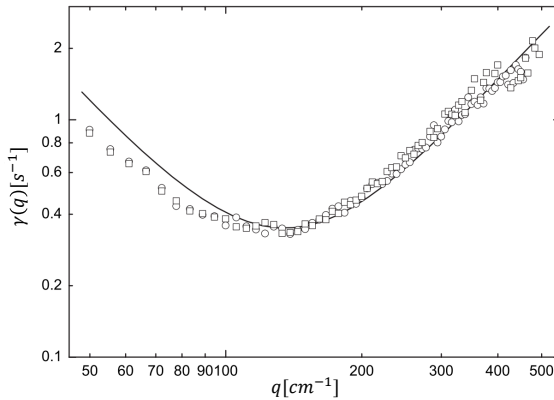


FIGURE 2.2: Decay rate γ (Eqn.2.41) at two different times from the beginning of diffusion plotted as a function of the wave vector q . The squares are measured after 14880s from the onset of diffusion, while the circles after 15420s. The minimum of these decay rates is close to the roll-off wave vector q_{ro} , for the squares $q_{ro} = 126.2\text{cm}^{-1}$ while for the circles $q_{ro} = 124.6\text{cm}^{-1}$. [30].

the purely exponential relaxation trend shown in Figure 2.3.

2.3.2 Experimental results under microgravity conditions.

As mentioned earlier, my doctoral work is part of Neuf DIX space project of the European Space Agency (ESA), a project aimed at the investigation of Non-EquilibriUm Fluctuations during Diffusion in compleX liquids (NEUF-DIX Giant Fluctuations) [1]. The focus of the project is on the investigation in microgravity conditions of the non-equilibrium fluctuations in complex liquids, trying to tackle several challenging problems that emerged during the latest years. The grounds of the Neuf-Dix project are represented by the GRADFLEX project [84], concluded in 2007. GRADFLEX investigated non-equilibrium concentration fluctuations occurring during diffusion experiments in a Polystyrene-Toluene solution ($MW = 9,100\text{ g mol}^{-1}$, average concentration 1.8 wt%) under microgravity conditions. The experiments were performed during the flight

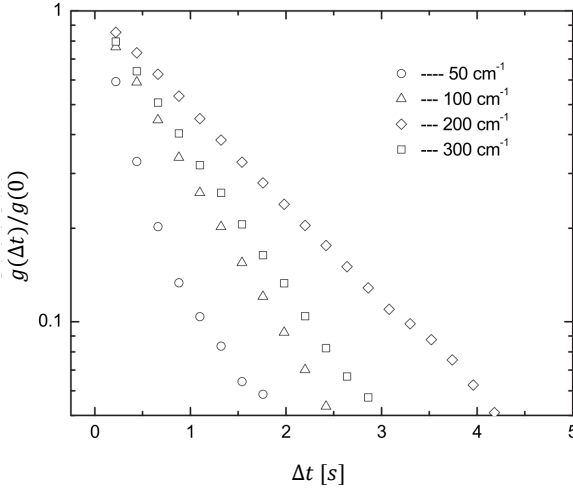


FIGURE 2.3: Correlation function $g(q, \Delta t)$ obtained by fixing four different wave vectors indicated in the legend. The measurement was taken 600s after the onset of diffusion. [30].

of FOTON M3, a retrievable capsule inserted into orbit about 300 km above the Earth's surface. The experimental procedure involved an initial equilibration phase at a uniform temperature of 30.0 C for 260 minutes. This phase was followed by the rapid imposition of a temperature difference across the sample, which initiated a thermal diffusion process. The temperature differences used were 4.35, 8.70 and 17.40K. The time required for the formation of a linear temperature profile was approximately 100 s. In contrast, the time $\tau_0 = h^2 / (\pi^2 D)$ to create a steady-state concentration profile was about 500 s; here $D = 1.97 \cdot 10^{-6} \text{ cm}^2/\text{s}$ is the diffusion coefficient and $h = 1.00 \text{ mm}$ is the sample thickness. Removing gravity, low q fluctuations are several orders of magnitude more intense than those occurring on earth Fig.2.4; secondly, in the same figure, one can observe that by normalizing the structure functions with $S_\infty = \lim_{q \rightarrow \infty} S(q) \cdot q^{-4}$ in the absence of gravity all the curves scale in the same way, on the other hand, on earth, there is a different trend at low q . This is because the plateau reached at

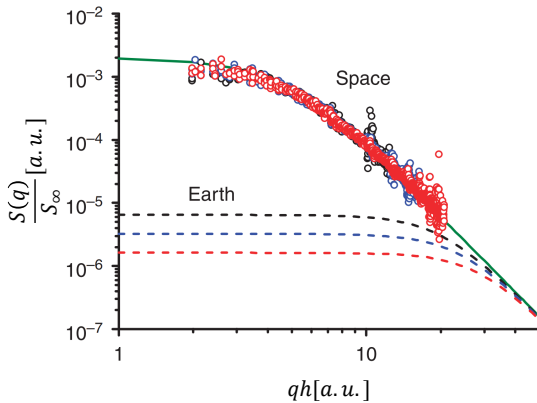


FIGURE 2.4: *Experimental results for the static structure factor of non-equilibrium fluctuations obtained in microgravity in the presence of temperature differences of 4.35 K (black), 8.70 K (blue) and 17.40 K (red). The circles are the experimental data, normalized by S_{∞} , the dashed lines represent the theoretical predictions on earth while the green solid line is the theoretical prediction under microgravity conditions. One can appreciate the good agreement between the experimental results and the theoretical predictions. In microgravity, the data scale onto a single universal curve, whereas on the Earth no such scaling occurs. [84]*

low q on earth indicates that the system was in a gravitational regime which depends on the imposed concentration gradient. On the other hand, when placed in microgravity conditions, this phenomenon is eliminated and the only limitations to a divergence of the fluctuations at small q is represented by the final size of the sample (independent of the concentration gradient set in the sample).

The GRADFLEX experiment investigated non-equilibrium concentration fluctuations during a stationary diffusion process. The concentration gradient is kept constant within the sample by a constant temperature gradient.

The dynamics of the relaxation of non-equilibrium fluctuations is also significantly affected by the absence of gravity. The bell-shaped pattern with a vertex in the q_{ro} is lost, and only a purely diffusive regime is observed (Fig.2.5). To summarise: thanks to the microgravity conditions, it was possible to investigate

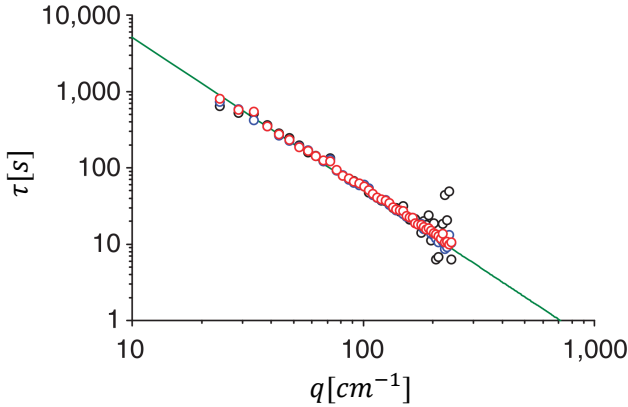


FIGURE 2.5: *Relaxation time of non-equilibrium concentration fluctuations as a function of wave vector. The black data correspond to a temperature difference of 4.35 K, the blue data to 8.70 K and the red ones to 17.40 K. The solid line represents the diffusive time (defined as the reciprocal of γ , equation 2.41) $\tau(q) = 1/\gamma = 1/(Dq^2)$ as estimated from literature data for the diffusion coefficient. [84].*

non-equilibrium fluctuations in their full intensity. These results have encouraged our group to undertake further space missions to tackle some unresolved problems. The goals of the Neuf Dix mission are [1]:

- the experimental verification of the existence and intensity of the novel non-equilibrium Casimir effect [45], that is so far unavailable;
- the understanding of the non-equilibrium fluctuations in polymer solutions, in relation to their behavior close to a glass transition [64];
- the understanding of the non-equilibrium fluctuations in concentrated colloidal suspensions problem closely related with the detection of Casimir forces [41];
- the understanding of the non-equilibrium fluctuations in multi-component mixtures, in relation to the transport coefficients;

- the investigation of the development of fluctuations during transient diffusion [13]; [20]
- Experiments in space will provide a better understanding of the mechanisms that induce protein aggregation under nonequilibrium conditions.

in particular, the results presented in this PhD thesis, provide a contribution to the study of fluctuations occurring in strongly nonideal systems, such as very dense colloidal solutions or multicomponent mixtures.

Chapter 3

Shadowgraph technique and processing methods.

This section introduces the optical technique and analysis procedure used to investigate non-equilibrium fluctuations within the sample. In this study, we utilized the Shadowgraph technique to visualize non-equilibrium fluctuations. This technique requires a spatially coherent collimated beam of light to pass through a transparent medium, providing a noninvasive measurement of the refractive index profile perpendicular to the direction of propagation of the light beam.

The Shadowgraph method uses a beam of light that is parallel and coherent in space. This beam passes through a layer of fluid, and when it does so, it scatters with the molecules that make up the fluid. As the transmitted beam moves away from the fluid layer, it creates a pattern of varying intensity. The distribution of this pattern reveals the non-uniformities in the local refractive index.

To explain *qualitatively* this intensity profile, we can utilize geometrical optics. The light rays slightly deviate as they pass through the fluid, bending toward the higher refractive index regions and away from the lower index regions. The angular deflection is small, and the rays move very little as they pass through the layer. Therefore, the local intensity of the beam is not significantly altered as it passes through the layer, but the angular deflection is sufficient to produce a focusing effect over the higher index regions as the beam propagates past the fluid layer. The resulting intensity distribution can be photographed or recorded with a digital camera, obtaining the 2D map of the underlying thermal perturbation.

The Shadowgraph technique was historically used to probe convective patterns [73], which have a non-linear profile of refractive index. Only recently it has been used to visualize refractive index modulations due to non-equilibrium fluctuations [81]. Using an algorithm based on image difference analysis, it is possible to extract information from Shadowgraph signals not only concerning the intensity of the fluctuations, but also their dynamics [30]. We will explain the operation of an algorithm developed recently that significantly reduces computation time, providing this information.

3.1 Shadowgraph technique

In order to describe *quantitatively* the distribution of light intensity on a screen after passing through a sample, it is necessary to utilize physical optics rather than geometrical optics. Specifically, when a plane wave passes through a transparent fluid layer, it undergoes a phase modulations. The wave that exits the fluid layer can be decomposed into the superposition of plane waves, which propagate beyond the cell. These plane waves generate an interference pattern that is recorded as the shadowgraph signal.

In order to describe the path of light through the sample, we must establish an expression for the refractive index profile within the sample. We make the assumption that the refractive index is uniform in space and constant in time when in air, in other words, the surrounding air does not introduce any significant perturbation. Our analysis considers a scenario in which a plane wave is propagating perpendicular to the horizontal xy -plane. A horizontal thin layer of fluid with a thickness L is crossed by the beam, and within this layer, there exists a refractive index profile $n(\mathbf{x}, z, t)$ denoted by

$$n(\mathbf{x}, z, t) = n(z, t)_0 + \left(\frac{\partial n}{\partial c} \right)_P \delta c(\mathbf{x}, z, t) \quad (3.1)$$

where $n(z, t)_0$ is the macroscopic refractive index profile present in the sample. This profile is dependent on the macroscopic profile of thermodynamic variables, particularly the local concentration $c(z, t)$, which has a linear relationship with the refractive index in the experiments addressed in this thesis [67]. The

second term on the right-hand side, $\left(\frac{\partial n}{\partial c}\right)_P \delta c(\mathbf{x}, z, t)$, accounts for concentration fluctuations.

As the refractive index is defined as the ratio of the speed of light in vacuum to that in the medium, the passage of light through the medium results in a slowing down of light rays. This slowing down results in a phase shift in the outgoing rays from the sample compared to the incoming ones. In our case, since the concentration profile is uniform in the horizontal plane and varies on time scales that are much slower than local concentration fluctuations, we can treat the macroscopic phase shift $\Phi_0(t)$ as constant in time and over the $\mathbf{x} = xy$ -plane. We can quantify this accumulation of phase delay by setting the phase of the incident beam arbitrarily as $\Phi_{in} = 0$ and calculating the phase of the outgoing beam using the following relation:

$$\begin{aligned} \Phi(\mathbf{x}, L, t) &= q_0 \int_0^L n(\mathbf{x}, t) dz = \phi_0 + q_0 \int_0^L \left(\frac{\partial n}{\partial c}\right)_P \delta c(\mathbf{x}, z, t) dz \\ &= \phi_0 + \delta\phi(\mathbf{x}, z, t)_c \quad (3.2) \end{aligned}$$

q_0 represents the wave number of the incident light, while $\phi_0 = (q_0 n_0 L + \frac{1}{2} q_0 \nabla n_0 L^2)$ corresponds to the phase shift resulting from the macroscopic gradient n_0 and $\delta\phi(\mathbf{x}, z, t)_c = q_0 \left(\frac{\partial n}{\partial c}\right)_P \int_0^L \delta c(\mathbf{x}, z, t) dz$. The term $\delta\phi$ captures the effects of nonequilibrium fluctuations, which spontaneously arise in the sample. As detailed in previous chapters, these fluctuations, known as NEFs, form randomly in space and evolve over time according to a well-defined dynamics, described by Eqn. 2.40. The Huygens-Fresnel principle posits that each point on a wavefront acts as a source of spherical waves, and the superposition of these waves generates the resulting wavefront. In our experiment, plane waves pass through the sample (as illustrated in Fig.3.1). As the beam travels through the sample, its wavelength changes due to the sample's refractive index being different from that of air. When the refractive index is uniform within the sample (as shown in Fig.3.1a), the phase is also uniform at all points. The waves will recombine constructively, generating a uniform plane wavefront out of phase with the initial wavefront ($\Phi(\mathbf{x}, L, t) = \phi_0$). This produces a Gaussian intensity profile

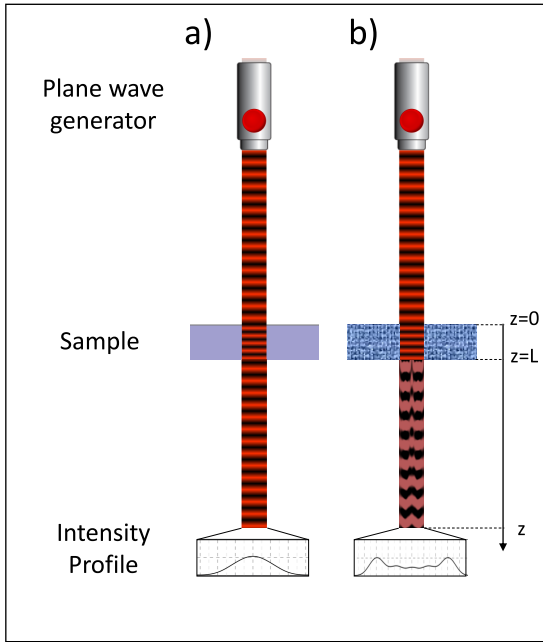


FIGURE 3.1: Schematic representation of the optical path for plane waves passing through the sample and detected on a screen to measure their intensity. (a) Uniform sample, and (b) non-uniform sample interference pattern.

on the screen within the illuminated area, since the original plane wave generated by the light source had a gaussian profile.

However, if the sample contains non-uniformities, the spherical Huygens waves making up the beam will interfere with each other, resulting in a distinct interference pattern on the screen's intensity profile (as shown in Fig.3.1b).

To propagate the wave and measure the intensity profile at a distance from the sample, we express the amplitude of the phase-shifted electric field leaving the sample in the following form:

$$E_0(\mathbf{x}, L, t) = E_0 e^{i[\phi_0 + \delta\phi(\mathbf{x}, t)]} \quad (3.3)$$

where the complex amplitude E_0 of the incident beam at $z = 0$ undergoes a phase shift as per equation 3.2. It is important to note that the amplitude value $E_0(\mathbf{x}, L, t)$ value varies with time as the phase shift due to fluctuations is also time-dependent. To obtain the intensity profile on a screen placed at a specific position z , we must propagate and sum the amplitudes of the electric field at each point in the plane at distance $z = L$. This can be achieved by utilizing the Fresnel approximation [8]. The resulting solution is expressed as:

$$E(\mathbf{x}, z, t) = i \frac{e^{-iq_0 z}}{\lambda_a z} \int_A d^2 \mathbf{x}' E_0 e^{i[\phi_0 + \delta\phi(\mathbf{x}', t)]} e^{-i \frac{q_0}{2z} (\mathbf{x}' - \mathbf{x})^2} \quad (3.4)$$

where $\lambda_a = \frac{2\pi}{q_0}$ is the wavelength of light in the air and A is the integration surface based clear aperture of the the optical window through which the light passes in the sample.

By assuming that the fluctuations are small, we can approximate the term $e^{i\delta\phi}$ in equation 3.4 to first order. By extracting the constant terms from the integral, we obtain the following expression:

$$\begin{aligned} E(\mathbf{x}, z, t) &\sim i E_0 \frac{e^{-iq_0 z - \phi_0}}{\lambda_a z} \int_A d^2 \mathbf{x}' [1 + i\delta\phi(\mathbf{x}', t)] e^{-i \frac{q_0}{2z} (\mathbf{x}' - \mathbf{x})^2} \\ &= E_0 e^{-iq_0 z - \phi_0} \left[1 - \frac{q_0}{2\pi z} \int_A d^2 \mathbf{x}' \delta\phi(\mathbf{x}', t) e^{-i \frac{q_0}{2z} (\mathbf{x}' - \mathbf{x})^2} \right] \end{aligned} \quad (3.5)$$

To simplify the mathematical analysis, we solved the first Gaussian integral, which excluded the fluctuating components, while approximating an infinite integration surface A

$$\int d^2 \mathbf{x}' e^{-i \frac{q_0}{2z} (\mathbf{x}' - \mathbf{x})^2} = -i \frac{2\pi z}{q_0} = -i \lambda_a z \quad (3.6)$$

with this simplification, we can now determine the intensity profile on a screen located at a distance z from the sample entrance.

We define the intensity at any given position as the square modulus of the complex amplitude of the field present at that particular location

$$I(\mathbf{x}) = I_0 \left[1 - \frac{q_0}{2\pi z} \frac{1}{\Delta t} \int_0^{\Delta t} dt \int_A d^2\mathbf{x}' \delta\phi(\mathbf{x}', t) e^{-i\frac{q_0}{2z}(\mathbf{x}' - \mathbf{x})^2} - c.c. \right] \quad (3.7)$$

where $I_0 = |E_0|^2$ is the incident light intensity and Δt is the signal formation time in the detector device, and the *c.c.* term represents the complex conjugate part of the integral. The quadratic terms in the fluctuations have been neglected. In this doctoral thesis, we focused on investigating the fluctuating component of the intensity in equation 3.7. However, the fluctuating part is significantly smaller than the stationary component I_0 . Thus, in order to isolate the signal of the fluctuations, it is necessary to remove the stationary part of the signal.

To accomplish this, we captured sequences of images and exploited the stochastic nature of the fluctuations. Specifically, since the fluctuations are temporally uncorrelated and t is significantly larger than the largest correlation time of the fluctuations, their time average over multiple images is zero: $\langle \delta\phi \rangle_t = 0$. This allowed us to calculate I_0 and optical background and subtract it from the real part of the intensity profile. By doing so, we obtained a signal that we can analyze in our measurements.

$$\delta I(\mathbf{x}) = \frac{I(\mathbf{x}) - I_0}{I_0} = \frac{q_0}{2\pi z} \frac{1}{\Delta t} \int_0^{\Delta t} dt \int_A d^2\mathbf{x}' \delta\phi(\mathbf{x}', t) \cos \left[\frac{q_0}{2z}(\mathbf{x}' - \mathbf{x})^2 \right] \quad (3.8)$$

To examine the fluctuations at various spatial scales $\lambda = \frac{2\pi}{|\mathbf{q}|}$, we apply a Fourier transform to the signal. Specifically, we decompose the signal and investigate the spatial power spectrum of intensity $|\delta I(\mathbf{q})|^2$. We then calculate the average power spectrum over a set of shadowgraph images in order to increase the statistical accuracy of the power spectra by lowering the stochastic noise terms [87]; [12]

$$\langle |\delta I(\mathbf{q})|^2 \rangle = \int d^2\mathbf{x} \int d^2\mathbf{x}' \langle \delta I^*(\mathbf{x}) \cdot \delta I(\mathbf{x}') \rangle e^{i\mathbf{q}(\mathbf{x} - \mathbf{x}')} \quad (3.9)$$

In Fourier space, \mathbf{q} represents the two-dimensional wave vector conjugated to the spatial coordinate \mathbf{x} . Our goal is to derive an expression for the power spectrum that is related to the fluid structure factor.

Examining the equation 3.9, we observe that the term $\langle \delta I(\mathbf{x}, t) \delta I(\mathbf{x}', t') \rangle$ appears in it. The variable $\delta I(\mathbf{x})$ is defined in Eqn. 3.8 and we observe that the term $\delta \phi(\mathbf{x}, t)$ appears in it. In addition, as can be seen from the equation 3.2, the concentration fluctuations term $\delta c(\mathbf{x}, t)$ is present in the definition of $\delta \phi(\mathbf{x}, t)$. Then, by substituting all terms into the starting equation 3.9, we see the term $\langle \delta c(\mathbf{x}, t) \delta c(\mathbf{x}', t') \rangle$ appear. This term can be expressed in terms of the fluid structure factor $S(\omega, \mathbf{q})$ [90].

$$\langle \delta c^*(\omega, \mathbf{q}, z) \cdot \delta c(\omega', \mathbf{q}', z') \rangle = \frac{m_0}{\alpha^2 \rho} S(\omega, \mathbf{q}, z, z') (2\pi)^3 \delta(\omega - \omega') \delta(\mathbf{q} - \mathbf{q}') \quad (3.10)$$

The parameter ρ represents the average density of the fluid, while m_0 denotes the average mass of the molecules, and α is the solutal expansion coefficient. By replacing this equation into 3.2, and then plugging the resulting expression into 3.9, we can perform the necessary mathematical manipulations and obtain the following expression:

$$\langle |\delta I(\mathbf{q})|^2 \rangle = \frac{4Vm_0q_0^2}{\rho\alpha^2} \left(\frac{\partial n}{\partial c} \right)^2 \sin^2 \left(\frac{q^2 z}{2q_0} \right) S(0, q) \quad (3.11)$$

The volume of the cylindrical sample is denoted by $V = A \cdot L$, and the structure factor $S(0, q)$ evaluated for $\omega = 0 \text{ s}^{-1}$, which was introduced as the *static structure factor* in Equation 2.35, is used.

After performing mathematical manipulations, we find that the intensity profile of the fluctuations is rotationally invariant. Thus, it is advantageous to perform azimuthal averaging over \mathbf{q} . As a result, Equation 3.11 becomes dependent only on the wavenumber $q = |\mathbf{q}|$.

This allows us to express the measured intensity signal as the product of the static structure factor $S(q)$ and a term known as the *transfer function* $T(q)$.

$$\langle |\delta I(q)|^2 \rangle = T(q)S(q) \quad (3.12)$$

Thus, we have successfully demonstrated that the measured intensity profile in each image contains the information regarding the static structure factor of the fluctuations. However, it is crucial to note that this was only possible after removing the macroscopic nonfluctuating background I_0 .

3.2 Dynamic Algorithm

In this section, we present the *Dynamic Shadowgraph Algorithm* that, starting from the shadowgraph image, enables the characterization of concentration fluctuations dynamics [30]; [61]. By employing the Shadowgraph technique, elaborated upon in the preceding section, the intensity of concentration fluctuations can be quantified through the I_m series of N images. From this series, the structure function can be extracted, providing insight into the underlying dynamics of the system.

In the classical implementation of the Dynamic Shadowgraph algorithm [68], the structure function is obtained through a three-step process. Firstly, the differences among all pairs of images are evaluated. Next, the power spectra of these differences are computed. Finally, the power spectra are averaged over all the pairs of images acquired with the same time delay. This procedure can be precisely defined as follows:

$$\delta I(q, \Delta t) = \frac{1}{N-m} \sum_{n=m}^{N-1} |F_{xy}(I_{n-m} - I_n)|^2 \quad (3.13)$$

where F_{xy} is the bidimensional Fast Fourier Transform (FFT) of images in space, and the indices n and m span the range from 0 to $N-1$. The modulus " $|\dots|$ " applies to each wave vector component of the FFT. The parameter Δt denotes the time delay between the I_{n-m} and n th image I_n , and is fixed for a given value of m .

In order to analyze the dynamics of fluctuations, processing image differences is more effective than subtracting the average intensity i_0 (Eqn. 3.12). While the underlying physics remains the same as the method discussed in the previous paragraph, we have chosen to treat the static and dynamic components separately for clarity. The equation 3.13 can be related to the structure factor through the following relation.

$$\delta I(q, \Delta t) = S(q)T(q) \cdot (1 - g(q, \Delta t)) \quad (3.14)$$

the intermediate scattering function, denoted by $g(q, \Delta t)$, represents the correlation function which we have explained in the section 2. When analyzing a set

of images captured at a high framerate compared to the dynamics we wish to study, the images can be temporally correlated with each other. If m is small, the time separation between the images m and $n - m$ is also small, resulting in a high correlation between them and $g(q, \Delta t)$ being approximately equal to 1. Conversely, as m becomes larger, the time lag between the analyzed images also increases, leading to the images being fully decorrelated and $g(q, \Delta t)$ approaching 0. By monitoring the time evolution of the fluctuations through the changes in $g(q, \Delta t)$, we can characterize their dynamics.

The computation of the structure function involves a series of calculations including differences, FFTs, and averages, which can be time-consuming. However, to speed up this process, these operations can be efficiently performed on a GPU in parallel [54]. In addition, the approach can be optimized by exploiting the linearity of the FFT and the available hardware memory, as described in ref. [21]. The algorithm for Eqn. 3.13 can be divided into two steps. Firstly, all FFTs $\tilde{I}_n = F_{xy}(I_n)$ of the images I_n are calculated and stored in the local memory. Secondly, each matrix $\delta I(q, \Delta t)$ is evaluated by averaging differences of the FFTs of images $(\tilde{I}_{n-m} - \tilde{I}_n)$, instead of FFTs of image differences $F_{xy}(I_{n-m} - I_n)$, which exploits the linearity of the FFT operation. This approach reduces the number of operations required, as the matrices \tilde{I}_n can be used for different Δt in $\delta I(q, \Delta t)$, resulting in a reduction of FFTs from $O(NN)$ to $O(N)$, although the overall algorithm still has a computational complexity of $O(NxN)$, due to the m time delays and the sum over $(N - m)$ images needed to obtain each matrix $\delta I(q, \Delta t)$ from Eqn. 3.13.

In the paper of Cerchiari et al. [61], they propose a novel approach to reduce the global computational complexity of the algorithm to $O(N - \log_2(N))$, using the Wiener–Khinchin theorem [23]. This theorem states that, for a stationary random process, the autocorrelation function can be calculated by the power spectrum (in time) of the process. This approach significantly reduces the computational complexity of the algorithm, improving its efficiency in calculating the structure function. By expanding the square modulus operation of Eqn. 3.13, we get

$$\delta I(q, \Delta t) = \frac{1}{N - m} \sum_{n=m}^{N-1} [|\tilde{I}_{n-m}|^2 + |\tilde{I}_n|^2 - 2Re(\tilde{I}_{n-m}^* \cdot \tilde{I}_n)] \quad (3.15)$$

In this equation, the symbol "*" denotes complex conjugation. The first term of the sum, $|\tilde{I}_{n-m}|^2$, represents the average of the first $(N - m)$ spatial power spectra, while the second term, $|\tilde{I}_n|^2$, represents the average of the last $(N - m)$ spatial power spectra. Both terms have a computational complexity of $O(N)$, which means that they require computing resources proportional to the size of the input data.

The third term, which is represented by the product $\tilde{I}_{n-m}^* \cdot \tilde{I}_n$, corresponds to the autocorrelation function of the image FFTs. This term is the only one in equation 3.15 that has a computational complexity of $O(NN)$, which means that it requires computing resources proportional to the square of the size of the input data.

However, we can take advantage of the Wiener–Khinchin theorem [49] to evaluate the autocorrelation function via the power spectrum in the temporal frequency Fourier space. This allows us to use the FFT algorithm to reduce the computational complexity from $O(NN)$ to $O(N \log_2(N))$. The speedup provided by this approach is significant and can make a real difference in practice.

Chapter 4

Free Diffusion: theory and Simulation of Non-Equilibrium Fluctuation in a strongly stratified sample

This section presents the findings of research into non-equilibrium fluctuations during free diffusion phenomena. The study focuses on the investigation of diffusion at the mesoscopic scale in a solution of water and glycerol, where the glycerol concentration profile is strongly stratified and nonlinear. The investigation of non-equilibrium fluctuations in the presence of large density gradients is challenging because analytic descriptions of static and dynamic statistical properties of fluctuations are not feasible. However, it is essential to study non-equilibrium fluctuations under non-ideal conditions because most natural and technological diffusion processes occur under non-ideal transient conditions with large gradients and in the presence of non-linearities.

Fortunately, experiments and simulations can quantitatively characterize these systems, paving the way for the development of new theoretical models. This research is performed in the framework of the Giant Fluctuations and TechNES projects of the European Space Agency, which study non-equilibrium fluctuations in complex fluids during diffusion processes under microgravity conditions. The project investigates transient and stationary diffusion processes in multi-component fluids, where stability on Earth is hindered by the presence of

double diffusion processes that lead to convective motions even in the presence of an initially stable density profile.

Non-equilibrium fluctuations are typically investigated using light scattering techniques, including Near Field Scattering, Dynamic Shadowgraphy, and Differential Dynamic Microscopy [30], [17]. These optical methods work by illuminating the sample with light and collecting the scattered light on a sensor. The light collected by the sensor is a superposition of the contributions of the light scattered by layers of the sample that can be characterized by different thermophysical properties depending on the local concentration.

For small gradients, the dependence of thermophysical properties on concentration can be neglected, but for larger gradients, a non-trivial modeling of properties of the stratified fluid is required. As a first approximation, the contributions arising from different layers can be assumed to be uncorrelated, and the modeling of the scattered intensity can be obtained by integrating the intensity of the scattered light across the sample thickness. This approximation holds when the wavenumbers are significantly larger than the critical wavenumber associated with the finite thickness of the sample. Non-equilibrium fluctuations are expected to be correlated in the direction parallel to the gradient when the correlation length is of the order of the inverse wavenumber [12]. A proper modeling of the light scattered at small wavenumbers would require taking these correlations into account.

The goal of this work is to investigate non-equilibrium concentration fluctuations during free diffusion in a mixture of water and glycerol subjected to strong concentration gradients. Experiments are performed in an isothermal configuration where two mixtures of water-glycerol at different concentrations are initially brought into contact in the stable configuration where the denser mixture lies at the bottom of the sample cell [30].

After discussing the static and dynamic structure factors for an ideal thin layer of a binary mixture with a uniform concentration gradient in Chapter 2, we can extend our modeling to strongly stratified samples. In this case, we consider a superposition of thin layers of fluid with varying concentration gradients.

In Chapter 3, we described the Shadowgraph optical technique and the analysis algorithm employed to measure the static and dynamic structure factors. However, measuring the structure factor of fluctuations in a layered sample using

this optical technique poses a challenge: due to the variations in the structure factors and intermediate scattering functions across different layers, it becomes imperative to establish and quantify a comprehensive global structure factor and intermediate scattering function. This is essential for an accurate assessment of the overall statistical features of the Non Equilibrium Fluctuation using dynamic light scattering techniques.

To overcome this challenge, we need to numerically characterize the macroscopic gradient and concentration profiles of the sample along the z -coordinate. This step will enable us to calculate expressions for the static and dynamic structure factors of the stratified sample and compare them with experimental data.

4.1 Macroscopic State: Free Diffusion

When two miscible fluids with different concentrations are brought into contact, particles tend to move from the more concentrated fluid to the less concentrated one and, in the absence of convection, the process can be described by a diffusion equation. In this section, we introduce the concept of free diffusion, which is a diffusive process occurring between two layers of liquid of infinite thickness. In practice, free diffusion can be achieved in finite systems, provided that the concentration in the areas farthest from the contact surface between the two fluids remains unchanged during the diffusion process. Under these conditions, this assumption is valid only for a certain time interval after the diffusion process begins, depending on the size of the sample in the vertical dimension and the mutual diffusion coefficient D . Having simulated the evolution of the concentration profile under different conditions of sample thickness and diffusion coefficients, it was observed that, for systems under the conditions we studied, the free diffusion condition is always valid for times t less than 320 *min*.

Our goal in this section is to quantitatively characterize the time evolution of the concentration profile $c(x, y, z, t)$ of a solution undergoing a free diffusion process. We have a system consisting of two horizontal layers of a binary liquid mixture with different concentrations that are brought into contact at time $t = 0$ s. The mixture is in a gravitationally stable configuration where the denser phase is layered at the bottom of the lighter one, allowing mixing to occur only through a diffusive process.

To obtain quantitative information about the concentration profile $c(x, y, z, t)$ and the gradient profile $\nabla c(x, y, z, t)$, we can formalize the problem using the one-dimensional diffusion equation for concentration, as the system exhibits symmetry with respect to x and y coordinates ($\frac{\partial}{\partial y} = 0$ and $\frac{\partial}{\partial x} = 0$). When the diffusion coefficient depends on the concentration, the resulting equation becomes nonlinear

$$\frac{\partial c}{\partial t} = \frac{\partial}{\partial z} \left(D(c) \cdot \frac{\partial c}{\partial z} \right) \quad (4.1)$$

In order to solve the equation, we must make the dependence of c on $D(c)$ explicit and establish the initial and boundary conditions. For $D(c)$, we have employed a polynomial function that effectively characterizes a water-glycerol mixture that is relevant to the research presented in this paper [9], which works for solutions at standard condition, over all range of c .

$$D(c) = (10,25 - 13,08 \cdot c + 8,62 \cdot c^2 - 17,65 \cdot c^3 + 11,98 \cdot c^4) \cdot 10^{-06} \text{cm}^2/\text{s} \quad (4.2)$$

In the case of a free diffusion process the initial condition is a step function:

$$c(z, t = 0\text{s}) = \begin{cases} c_1, & z \in (0, \frac{h}{2}) \\ c_2 & z \in (\frac{h}{2}, h) \end{cases} \quad (4.3)$$

where $t_0 = 0$ is the initial time and h is the thickness of the two superimposed layers.

To finish setting up the problem we need to specify the boundary conditions. In our case the walls of the sample are impermeable to mass, this results in the condition:

$$\frac{\partial c}{\partial z} = 0 \Big|_{z=0; z=h} \quad (4.4)$$

In order to obtain the time evolution of the concentration profile during the diffusion process, we utilized the MatLab PDE solver to numerically solve Equation (4.1), while specifying the initial and boundary conditions as given by Equations (4.3)-(4.4). In the scenario where an initial extremely large gradient is

present (95% glycerol against pure water), the concentration and gradient profiles exhibit significant asymmetry during their time evolution, which can be attributed to the non-linearity of Equation (4.1), as depicted in Figure 4.1a,c.

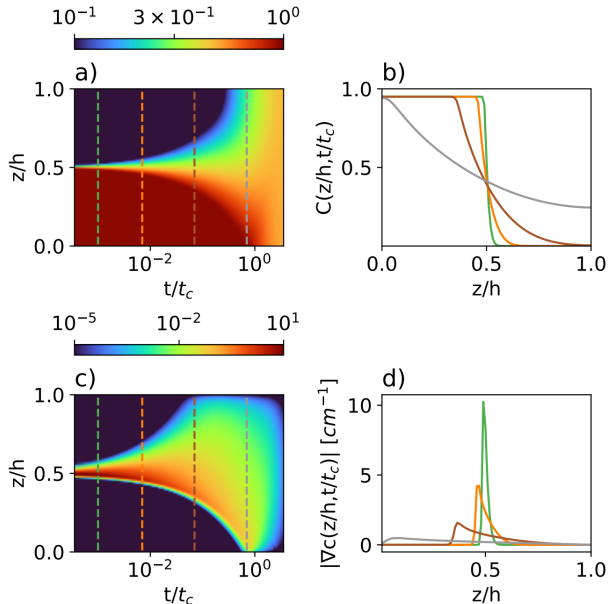


FIGURE 4.1: Time evolution of concentration $c(z,t)$ and gradient $|\nabla c|$ profiles with initial condition: $c_1 = 95\%$ and $c_2 = 0\%$. a) $c(z,t)$ represented by a colour map ranging from blue (low concentration) to red (high concentration). The colour scheme (top colour bar) is on a logarithmic scale; the time is normalised to $t_c = 3.16 \cdot 10^5$ s, while the z -coordinate is normalised to the height of the sample h . b) Vertical sections of Fig. a) at four different times $t/t_c = 10^{-3}$ (green); 7×10^{-3} (orange); 7×10^{-2} (burgundy); 7×10^{-1} (grey), marked in panel a) with the same colour scheme. c) $|\nabla c|$ corresponding to concentration profile plotted in a) (same horizontal and vertical axes). The colour map (top colour bar) is logarithmic. d) Vertical sections of Fig. c) at the same times marked in panel a) with the same colour scheme.

This result presents a stark contrast to the scenario of small gradients, where the diffusion equation assumes $D(c)$ to be constant. In this case, Equation (4.1) reduces to Fick's second law $\partial c / \partial t = D(\partial^2 c / \partial z^2)$ and exhibits symmetry around the interface position $z/h = 1/2$ at all times. However, in our case, it is apparent

that although the concentration and gradient profiles initially display symmetry along the z -coordinate, this symmetry is gradually lost as the macroscopic state evolves, leading to pronounced asymmetry.

We chose to normalise the time variable with a characteristic "average" diffusive time t_c which indicates the time constant of the slowest mode $q_s = \frac{\pi}{h}$ in the decomposition into normal modes of the diffusion equation. It's defined by

$$t_c = \frac{h^2}{\langle D(c) \rangle \pi^2} \quad (4.5)$$

where we used the average diffusion index $\langle D(c) \rangle$ within the fluid. Approximating the diffusion coefficient as $D = \langle D(c) \rangle$, t_c is the time needed for the slowest mode to reach $1/e$ of its initial value. This approximation is only used to define the normalisation time constant.

Observing the figure 4.1, one can see that the central region involved in diffusive remixing, increases as time elapses, ultimately encompassing the entire sample (uniform concentration). This characterization of the macroscopic state is essential for analyzing and interpreting experimental results, particularly in the context of strongly stratified samples.

4.2 Static Stratified Structure Factor

To evaluate the static structure factor of a thick layer in a strongly stratified fluid, we can combine the equation 2.35 and the results of the previous section regarding the macroscopic state, and add up the contributions to the static power spectrum determined by each layer, which is characterized by its unique thermophysical properties. This approach enables us to define a structure factor that is averaged across the thickness of the sample. This averaged quantity can be easily compared to experimental results.

To obtain an expression for the average structure factor, we can integrate $\tilde{S}(q)$ across the sample thickness. Assuming that our system is far from equilibrium, such that $S_{eq} \ll S(q)$ and $\nabla c_{grav} \ll \nabla c$, we can define the *Static Stratified Structure factor* using the relation:

$$S(q) = \int_0^h \frac{dz}{h} \tilde{S}(q) = \int_0^h \frac{dz}{h} \frac{S_{eq}}{\nabla c_{grav}} \left[\frac{\nabla c}{1 + \left(\frac{q}{q_{ro}}\right)^4} \right] \quad (4.6)$$

Along the z -coordinate, the ratio $S_{eq}/\nabla c_{grav}$ remains constant. As a result, it is possible to numerically integrate the static structure factor, which yields the result shown in Fig. 4.2. This figure also illustrates how the various layers contribute to the final outcome.

It is evident from the plot that integrating $S(q)$ over the entire thickness of the

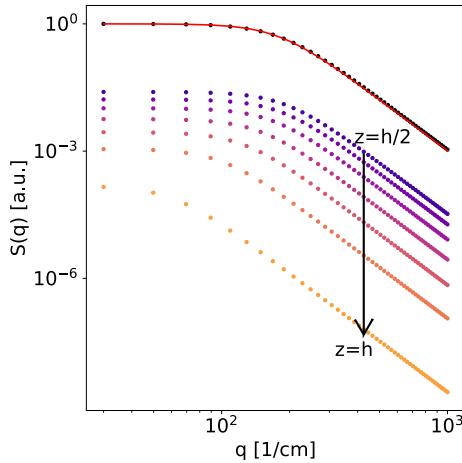


FIGURE 4.2: Simulated static structure factor $\tilde{S}(q)$ as function of wavenumber q for initial condition $c_1 = 95\%$ and $c_2 = 0\%$ and at diffusion time $t/t_c = 0.07$ (~ 350 min after the start of evolution). Different colours represent $\tilde{S}(q)$ at different z -coordinates (as indicated by the arrow). The black data are the integral of $\tilde{S}(q)$ layer by layer, over z , Eqn. (4.6), the red solid line is the fit with the model of Eqn. (4.7).

sample (black data points) exhibits a trend similar to the one integrated over the central thin layers (purple data points), which provide the largest contributions to the average. Therefore, the contributions of the different layers have a minimal impact on the shape of the stratified static structure factor. We can use the

following model to interpolate the stratified structure factor:

$$\frac{S(q)}{S(0)} = \frac{1}{1 + \left(\frac{q}{q_{ro}}\right)^4} \quad (4.7)$$

which allows to estimate the effective roll-off wavenumber determined by the stratification. It is important to note that in our derivation of Eqn. (4.6), we made the assumption that the contributions to the integrated structure factor from each layer are independent, which implies that non-equilibrium fluctuations are not correlated in the direction of the macroscopic gradient, which in our case is the vertical direction. However, it has been shown that non-equilibrium fluctuations are indeed correlated in the vertical direction, with a correlation length similar to that in the direction perpendicular to the concentration gradient [10]. However, it is possible to assume that the correlation between contributions to the integrated structure factor determined by different layers is negligible when the condition $q \gg 2\pi/h$ is met [89]. It is worth noting that the smallest wavenumber for the results presented in Fig. 4.2 is 50 cm^{-1} , which is significantly larger than the value of $2\pi/h \approx 6 \text{ cm}^{-1}$ associated with the finite size of the sample.

4.3 Dynamic Stratified Structure Factor

To obtain an expression for the Dynamic Stratified Structure Factor $S(q, \Delta t)$, we can employ a similar approach to the one used for the *Static Stratified Structure Factor*. We achieve this by averaging contributions from different layers. In the dynamic case, the stratification of the sample leads to a dispersion of the relaxation rate of non-equilibrium fluctuations at a fixed wavenumber q . This is due to the dependence on the concentration of the diffusion coefficient and the roll-off wavenumber in Eqn. (2.41). As a result, it is more convenient to use the relaxation rate γ as a suitable integration variable for the stratified structure factor, rather than the z coordinate.

$$S(q, \Delta t) = S(q) \cdot \int_{\gamma_m}^{\gamma_M} G(\gamma) \exp(-\gamma \Delta t) d\gamma \quad (4.8)$$

where $G(\gamma)$ is the probability density function of decay rates γ within the sample while γ_m and γ_M are the minimum and maximum decay rates within the sample, respectively.

We can then write the *Dynamic Stratified Structure Factor* in the form $S(q, \Delta t) = S(q) \cdot g(q, \Delta t)$, where we have defined the *stratified correlation function*:

$$g(q, \Delta t) = \int_{\gamma_m}^{\gamma_M} G(\gamma) \exp(-\gamma \Delta t) d\gamma \quad (4.9)$$

Physically, the function $g(q, \Delta t)$ results from the superposition of all $\tilde{S}(q, \Delta t)$, which describe the correlation dynamics of non-equilibrium fluctuations (NEFs) occurring at different layers, and therefore at different relaxation rates γ .

To develop a suitable model to represent $g(q, \Delta t)$, it is necessary to identify the function $G(\gamma)$ that adequately describes experimental results. In this study, we adopt a Uniform Distribution (UD) model, assuming that $G(\gamma)$ is uniformly distributed between a minimum relaxation rate γ_m and maximum relaxation rate γ_M . While this simple approximation is not strictly compatible with the asymmetry of the concentration profiles, as discussed in the section on the macroscopic state, it provides a remarkably better agreement between the theoretical and experimental time correlation functions compared to the thin-layer model where the concentration gradient is uniform, as shown in Eqn.(2.40).

Integrating Eqn.(4.9) with the UD model enables us to derive an analytic expression for the stratified correlation function $g(q, \Delta t)$.

$$g(q, \Delta t) = \frac{-e^{-\gamma_M \Delta t} + e^{-\gamma_m \Delta t}}{\Delta t (\gamma_M - \gamma_m)} = \exp(-\Gamma \Delta t) \cdot \frac{\sinh(\sigma \Delta t)}{\sigma \Delta t} \quad (4.10)$$

where

$$\Gamma = \frac{\gamma_M + \gamma_m}{2} \quad (4.11)$$

$$\sigma = \frac{\gamma_M - \gamma_m}{2} \quad (4.12)$$

The form of Eqn.(4.10) is particularly appealing since it expresses the correlation function as a single exponential relaxation, multiplied by a hyperbolic sine cardinal function that characterizes the dispersion of relaxation times. When

$\sigma \sim 0$, we obtain the ideal single exponential relaxation for a thin layer, as in Eqn.(2.40), where NEFs relax with a single characteristic time.

To obtain quantitative parameters characterizing the sample, it is necessary to investigate the theoretical dependence of Γ and σ on q . In the thin-layer case, the diffusion coefficient D and the roll-off wavenumber q_{ro} are the two parameters that determine the quantitative dependence of γ on q , as shown in Eqn.(2.41).

In the thick sample case, the new variables $\Gamma(q)$ and $\sigma(q)$ are linear combinations of the decay rates $\gamma_m(q)$ and $\gamma_M(q)$, which have the same dependence on q as in the thin-layer case, as given in Eqn.(2.41). Therefore, a linear combination of these rates does not change the dependence on q . By combining Eqns.(4.11), (4.12) with Eqn.(2.41), it is possible to determine the dependence of Γ and σ on q .

$$\Gamma(q) = \left(\frac{D_M + D_m}{2} \right) q^2 \cdot \left[1 + \frac{D_M \cdot q_M^4 + D_m \cdot q_m^4}{(D_M + D_m) \cdot q^4} \right] \quad (4.13)$$

$$\sigma(q) = \left(\frac{D_M - D_m}{2} \right) q^2 \cdot \left[1 + \frac{D_M \cdot q_M^4 - D_m \cdot q_m^4}{(D_M - D_m) \cdot q^4} \right] \quad (4.14)$$

Where D_M and q_M are the diffusion coefficient and roll-off wavenumber of the thin layer with the maximum decay rate γ_M , while D_m and q_m are the ones for the layer with the minimum decay rate γ_m . It is possible to simplify the notation by introducing the parameters

$$D_\Gamma = \left(\frac{D_M + D_m}{2} \right) \quad (4.15)$$

$$q_\Gamma^4 = \frac{D_M \cdot q_M^4 + D_m \cdot q_m^4}{(D_M + D_m)} \quad (4.16)$$

$$D_\sigma = \left(\frac{D_M - D_m}{2} \right) \quad (4.17)$$

$$q_\sigma^4 = \frac{D_M \cdot q_M^4 - D_m \cdot q_m^4}{(D_M - D_m)} \quad (4.18)$$

so that Eqn. (4.14) becomes:

$$\Gamma(q) = D_{\Gamma} q^2 \cdot \left(1 + \left(\frac{q_{\Gamma}}{q} \right)^4 \right) \quad (4.19)$$

$$\sigma(q) = D_{\sigma} q^2 \cdot \left(1 + \left(\frac{q_{\sigma}}{q} \right)^4 \right) \quad (4.20)$$

D_{Γ} and D_{σ} represent respectively the mean value and the width of the distribution of the true diffusion coefficients present in the stratified sample, Eqn. (4.2), as confirmed by both simulations (Fig. 4.3) and experimental data (Fig. 7.3). The wavenumber q_{Γ} represents an average of the two wavenumber q_m and q_M , weighted by the smallest and largest diffusion coefficients of the systems D_m and D_M , while q_{σ} is analogously related to the wavenumber difference.

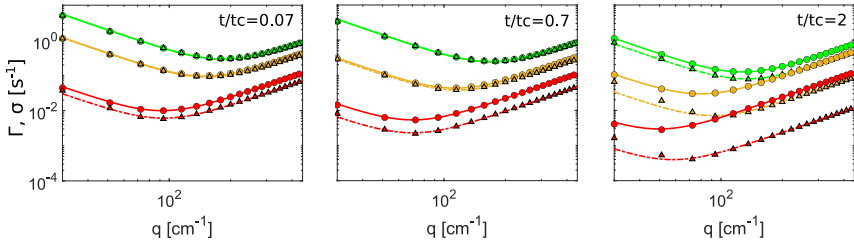


FIGURE 4.3: Simulated dependence on q of the mean relaxation rate Γ (circle) and of its dispersion σ (triangle). Data are evaluated at the instants $t/t_{cm} = 0.07$, $t/t_{cm} = 0.7$ (as in Fig. 4.2) and $t/t_{cm} = 2$. The different colours represent different initial conditions: $c_1 = 95\%$ and $c_2 = 80\%$ (red); $c_1 = 95\%$ and $c_2 = 40\%$ (orange); $c_1 = 95\%$ and $c_2 = 0\%$ (green). The solid lines are the fit of $\Gamma(q)$ with Eqn. (4.19), while the dashed lines are the fit of $\sigma(q)$ with Eqn. (4.20).

Figure 4.3 shows the trends of $\Gamma(q)$ and $\sigma(q)$, calculated by fitting the numerically generated data of *Dynamic Stratified Structure Factor* (circles and triangles), Eqn. (4.8) with the model of Eqn. (4.10) (solid and dashed lines). The numerically generated data are calculated using in the integral Eqn.4.8 the relaxation rate distribution $G(\gamma)$; it was calculated on the macroscopic state simulated

in the section 4.2. The results of the fit are shown at three different initial concentrations (different colors), after three different t/t_c from the start of diffusion (different panels).

In the panel $t/t_c = 0.07$, for large concentration differences between the two initial mixtures (green symbols) the values of σ (triangles) are perfectly superimposed on those of Γ (circles). This means that for each q , the dispersion of $G(\gamma)$ is so large that it is comparable to the mean value Γ . As the difference between the initial concentration conditions decreases (orange and red data), the difference between Γ and σ increases. This becomes particularly evident for $c_1 = 95\%$ and $c_2 = 80\%$ (red symbols), where the mean value of Γ relaxation rates is lower than in the green case, and where σ dispersion (red triangles) is distinctly lower than Γ (red circles).

In addition to the previous considerations regarding the different concentration curves, we can also comment on the time evolution of the $\Gamma(q)$ and $\sigma(q)$ curves. As time progresses, the stratification conditions change, as the system approaches a uniform concentration equilibrium state. Across the various panels, it can be observed that both the $\Gamma(q)$ and $\sigma(q)$ curves get further and further apart as t/t_c increases.

The panels at $t/t_c = 0.07$ and $t/t_c = 0.7$ exhibit similarities since the system has just emerged from the free diffusion condition, and the stratification remains similar under both conditions. However, as time increases further ($t/t_c = 2$), the differences in stratification become apparent for all concentrations. Having simulated several time instants t/t_c , our simulations show that it is not possible to consider data acquired at time instants $t/t_c > 0.07$ under the same stratification conditions, making it impossible to average the coefficients found in the result discussion section.

In order to compare the dispersion of samples with different stratification conditions in a quantitative way, a significant dimensionless parameter is the *stratification index*:

$$SI \equiv \frac{D_\sigma}{D_\Gamma} \quad (4.21)$$

The values of the *stratification index* extracted from the data shown in figure 4.3 are, for $t/t_c = 0.07$: $SI_{95\%0\%} = 0.96$, $SI_{95\%40\%} = 0.90$ and $SI_{95\%80\%} = 0.66$; for

$t/t_c = 0.7$: $SI_{95\%0\%} = 0.95$, $SI_{95\%40\%} = 0.85$ and $SI_{95\%80\%} = 0.43$; for $t/t_c = 2$: $SI_{95\%0\%} = 0.58$, $SI_{95\%40\%} = 0.18$ and $SI_{95\%80\%} = 0.10$.

The theoretical Stratification Index during free diffusion ($t/t_c < 0.07$) can also be determined using the reference values of the diffusion coefficient for the layer above and the layer below (under the initial concentration conditions), calculated via Eqn. (4.2). This evaluation of the reference stratification indices leads to the values: $SI_{95\%0\%}^{ref} = 0.96$, $SI_{95\%40\%}^{ref} = 0.90$ and $SI_{95\%80\%}^{ref} = 0.67$, in complete agreement with the values evaluated for $t/t_c = 0.07$, when the sample is in the free diffusion regime.

Chapter 5

Free Diffusion: Comparison of the Uniform Distribution model with the cumulant method and with the Schulz distribution

The cumulant method is often used in dynamic light scattering experiments to determine the size distribution of particles undergoing diffusion at equilibrium. This method is based on the principle that particles of different sizes contribute to the time autocorrelation function with different relaxation times.

In this chapter, we initially expound the Cumulant Method theoretical basis, referring to their critical discussion in the work by Frisken [37]; then we show the computational confirmations that have deepened and strengthened this type of analysis with Mailer's work [55]; finally, we apply the achievements made in this field to the NEFs field, the subject of this thesis, highlighting the changes we had to adopt, in order to improve the results.

5.1 Cumulant Method theoretical basis

The method of cumulants for the analysis of dynamic light-scattering (DLS) data was first introduced by Koppel in 1972 [48]. In that years, the method allowed for obtaining information about the distribution of decay rates for polydisperse samples from the scattered intensity correlation function.

To elucidate the methodology employed in this study, we refer to Berne and Pecora's book [62] where the focus is on describing solutions of polymers that are neither infinitely dilute nor monodisperse. In such cases, the superposition between light waves scattered by different molecules becomes significant.

We start from the equation 4.9, which is valid for any dispersed sample analyzed using light scattering techniques. It should be noted that this formula for the correlation function is applicable only if one has reason to believe that the function $G(\gamma)$ accurately represents the dispersion of the sample under investigation. However, in most cases, especially for biological molecules, the distribution of weights or sizes is unknown, and then the dispersion is unknown. The method of cumulants aims to derive a well-defined "mean" from the sample and estimate the degree of dispersion around this mean. These quantities, which correspond to moments of the distribution function $G(\gamma)$, can be measured in certain cases by examining short-time homodyne or heterodyne correlation functions.

Starting from the equation 4.9, it is possible to take its logarithm and expand it into a series of powers of the variable t , obtaining:

$$\ln g(q, \Delta t) = 1 - K_1 t + \frac{1}{2} K_2 t^2 - \frac{1}{3!} K_3 t^3 + \frac{1}{4!} K_4 t^4 \dots \quad (5.1)$$

where

$$K_n = \left[(-1)^n \frac{d^n}{d\Delta t^n} \ln g(q, \Delta t) \right]_{\Delta t=0} \quad (5.2)$$

is the n^{th} cumulant of $g(q, \Delta t)$. The explicit forms of the first few cumulants are

$$\begin{aligned} K_1 &= \langle q^2 D \rangle = \Gamma(q) \\ K_2 &= \langle (q^2 D - \langle q^2 D \rangle)^2 \rangle = \sigma^2 \\ K_3 &= \langle (q^2 D - \langle q^2 D \rangle)^3 \rangle \\ K_4 &= \langle (q^2 D - \langle q^2 D \rangle)^4 \rangle = -3K_2^2 \end{aligned} \quad (5.3)$$

Where the operator $\langle \rangle$ stands for the average over all dispersed species in the sample, D is the diffusion coefficient and q the wave number. Since the treatise [62] deals with polymer diffusion, the decay rates at different wave numbers follow the purely diffusive law $q^2 D$ and the gravitational term in equation 4.19 is absent because in the case of polymers is negligible.

The correlation function in eqn. 5.1 is expressed as a polynomial in the delay time, which could be fitted using linear least-squares techniques [63]. However, this approach has several drawbacks, such as a lack of invariance of the parameters with increasing data points, and the need to estimate the long-time background of the intensity correlation function rather than fitting it as a floating parameter.

To overcome these limitations, in [37], the method was reformulated in terms of the *moments* of the distribution rather than the cumulants, which leads to more robust and reliable fits and permits independent fitting of the long-time background. Moreover, this approach eliminates the need to restrict the fit to a limited range of data.

First, it is possible to rewrite the correlation function in terms of the mean value of the decay rates

$$g(q, \Delta t) = \exp(-\Gamma \Delta t) \cdot \int G(\gamma) e^{(\gamma - \Gamma) \Delta t} d\gamma \quad (5.4)$$

then we can expand the exponential part of 5.4 in a series of powers in Δt , obtaining

$$g(q, \Delta t) = \exp(-\Gamma \Delta t) \cdot \int G(\gamma) [1 - (\gamma - \Gamma) \Delta t + (\gamma - \Gamma)^2 \Delta t^2 - (\gamma - \Gamma)^3 \Delta t^3 + \dots] d\gamma \quad (5.5)$$

the moments of the distribution $G(\gamma)$ are defined by

$$\mu_n = \int G(\gamma) (\gamma - \Gamma)^n d\gamma \quad (5.6)$$

Writing the correlation function in term of the moments we obtain an expansion that can be fitted without the need of taking the logarithm of the correlation function pf Eqn. 5.1

$$g(q, \Delta t) = \exp(-\Gamma \Delta t) \cdot \left(1 + \frac{1}{2} \mu_2 \Delta t^2 - \frac{1}{3!} \mu_3 \Delta t^3 + \frac{1}{4!} \mu_4 \Delta t^4 \dots \right) \quad (5.7)$$

This reformulated method enables a more satisfactory and robust fittings and allows for independent adjustment of the background noise. Additionally, there is no need to limit the range of data used for fitting.

There is a strong connection between Koppel's method and Frisken's method since the moments μ_n and cumulants K_n are closely related by their definitions (Eqns. 5.6 and 5.2, respectively). Indeed, it is possible to write the cumulants in terms of the moments, and have equality, especially at low orders where

$$\begin{aligned} K_2 &= \mu_2 \\ K_3 &= \mu_3 \\ K_4 &= \mu_4 - 3 \cdot \mu_2^2. \end{aligned} \tag{5.8}$$

5.2 Computational Confirmation

A comparison between Koppel's and Frisken's method performed by using computer generated data including noise, allowed to confirm the robustness of Frisken's nonlinear method and to highlight its limitations [55].

Data, in the form of a time correlation function of scattered light, are realistically computer-generated for a sample in which there is some spread in the distribution of decay rates $G(\gamma)$.

Mainly for mathematical convenience, in the article they generate the distribution of decay rates, following the Schulz distribution

$$G(\gamma) = \frac{1}{\Gamma} \frac{(1/\sigma_n^2)^{1/\sigma_n^2}}{(1/\sigma_n^2 - 1)!} \left(\frac{\gamma}{\Gamma}\right)^{1/\sigma_n^2 - 1} \exp\left(-\frac{\gamma}{\Gamma\sigma_n^2}\right) \tag{5.9}$$

where Γ is the mean value and $\sigma_n = \sigma/\Gamma$ the normalized standard deviation of the distribution. The Schulz function has a mathematical advantage in that its integral with respect to the variable γ yields an analytical solution. To visualize the function 5.9, in Figure 5.1 we show the graph of the distribution, fixing $\Gamma = 1$ and showing what happens as the dispersion varies in the range $0 < \sigma < 1$.

Combining the integral equation Eqn. (4.9) and Eqn. (5.9), the expression for the correlation function is:

$$g(q, \Delta t) = (1 + \sigma_n^2 \Gamma \Delta t)^{-1/\sigma_n^2} \tag{5.10}$$

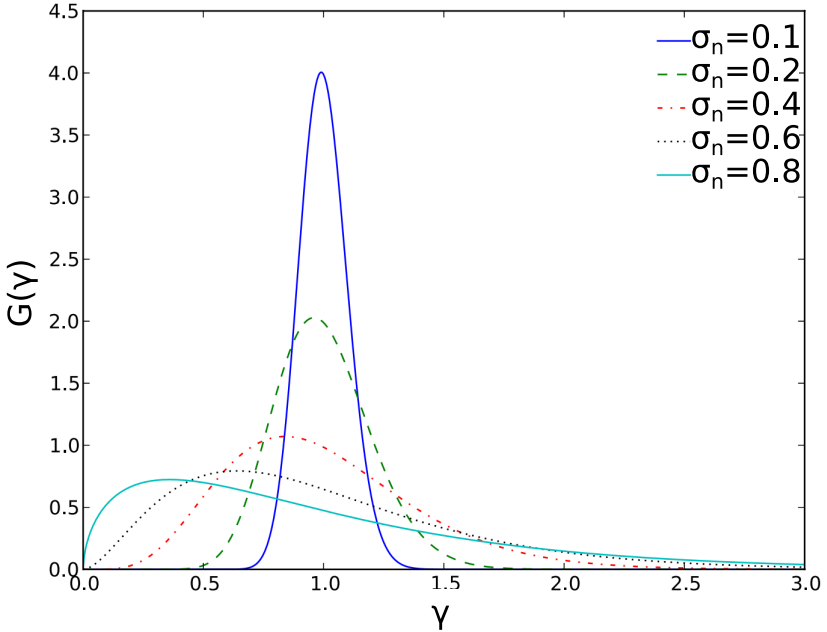


FIGURE 5.1: *The Schulz distribution, equation 5.9, for indicated values of standard deviation σ_n and $\Gamma = 1$. Image obtained from the study by Mailer et al. [55].*

If we develop this equation in a series of powers, assuming small value for σ_n , we can find the solution presented in equation 5.7. Referring to the equation 5.7, in this case, the coefficients μ_1 , μ_2 , μ_3 etc. are related to the variable σ and Γ in the following way:

$$\begin{aligned}
 \mu_2 &= \sigma^2 \\
 \mu_3 &= -2\sigma^2\Gamma \\
 \mu_4 &= 3\sigma^4 \left[1 + 2 \left(\frac{\sigma}{\Gamma} \right) \right]
 \end{aligned} \tag{5.11}$$

In the article [55], data generated with equation 5.9 are interpolated both with equation 5.7, using nonlinear methods accessible by a computer, and with equation 5.1, using a linear regression method. They conclude that if the distribution

of diffusion coefficients is not too wide, nonlinear cumulant analysis offers a simple and robust method for determining the mean and variance of the decay rates distribution of the scattered light time correlation function. However, the prospects for obtaining higher moments are not promising.

5.3 Comparison between the Uniform Distribution and Schulz models

In this section we compare the cumulant coefficients extracted from a Schulz distribution (Eqn.5.9) with those extracted from the *UD* model. We can obtain the coefficients for the *UD* model from a Taylor expansion of the hyperbolic sine cardinal function of the UD model, Eqn. (4.10):

$$\begin{aligned}\mu_2 &= \frac{\sigma^2}{3} \\ \mu_3 &= 0 \\ \mu_4 &= \frac{\sigma^4}{5}\end{aligned}\tag{5.12}$$

which, when substituted in equation 5.7, lead to having:

$$g(q, \Delta t) = \exp(-\Gamma \Delta t) \cdot \left(1 + \frac{\sigma^2}{3!} \Delta t^2 + \frac{\sigma^4}{5!} \Delta t^4 + \dots \right)\tag{5.13}$$

In comparing the coefficients 5.11 and 5.12, it is evident that the first three terms of the UD model are of even degree, while the Schulz distribution has a term of degree three. In the paper [55] it's shown that cumulant methods for a Schulz distribution are effective when the distribution is relatively narrow, with σ_n less than 0.6 [55]. However, in the free-diffusion experiments described in this paper, the dispersion of relaxation times can greatly exceed this value. For instance, in the case of the most extreme initial conditions ($c_1 = 0$ and $c_2 = 0.95$) observed in our experiments, σ_n is approximately 1. Furthermore, our simulations under these conditions demonstrate that the distribution $G(\Gamma)$ is essentially flat. As a result, in this work, we adopted a uniform distribution of relaxation times

which yields a time autocorrelation that is conceptually simpler than the one obtained with the Schulz distribution, Eqn. (5.9). This is because when $\sigma_n = 0$, a purely exponential relaxation is immediately recovered from Eqn. 4.10. In order to assess the effectiveness of the correlation function obtained using the UD model given by Eqn.(4.10) and that obtained using the Schulz model described by Eqn.(5.10), we conducted a comparison to determine which model best interpolated the numerically generated correlation function data. These data were obtained by integrating Eqn. (4.9) over the non-linear macroscopic state, which was discussed in section 4.2. This approach enabled us to consider the actual distribution of relaxation times within the sample.

In Fig.5.2, we present the correlation function $g(q, \Delta t)$ for four wave-vectors,

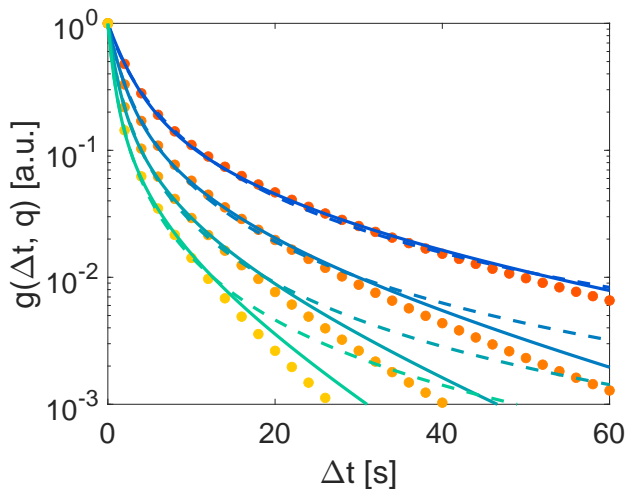


FIGURE 5.2: Simulated stratified correlation functions $g(q, \Delta t)$ (circles) as a function of delay time Δt for a sample with $c_1 = 95\%$ and $c_2 = 0\%$, at a diffusion time $t/t_c = 0.07$ (as in Figs. 7.1, and 4.3). Results are shown for different wavenumbers $q = 285, 390, 495,$ and 600 cm^{-1} , with colour ranging from red (lowest q), to yellow (highest q). Data are fitted with the uniform model Eqn. (4.10) (solid lines) and with the Schulz model Eqn. (5.10) (dashed lines).

obtained by numerically integrating Eqn.(4.9) over the non-linear concentration profile shown in Fig.4.1. We note that $g(q, \Delta t)$ is not generally a simple exponential, as in the thin layer case where it would result in a straight line. To

highlight this, we use a semilogarithmic scale for the plot. We then fit the data using the UD model of the correlation function proposed in Eqn.(4.10) (solid lines) and the Schulz function given by Eqn. (5.10) (dashed lines).

We observe that, under the extreme conditions considered, the interpolation obtained with the Schulz function exhibits significant deviations from the simulated data as the wavenumber q and delay time Δt increase. Conversely, the fit with the model given by Eqn.(4.10) agrees well with the simulated data for wavenumbers $285 < q < 600 \text{ cm}^{-1}$ and delay times $0 < \Delta t < 60 \text{ s}$, up to values of the correlation function of the order of 0.01. Although for values beyond these limits it may be necessary to use a less stringent approximation for $G(\gamma)$, the results presented in Fig.5.2 demonstrate that the UD correlation function, introduced in Eqn.(4.10), is more effective than the Schulz function, Eqn.(5.10), in describing the simulated dynamics of non-equilibrium fluctuations in a strongly stratified system, particularly when a large dispersion of decay times ($SI^{act} = 0.96$) is present.

Chapter 6

Free Diffusion: Set up and Methods

In this chapter, we outline the experimental setup and measurement methods used to investigate nonequilibrium fluctuations in the macroscopic state described earlier. The key components of the setup are a Flowing Junction Cell (FJC), an instrument designed to create two zones with distinct concentrations that are in contact but clearly separated by a sharp interface, an injection system for controlling the flows within the cell and maintaining the concentration zones, and an optical system for acquiring the images that will be analysed in the results chapter. In addition, the experimental procedures developed to inject the solutions into the cell and to acquire the shadowgraph images are explained in detail in this chapter.

6.1 Flowing Junction Cell (FJC)

Our physics experiments involved the use of a customized cell that was designed to operate under simulated microgravity conditions. This cell was originally developed by Longworth in 1950 to study diffusion processes and was later improved upon by Thomas in the 1960s and Crococo a few years ago [78], [28]. The primary materials used in the construction of the cell are non-magnetic, austenitic stainless steel, PTFE (polytetrafluoroethylene a.k.a. Teflon), and FKM (fluorocarbon elastomer a.k.a. Viton) gaskets. These materials are highly resistant to corrosion and chemical and physical deposition. The cell consists of a

3.36 cm thick sample with a stable liquid-liquid interface between miscible soluble liquids placed precisely in the middle at a height of 1.68 cm, as illustrated in Figure 6.1 c).

To better understand the cell's mechanism, we refer to the illustrations Fig.6.2

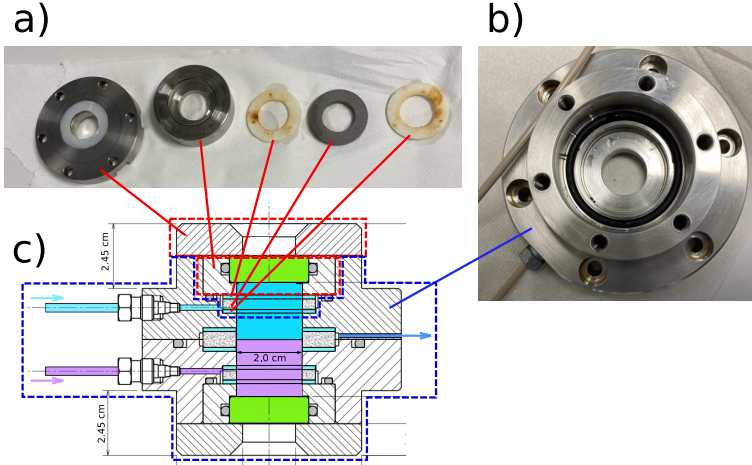


FIGURE 6.1: *photographs and schematic representations of the constituent components of the flowing junction cell utilized in our experimentation. Panel a) presents a sequential arrangement, from left to right, of the cell top shielded with polytetrafluoroethylene (PTFE a.k.a. Teflon), a sapphire crystal window fixed in its steel holder, a PTFE gasket, a porous medium of the cell top, and another PTFE and fluorocarbon elastomer (FKM a.k.a. Viton) gasket. Panel b) exhibits the lower section of the cell assembled with the components as shown in panel (a). Panel c) is a cross section of the cell along its longitudinal axis and highlights the sapphire plates responsible for determining the upper and lower limits of the sample, represented in green, and the porous septa outlined in cyan that enable radial inlet and outlet flow of mixtures within the cell, which are secured by PTFE gaskets.*

obtained from the research article by Croccolo et al. [29]. The two mixtures are continuously injected into the bottom and top chambers (Fig.6.2a), respectively, facilitated by two annular porous septa, which promote radial distribution of the inlet flow (Fig.6.2 b). The two mixtures interact at the mid-height of the cell,

and a distinct interface is maintained by continuously drawing the fluid phases out of the cell through a narrow annular slit. Sapphire cell windows have been employed to prevent any leakage or abrasion.

Once the system is prepared, an experimental run can be initiated by interrupt-

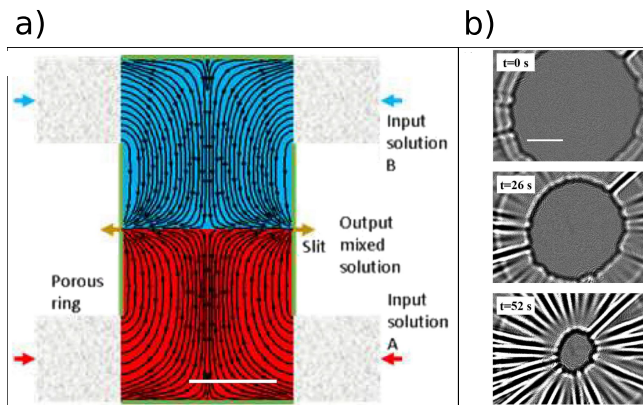


FIGURE 6.2: *schematic of the operational mechanism of the cell and accompanying images of an injection process. Panel a) portrays a vertical cross-section of the cell wherein the two fluid phases are introduced into the cell through the top and bottom porous septa. The dimensions of the white scale-bar are 10 mm. Panel b) displays images of the cell in a horizontal cross-section, obtained during the filling process. At $t = 0$ s, $t = 26$ s, and $t = 52$ s, a liquid marginally warmer than the one present in the cell is gradually injected. The white scale-bar has dimensions of 5 mm. Images obtained from the study by Croccolo et al. [29].*

ing the fluid flow, allowing the two phases to diffuse into each other through a free-diffusion process. Under these conditions, the concentration profile evolves as depicted in Figure 4.1. Our customized cell has already been utilized during parabolic flights in zero gravity, and stringent specifications were observed throughout its development and use.

6.2 Hydraulic injection circuit

In our physical experiment, we took great care to design a hydraulic injection circuit that would prevent the formation of gas bubbles in the cell. These bubbles can interfere with the concentration and gradient profiles and complicate dynamic analysis. To achieve this, we developed a strict injection procedure that allows for bubble-free injection of solutions. The circuit includes PEEK capillaries, valves, and steel piping, and a schematic is shown in Figure 6.3.

The injection mechanism involves using a syringe pump to fill the syringes with solutions under high vacuum conditions and inject them into the flowing junction cell at a constant flow rate. To ensure a bubble-free injection, we create a high vacuum in the circuit and cell by closing valves V1 and V5 and sucking from valve V2 for at least 24 hours using a vacuum pump. We then close valves V4, V3, and V2 in that order, while the vacuum pump is still running. Valve V3 is slowly opened to fill the capillaries in that section by pressure difference, taking care to ensure that the capillary connecting valve V3 to the solutions is free of air.

Next, the syringes are filled with solutions using the syringe pump with valve

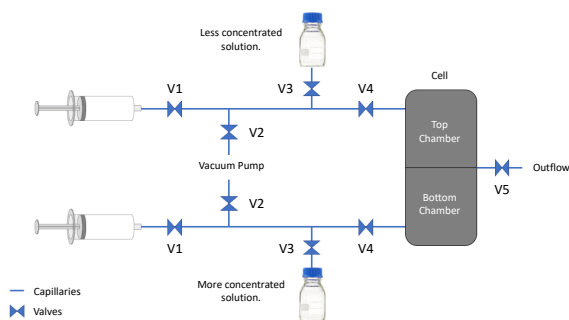


FIGURE 6.3: Schematic diagram highlighting the critical components of the solution injection mechanism.

V3 and V1 open. After filling, we flush the syringes at a rate of $1 \text{ cm}^3/\text{min}$ for

both syringes. Valve V4 is then opened, and after verifying that the cell is filled with solutions and free of bubbles, valve V5 is opened. The flow continues for approximately 20 minutes, after which valve V5 is closed, the syringe pump is stopped, and the concentration profile begins to evolve.

Our hydraulic injection circuit design and strict injection procedure have proven effective in preventing the formation of gas bubbles and ensuring a bubble-free injection of solutions, allowing for accurate concentration and gradient profiles and facilitating dynamic analysis.

6.3 Optical System

In this experiment, we used a technique called Dynamic Shadowgraph, which was explained in detail in chapter 3. This technique requires a collimated non-coherent beam of light to pass through the sample. The light source used in our setup was a Superluminescent Light Emitting Diode (Superlum, SLD-MS-261-MP2-SM) with a wavelength of $\lambda = (675 \pm 13)$ nm. The light emitted by the LED was collimated using an achromatic doublet with a focal length of $f = 150$ mm, which was placed in the focal plane of the LED.

As illustrated in Figure 6.4, dynamic shadowgraph images were acquired using an scientific-CMOS camera (Hamamatsu C13440, ORCA - Flash 4.0 V3). This camera was chosen due to its high sensitivity and low readout noise, which is ideal for imaging small fluctuations in concentration.

It is important to note that the choice of light source and camera are critical in obtaining accurate results from the Dynamic Shadowgraph technique. The Superluminescent Light Emitting Diode provided a stable and consistent light source, while the scientific-CMOS camera allowed for high-quality imaging with minimal noise.

Overall, the optical system used in this experiment was carefully chosen to ensure accurate and reliable measurements of concentration fluctuations. The use of the Dynamic Shadowgraph technique, along with the appropriate optical components, allowed for precise measurements that were crucial in our analysis.

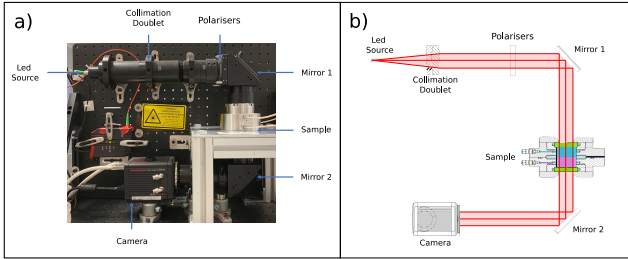


FIGURE 6.4: *Optical setup for image acquisition. Panel a) Photographs of the optical apparatus used in the experiment. Panel b) Schematic diagram of the setup: the light beam emitted by the LED source (specified in the text) is shown in red. After being collimated by the lens, the pair of polarizers adjusts its intensity; then, the beam is reflected by a first mirror, passes through the sample and is reflected by a second mirror in the camera (specifications in the text). This arrangement of the elements allowed us to optimise the space occupied by the setup.*

6.4 Methods

In this section we explain how the *Static Structure Function* $S(q)$ and the *intermediate scattering function* $g(q, \Delta t)$, defined by Eqns. 4.7 and 4.10, respectively, can be recovered from sequences of images of the sample acquired during the experiments: As already explained in the previous paragraphs (Chap. 3), the measurements are performed with Dynamic Shadowgraphy, a differential method based on processing shadowgraph images previously subtracted one to the other to get rid of their static components.

The power spectrum of the difference between two images taken at different times allows to calculate $\delta I(q, \Delta t) = \langle |I(q, 0) - I(q, \Delta t)|^2 \rangle$ where, to lighten the formalism in the equation 3.13, the brackets identify a time average. Time averaging is done on a thousand pairs of images, taken at different instants of time, but spaced at a fixed Δt . Since the system has a cylindrical symmetry, all quantities have been averaged over the azimuth angle of the wavenumber and are presented as a function only of the radial component q . We can then write the real signal we measure by adding the non-ideal contributions to the ideal equation 3.14, obtaining:

$$\delta I(q, \Delta t) = T(q)S(q) \cdot (1 - g(q, \Delta t)) + B(q) + \alpha \cdot \Delta t^2 \quad (6.1)$$

where $B(q)$ is the spectrum of the optical background and we had to add an empirical quadratic contribution in time because the system is in a non-equilibrium quasi-stationary state. It has been systematically observed that this non-stationary state generates an effect like that which occurs in the presence of a slow global drift of the collected images, that modifies the structure function with the term $\alpha \cdot \Delta t^2$. The term $T(q)$ is the *Transfer Function* and, as already explained, it characterizes the response of the optical system to a point-like perturbation of the refractive index inside the sample. For our experiment, we have used an empirical expression for $T(q)$, mutated from the one determined during the GRADFLEX project of ESA by performing an accurate calibration of the transfer function using a reference sample [84].

In the next section, results of the interpolation of data $\delta I(q, \Delta t)$ with three different models (the UD, Schulz and SE model), acquired using the Shadowgraph technique, are shown and compared with each other. Furthermore, our aim is to provide the parametric values of the scattering coefficients D_Γ , D_σ and q_{ro} .

The Fit procedure is now briefly described and consists of two steps. Firstly, data $\delta I(q, \Delta t)$ is interpolated q by q in order to extract $A(q) = T(q)S(q)$, $B(q)$ and $\alpha(q)$; by fixing q , it is possible to consider these functions as simple parameters, the only independent variable being Δt . For each model, the corresponding form of $g(q, \Delta t)$ (Simple Exponential Eqn. 2.40, Schulz Model Eqn. 5.10, Uniform Model Eqn.4.10) is used to extract the parameters.

Secondly, to compute D_Γ , D_σ and q_{ro} , a new fit in two variables ($q, \Delta t$) is required. In this second fit, parameters extracted during the first step are used. While in the first fit q was fixed and the variables $\Gamma(q)$ and $\sigma(q)$ were considered as parameters, now, by interpolating the data into the two variables ($q, \Delta t$), the q -dependence of $\Gamma(q)$ and $\sigma(q)$ is made explicit; For the UD and Schulz's model, the dependence is expressed in the equations 4.19 and 4.20, while for the simple exponential model, the decay rate $\gamma(q)$ (Eqn 2.41) changes physical meaning but has the same form as $\Gamma(q)$ (as discussed in the previous paragraphs). For simple exponential model $\sigma(q)$ is equal to zero.

We have acquired data for samples prepared under different initial concentration conditions. Furthermore, to observe the evolution of the fluctuations during the evolution of the concentration profile, we acquired measurements at different times in the evolution of the system ($t_i = t/t_c$). The conditions of measurements and the timeline are summarized in Table 6.1. For each of these times and for

c_1 vs c_2	t_c (min.)	t_1/t_c	t_2/t_c	t_3/t_c	t_4/t_c	t_5/t_c	t_6/t_c	t_7/t_c	t_8/t_c	t_9/t_c	t_{10}/t_c	t_{11}/t_c	t_{12}/t_c
20%vs0%	2.20E + 03	0.009	0.018	0.036	0.073	0.145	0.509						
40%vs0%	2.66E + 03	0.008	0.015	0.034	0.060	0.120	0.357	0.490					
80%vs0%	4.23E + 03	0.005	0.010	0.019	0.038	0.043	0.064	0.076	0.268	0.296	0.358	0.615	
90%vs0%	4.87E + 03	0.004	0.008	0.016	0.033	0.051	0.066	0.107	0.220	0.240	0.250	1.130	
95%vs0%	5.26E + 03	0.004	0.008	0.015	0.030	0.060	0.191	0.244	0.425	0.801			1.180
95%vs10%	5.83E + 03	0.003	0.007	0.014	0.027	0.055	0.110	0.211	0.241	0.278	1.040	1.290	
95%vs20%	6.53E + 03	0.003	0.006	0.012	0.049	0.098	0.195	0.216	0.303	0.418	0.542	0.737	0.877
95%vs40%	8.56E + 03	0.002	0.005	0.009	0.013	0.019	0.026	0.037	0.086	0.150	0.194	0.340	0.810
95%vs80%	2.10E + 04	0.002	0.004	0.008	0.015	0.030	0.055	0.063	0.130	0.170			

TABLE 6.1: *Index of measurements. Columns c_1 vs c_2 are the initial top and bottom concentrations of glycerol, respectively. t_c identifies the diffusive time across the thickness of the sample, after which the system exits the free-diffusion regime. The other columns represent times, relative to t_c , when measurements have been performed during the free-diffusion process*

each of the analysed concentration pairs, two sets of 2000 images at a resolution of 20482048 pixels at 16 bits were acquired at two different frame rates (10 fps and 100 fps). Due to the wide range of relaxation rates contributing simultaneously to the signal, we have adopted a processing procedure that makes use of concatenated frame-rates to reduce the amount of images and make the datasets more manageable: a faster framerate, at 100 fps, to investigate the relaxation occurring at the smallest scales, and a slower one, at 10 fps [38]. Considering the rather large diffusion times in our experiments, the system can be assumed to be in quasi steady state conditions within one measurement run, i.e. at a given time t_i/t_c . The whole procedure has been repeated three times at every initial concentration to check the repeatability of experiments and to enlarge the statistical sample of result.

Chapter 7

Free Diffusion: Results

In this chapter, we present the findings of our experiments on non-equilibrium fluctuations that occur during free diffusion between two solutions of glycerol and water with varying concentration differences. As mentioned in the preceding chapters, the system's nonlinearity is a result of the strong stratification of the sample, which necessitates the introduction of an interpretive model capable of characterizing the correlation properties of the non-equilibrium fluctuations. This model enables the characterization of the dynamics of non-equilibrium fluctuations in the presence of a broad range of relaxation times caused by the sample's strong stratification. This is in contrast to the cumulative methods usually employed in Dynamic Light Scattering experiments, which are effective when dealing with moderate dispersion of relaxation times.

In this chapter, we present the experimental results and check the effectiveness of the UD correlation function by providing an accurate evaluation of the experimental parameters.

7.1 Validation of the model

A first important verification involves the validation of the effectiveness of the model correlation function Eqn. (4.10) to fit the experimentally determined structure functions in the form described by Eqn. (6.1). Figure 7.1 (a)-(c) show $\delta I(q, \Delta t)$ for three different initial concentration conditions. Data acquired with the Shadowgraph technique at three different wave numbers q are interpolated with the SE, UD and Schulz model discussed in this work.

To evaluate the effectiveness of each model it is useful to determine the residuals $R(q, \Delta t)$, defined as the difference between the expected value from each model and the measured data, normalised to the expected value. To better quantify the information contained in the residuals, we introduce the summation over all the time delays:

$$R(q) = \sum_{\Delta t} [R(q, \Delta t)]^2 \quad (7.1)$$

From Fig. 7.1 one can appreciate that the three models work equally well in fitting the data when the difference between the concentrations is low (panel (a) and (d)), and no notable differences can be appreciated between the three models, in particular between the UD and Schulz model. This means that for a stratification index $SI < 0.30$, corresponding to the case reported in Fig. 7.1a, the stratification does not significantly influence the structure function measurements $\delta I(q, \Delta t)$. When the concentration difference in the sample is increased, some differences between the models become evident: in panel (b) $c_1 = 80\%$, $c_2 = 0\%$, with $SI^{act} = 0.79$, one cannot still distinguish between the different models, which appear to be overlapping, but looking at the residuals in panel (e), it can be appreciated that the UD and Schulz models perform better than the SE model. This feature is also clearly confirmed by the value of $R(q)$ in panel (g). This result shows that, as the stratification increases, it is necessary to modify the correlation function to take into account the dispersion of relaxation times inside the sample. Observing the residuals at $SI^{act} = 0.79$, the differences between the UD model and the Schulz one remain minimal and indicate that, in the presence of a moderate dispersion of relaxation times ($0.3 < SI^{act} < 0.8$), the Schulz distribution is also adequate to characterise the relaxation of NEFs. A pronounced difference between the Schulz model and the UD one becomes apparent at the maximum concentration difference $c_1 = 95\%$ and $c_2 = 0\%$; $SI^{act} = 0.96$ shown in panel (c). In this case, the extreme initial conditions can no longer be modelled by the Schulz model. Looking at the residuals $R(q)$ in panel (g) we observe that the difference between the models increases significantly and that UD model is the one that best interpolates the data under all the conditions described. The data shown so far exhibit an improvement in the quadratic sum of the relative residuals for three specific wave numbers.

To provide a more complete overview of the ability of the three models to

describe the data, it is necessary to compare them on all wave numbers in the observed range. Figure 7.2 (a) shows the experimentally determined structure function $\delta I(q, \Delta t)$ plotted in two dimensions as a function of all wave numbers q (vertical-axis) and of the delay time Δt (horizontal-axis) in the case $c_1 = 95\%$ and $c_2 = 0\%$. In panel (b) it is possible to observe the function $P(\Delta t)$, at three different fixed q corresponding to the horizontal sections indicated by the dashed lines in panel (a), interpolated by the three models.

To provide an integrated parameter that gives an overall information about the effectiveness of fit, we introduce the relative overall square residual averaged across all wave numbers and delay time range:

$$R_m = \frac{1}{N} \sum_q \sum_{\Delta t} [R(q, \Delta t)]^2 \quad (7.2)$$

where N is the number of independent values of $R(q, \Delta t)$ used in the summations. For the case shown in the figure, we obtain $R_m = 0.0021$ for the UD model, $R_m = 0.0032$ for the Schulz model, and $R_m = 0.0037$ for the SE model.

Table 7.1 shows the values of R_m for all the initial conditions analysed. These data confirm that for small differences in concentration, the three models perform equivalently. As the difference between c_1 and c_2 increases, the difference between the models becomes more and more evident. It is evident that the standard exponential SE is the best interpolation for the data when observing the mean-square residuals at $c_1 = 20\%$ and $c_2 = 0\%$, indicating that the dispersion of the diffusion coefficients for this concentration is negligible. On the other hand, as already confirmed for the analyses at q fixed and for the comment made to the figure 7.2, for $c_1 = 95\%$ and $c_2 = 0\%$ the difference between the models becomes more evident. Lastly, the mean square residuals for $c_1 = 95\%$ and $c_2 = 80\%$ are identical, as these measurements were extremely noisy and challenging to interpret for all three models.

Finally, the static power spectrum obtained with the three models can be observed in Fig. 7.2 c). As predicted by the simulations and detailed in the previous chapters, both the UD, Schulz and SE model show the same result for the static part. In the figure, the three static curves representing the term $S(q)T(q)$ are perfectly superimposed and in excellent agreement with the experimental $\delta I(q, \Delta t)$

TABLE 7.1: Comparison between the relative mean square residuals obtained with the UD, Schulz and SE models. c_1 and c_2 identify the concentrations of the bottom and top phase, respectively.

c_1	c_2	SI	R_m <i>UD</i>	R_m <i>Schulz</i>	R_m <i>SE</i>
20%	0%	0.132	0.0011	0.0011	0.0007
40%	0%	0.296	0.0014	0.0015	0.0017
80%	0%	0.795	0.0015	0.0016	0.0022
90%	0%	0.915	0.0021	0.0028	0.0032
95%	0%	0.956	0.0021	0.0032	0.0037
95%	10%	0.951	0.0020	0.0024	0.0030
95%	20%	0.943	0.0031	0.0037	0.0049
95%	40%	0.921	0.0028	0.0034	0.0055
95%	80%	0.674	0.0120	0.0120	0.0122

for $\Delta t = 90$ s.

7.2 Thermophysical Parameters and Discussion

The two dimensional fitting procedure adopted in this work allows to determine a single value of the average diffusion coefficient and of its dispersion for each experimental run. For times $t < t_c$ the system evolves under free-diffusion conditions, and the concentrations at the boundaries of the sample does not change in time. Under these conditions, the time evolution of the concentration profile does not influence significantly the values of D_Γ and D_σ , allowing the diffusion coefficients to be averaged over all tests and times for each experimental concentration. The fitting of the experimental data allows to estimate the values of D_M and D_m and, using Eqn. (4.15) and (4.17), to evaluate D_σ and D_Γ , which are plotted in Fig. 7.3 a) as a function of the average concentration. To achieve

a meaningful statistical relevance of the results, we have performed three measurements for each of the nine couples of concentrations shown in Table 6.1).

Experimental data are compared with the theoretical values calculated from Eqn. (4.15) and (4.17), using the theoretical values of the diffusion coefficients obtained with the empirical modelling of Eqn. (4.2). It can be observed that the average diffusion coefficient D_Γ decreases as the average concentration increases, in agreement with the theoretical prediction (dashed line), although the experimental values are systematically larger than the theoretical ones. The trend for the dispersion of the diffusion coefficient D_σ is also in agreement with the theoretical predictions, and a peak at the maximum concentration difference ($c_1 = 0$, $c_2 = 0.95$) is observed, even if the experimental data are noisy and differ substantially from the predicted ones. This difference can be also evidenced by comparing the predicted stratification index at each average concentration, with the experimental value, Fig. 7.3b). Although our Fick diffusivity data do not match exactly with the reference ones on the empirical concentration-dependence of the diffusion coefficient at 298 K derived from Bauchaudy et al. [9], see Eqn. 4.2, the trend of D_Γ , D_σ , and SI as a function of the average mass fraction of glycerol are in very good agreement with the ones derived from reference data. The deviations observed in Fig. 7.3 can be associated with the slight difference on the temperature, as well as the correlation itself. As shown in literature, one can expect deviations up to 30% between Fick diffusivity data at large mass fractions of glycerol [65],[60],[77],[32]. Propagating these deviations in the reference values depicted by the dashed lines on Fig. 7.3, not shown for legibility purposes, will lead to matching diffusivity and SI data across the complete range of mass fractions of glycerol used in our study.

Analogously to the analysis performed for D_Γ and D_σ , it is possible to extract from the experimental data the values of q_Γ and q_σ defined in the Eqns. (4.16) and (4.18), which are a linear combination of the roll-off wave-numbers q_m and q_M for the largest and smallest concentrations present inside the sample. The investigation of these two parameters allows to characterise the influence of gravity on NEFs in the presence of a significant stratification of the sample. Quite interestingly, we notice that results for time evolution of the roll-off wave number q_Γ obtained with all the initial conditions investigated in this work can be scaled onto a single curve, once they are normalised with an arbitrary constant

(Fig. 7.4). To understand the physical origin of this common behaviour, we notice that the only time-dependent term in Eqn. (2.38) is the gradient ∇c , which decreases with time proportionally to $t^{-1/2}$. Therefore, we expect that q_Γ and q_σ evolve in time according to the following expressions [81]:

$$q_\Gamma = a_\Gamma \cdot \left(\frac{t}{t_c}\right)^{-1/8} \quad (7.3)$$

$$q_\sigma = a_\sigma \cdot \left(\frac{t}{t_c}\right)^{-1/8} \quad (7.4)$$

where a_Γ and a_σ are two characteristic wave numbers that can be obtained by interpolating the time evolution of the roll-off wave numbers with Eqns. (7.3) and (7.4) for each experimental run. One can appreciate that the measured values of $q_\Gamma(t)/a_\Gamma$ are well approximated by the theoretical curve, providing an indication of the consistency of the interpretative model proposed by us. On the other hand, the trend of $q_\sigma(t)/a_\sigma$ follows the predictions only for large concentration differences (0vs90, 0vs95, 10vs95 and 20vs95), while for the small ones, the values are very noisy, Fig. 7.4b). This result can be understood by taking into account that q_σ represents the dispersion of roll-off wave numbers, which differs significantly from zero only in the presence of a significant stratification of the sample. This condition is met by the experimental results clustered around the theoretical prediction in Fig. 7.4b). Under all the other experimental conditions, the value of q_σ should be close to zero, and the fitting procedure becomes very noisy because under these conditions q_σ is not a relevant parameter to describe the system.

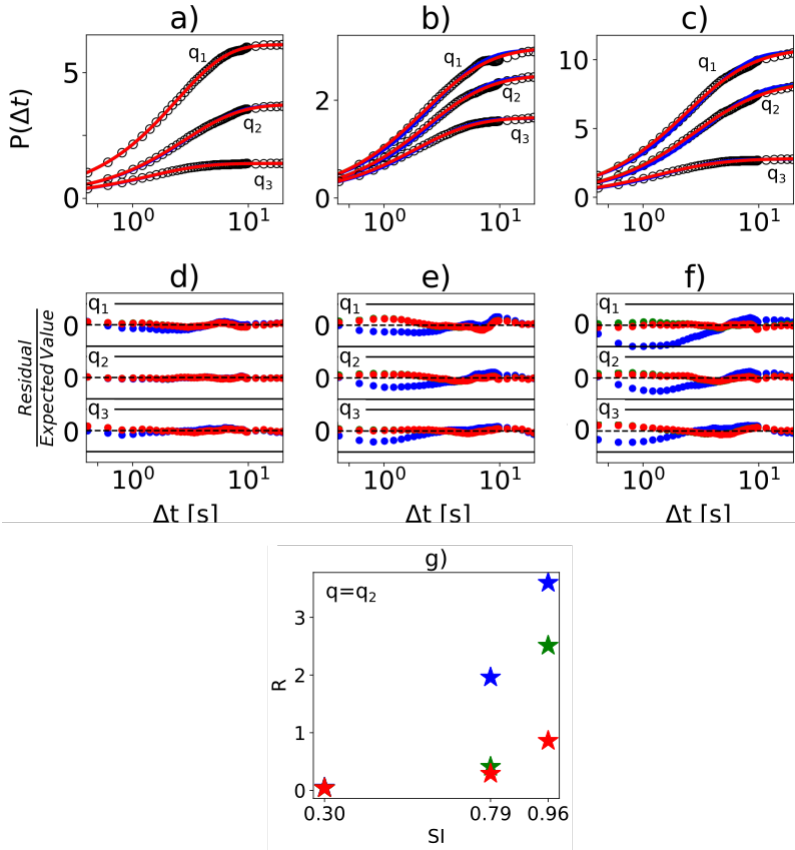


FIGURE 7.1: (a)-(c): $P(q, \Delta t) = \delta I(q, \Delta t)$ as a function of Δt , at $q_1 = 140 \text{ cm}^{-1}$, $q_2 = 200 \text{ cm}^{-1}$, $q_3 = 300 \text{ cm}^{-1}$; all measurements are made after 320 min from the start of the diffusion process, for different initial conditions: a) $c_1 = 40\%$, $c_2 = 0\%$; b) $c_1 = 80\%$, $c_2 = 0\%$; c) $c_1 = 95\%$, $c_2 = 0\%$; black circ $\delta I(q, \Delta t)$; Red solid line: UD model; green solid line: Schulz model (not visible due to the close superposition to the red line); blue solid line: SE model; (d)-(f): relative residuals corresponding to the plots above Dashed line: value 0; horizontal solid lines: $+0.1$ and -0.1 values; residuals resulting from different models are shown with the same colour scheme as in the graphs above. (g): $R(q_2)$ for the three values of SI^{ref} , plotted with the same colour scheme of the other panels.

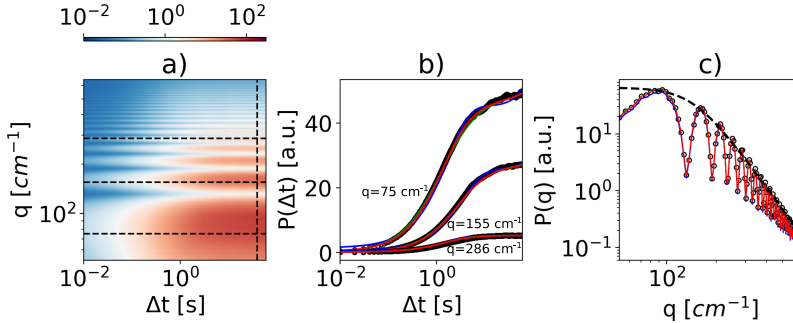


FIGURE 7.2: *a)* $\delta I(q, \Delta t)$ (colour scale indicated in the top bar) acquired for initial condition $c_1 = 95\%$, $c_2 = 0\%$, after 320 min from start of diffusion. *b)* Black dots: Structure functions corresponding to the horizontal sections of panel (a). Red solid line: our two-variable model interpolating the data; green solid line: two-variable Schulz model; blue solid line: two-variable simple exponential model. *c)* Black dots: section of panel (a) at the vertical dashed line. Red continuous line: $S(q)T(q)$ of our two-variable model; green continuous line: $S(q)T(q)$ two-variable Schulz model; blue continuous line: $S(q)T(q)$ two-variable simple exponential model; Dashed black line: theoretical result for $S(q)$.

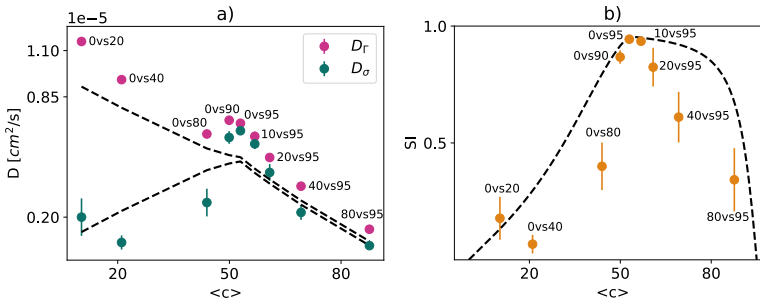


FIGURE 7.3: *a)* Values of D_Γ and D_σ as a function of the average mass concentration of the system. *b)* Values of SI as a function of the average mass concentration of the system. For both panels, the error bars are the standard deviations determined from the three repetitions of the experiments, which in some cases are smaller than the point size; the dashed black lines represent the theoretical predictions for D_Γ and D_σ and SI .

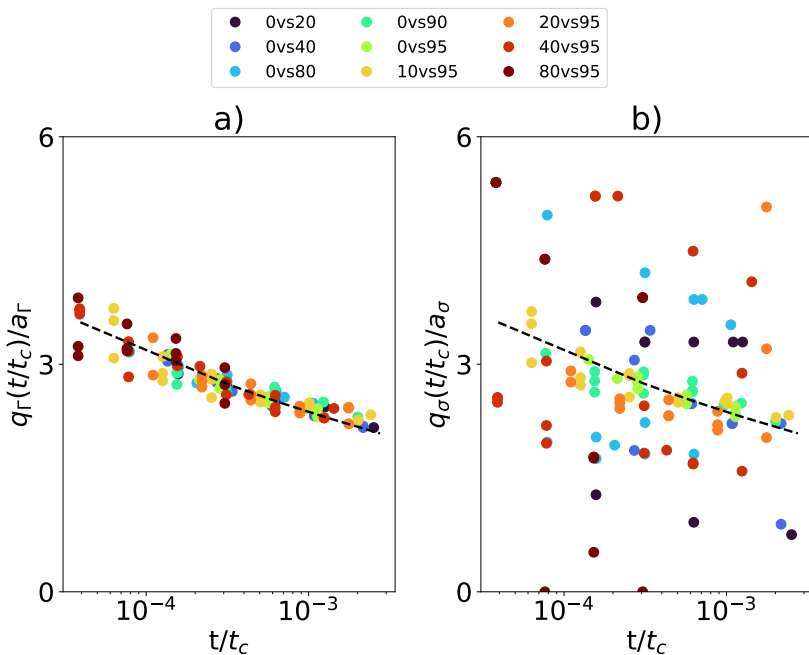


FIGURE 7.4: (a) q_Γ/a_Γ , and (b) q_σ/a_σ , plotted as a function of time. Different colours correspond to measurements performed under different initial concentration conditions (top legend). For both panels, the dashed black line represents the theoretical prediction $t^{-1/8}$.

Chapter 8

Transient Localized Rotating Structures in a Suspension of Highly Thermophilic Nanoparticles

In this chapter, we present the first part of a study focused on exploring the fluctuations that occur in a mixture of Ludox and Water. While our previous chapters examined NEFs during isothermal diffusion in a solution of water and glycerol, our next step is to study NEFs in the presence of temperature gradients. The presence of a stabilizing temperature gradients leads to long-range temperature fluctuations, which, as for concentration fluctuation, are several orders stronger than the equilibrium ones. Therefore, it is interesting to study the dynamics of systems in which concentration NEFs and temperature NEFs coexist and describe the interaction between fluctuations of different nature [88].

Moreover, the sample under investigation has several peculiarities. Ludox exhibits a strongly thermophilic behavior [19], leading to a unique stability diagram. Applying a temperature gradient to the mixture results in heat transport occurring either in a diffusive or convective regime, depending on the stability diagram coordinates of the sample. Investigating NEF in such a sample is crucial to understanding transport phenomena in fluids, which is the final goal of my research. Previous research has shown that NEFs generate a net mass transfer, corresponding to Fickian diffusion [11].

Thus, the aim of this chapter is to take a first step in this research, investigating the development of convective instabilities within the sample to determine the optimal conditions for studying fluctuations. Our findings indicate that the sample's stability is influenced by the preparation conditions, even when the applied temperature gradient is below the convective threshold. Additionally, we have identified and characterized localized convection patterns that demonstrate rotational dynamics, previously unobserved under the experimental conditions used in this study. Notably, the accumulation of particles at the cell's bottom, determined by the thermophilicity of the Ludox, should have prevented the onset of convective instabilities. This study has already produced published results [14] and lays the foundation for future investigations of NEF in systems like this.

8.1 Bénard Problem for colloidal solution

In a simple fluid at which we apply strictly vertical temperature gradients, heat flow can occur through two mechanisms, namely conduction and convection. Conduction occurs whenever there is a lack of homogeneity in the temperature of the fluid, whereas convection is induced by gravity and only takes place when a temperature gradient in the vertical direction exists, with a downward direction, exceeding a certain threshold. This threshold between conduction and convection, which define the stability of the fluid, can be evaluated by introducing a dimensionless number, the Rayleigh number (Ra), which represents the ratio between the timescale for thermal conduction and that for convective thermal transport. In case the fluid is confined in a layer of height h that is heated from below, commonly known as the Bénard problem [22], the Rayleigh number is given by

$$Ra = \frac{g\beta_T\Delta Th^3}{D_{Th}\nu} \quad (8.1)$$

where g represents the magnitude of the gravitational acceleration, β_T refers to the thermal expansion coefficient, Δt is the temperature difference between the upper and lower boundaries of the fluid, D_{Th} denotes the thermal diffusivity, and ν represents the kinematic viscosity of the fluid. It is worth noting that when Ra is less than a critical value ($Ra_c = 1708$), there is no significant movement or

macroscopic motion in the fluid. However, beyond the critical Ra value, motion begins in the fluid, where the denser portions of the fluid are pulled down by gravity.

Similarly, the phenomenon of heat flow can be described using the Nusselt number (Nu), which represents the ratio between the total heat transferred by the fluid and the one transferred by conduction only. Mathematically, it can be expressed as

$$Nu = \frac{Q_c L}{\lambda} \quad (8.2)$$

where Q_c is the heat transfer coefficient, L a characteristic length of the flow and λ the thermal conductivity. In the case of a fluid layer with an aspect ratio $r = \Phi/h$ that tends towards infinity, where Φ represents the diameter of the fluid layer, heat transfer takes place through conduction (with a corresponding Nusselt number of 1) when the Rayleigh number is below a certain critical value, $Ra_c = 1708$. However, when the Rayleigh number exceeds this threshold, heat transfer occurs through convection (with a Nusselt number greater than 1), as depicted in Figure 8.1.

As mentioned in section 2.1.3, the non-equilibrium mass flow i of the fluid is generated by the Ludwig-Soret effect due to the imposed temperature gradient. The equation governing this effect is given by

$$i = -\rho D [\nabla c - c(1-c)S_T \nabla T] \quad (8.3)$$

where ρ denotes the sample density, D represents the diffusion coefficient, c is the weight fraction concentration and S_T denotes the Soret coefficient. Consequently, the density profile within the sample is influenced both by the vertical profiles of temperature and fluid concentration.

The Soret effect is often studied in an experimental setting where a thin layer of fluid is confined between two plates at different temperatures, creating a thermal gradient cell. This experimental setup can give rise to a variety of phenomena depending on the conditions.

When the temperature at the bottom boundary of the cell (T_{below}) is smaller than the one at the top (T_{above}), two scenarios can occur when the particle density is

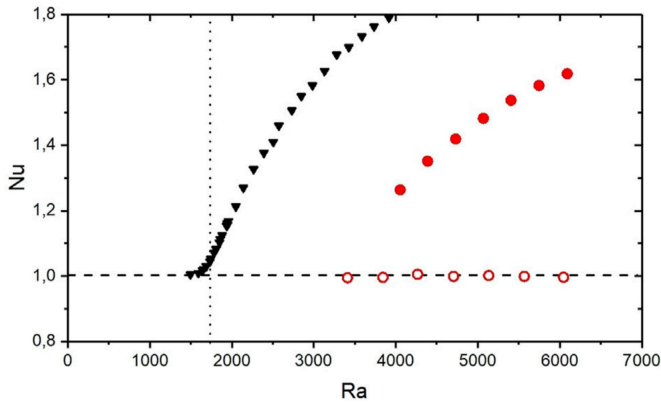


FIGURE 8.1: The figure shows a stability diagram depicting the relationship between the Nusselt number and Rayleigh number for a single-component fluid, liquid helium (represented by triangles), and LUDOXTM colloidal silica nanoparticles in water at a concentration of 4.0% w/w (represented by circles). The colloidal sample exhibits bistability, indicated by the presence of a stable convective branch (represented by full circles) and a stable conductive branch (represented by open circles). The dashed horizontal line denotes the purely conductive regime ($Nu = 1$), while the vertical dotted line corresponds to the Rayleigh-Bénard convection threshold of $Ra_c = 1708$ for a single-component fluid. Moreover, the range of Rayleigh numbers $2000 < Ra < 4000$ is characterized by the observation of transient rotating structures.

higher than the one of the supporting fluid. If the dispersed particles is thermophobic ($S_T > 0$), there is no macroscopic motion or net microscopic mass transport, and the system is stable. In this case, gravity and the thermophobic behavior of the colloid work together to stabilize the system. On the other hand, if the dispersed phase is thermophilic ($S_T < 0$), it tends to move towards the hotter plate and this give rise to an unstable configuration where gravity pulls the colloid down. This condition can cause solutal convection, a type of convective motion driven by the thermophilic nature of the colloid.

When T_{below} is greater than T_{above} , the phenomenology becomes more complex. If the Rayleigh number (Ra) is greater than the critical Rayleigh number (Ra_c), the system is above the threshold for Rayleigh-Bénard convection. In this case, the presence of the colloid affects the value of the threshold. If the dispersed

phase has a negative S_T , it has a stabilizing effect on the system as the colloid is pulled downwards towards the hotter plate. Conversely, if S_T is positive, the onset of convection is favored. If Ra is less than Ra_c , the system is below the convective threshold. In this scenario, the sign of S_T determines the role of the colloid in making the system more or less stable. In the case of positive S_T , solutal convective motions can arise due to the unstable density profile of colloidal particles.

Of particular interest is the case of a suspension of thermophilic particles heated from below because it presents a unique scenario in which the stabilising flow of nanoparticles induced by thermophoresis competes with the destabilising flow caused by thermal convection. The separation ratio Ψ , defined by

$$\Psi = \frac{\nabla\rho_s}{\nabla\rho_T} \quad (8.4)$$

expresses the relative contribution of solutal and thermal expansion in determining density differences $\nabla\rho_s$ and $\nabla\rho_T$, respectively. When Ψ is in the range of $-1 < \Psi < 0$, competition between these two factors causes traveling waves, localized pulses of convection, localized states, and convectons [86, 59, 53, 52]. However, when $\Psi < -1$, the stabilizing effect from the Soret flux dominates, and heat transfer occurs in the conductive regime regardless of the temperature gradient. Nevertheless, experiments on strongly thermophilic nanoparticles with $\Psi = -3.5$ and $\Psi = -7.5$ have demonstrated that initial conditions significantly impact the behavior of the system. When the temperature gradient is imposed gradually, nanoparticles migrate to the bottom, stabilizing the fluid layer against Rayleigh-Bénard convection, resulting in heat transfer by conduction. Conversely, a rapid imposition of the temperature gradient in the presence of a uniform dispersion of particles leads to convective motions that keep the particles dispersed and cause convection to continue indefinitely if the Rayleigh number is large enough. Theoretical investigations into the stability of a strongly thermophilic colloidal suspension with a large negative separation ratio reveal a transient oscillatory instability caused by the competition between Rayleigh-Bénard convection and the stabilizing effect from the Soret effect.

In this kind of systems, it is crucial to take into account another phenomenon

that affects the system's stability: sedimentation. To describe it, we employ the concept of the *sedimentation length* l_g which represents the characteristic length scale over which the concentration of suspended particles varies due to gravity. It's defined by

$$l_g = \frac{k_B T}{\nabla \rho V g} \quad (8.5)$$

where $\nabla \rho$ is the density mismatch between the particle and the carrier fluid, V is the volume of the particle and k_B the Boltzmann constant. Experimental conditions with weak sedimentation show that a decrease in l_g is associated with a decrease in the convection threshold and the frequency of neutral oscillations [74]. The interplay between sedimentation, thermophoresis with negative separation ratio, and convection has led to the discovery of a new traveling wave solution characterized by an anharmonic distribution of the vertical velocity across the sample layer [25]. Two-dimensional simulations mirroring experiments on a Hyflon MFA colloidal suspension with $\Psi = -7.5$ have shown that including the effect of gravitational sedimentation enables the quantitative estimation of the lifetime of the oscillatory flow as a function of Rayleigh number [24].

8.2 Convection: Experimental set up and methods

This section details the experimental apparatus employed to examine the convective patterns in the sample, which will also be utilized in future investigations of thermal and concentration NEFs within the same sample. Both NEFs and convective patterns are analyzed using the optical shadowgraph technique, although the difference in the experimental approaches lies in the subsequent analysis of the acquired measurements. The investigation of the various wave vectors, detailed in the previous section 2.2.2, of the scattered intensity is not necessary to study convective patterns. In addition to describing the optical setup utilized for image acquisition, this section delves into the specifics of the gradient cell and sample utilized, as well as the measurement procedure.

8.2.1 Experimental System

The key element of the experimental apparatus is a thermal gradient cell that comprises a layer of fluid confined between two sapphire plates, through which a thermal gradient can be imposed. The cell is heated using two ring-shaped Thermo Electric Devices (TED) that are thermally connected to the sapphire plates. The TED elements are in contact with an aluminum thermal reservoir, consisting of two annular chambers that house a steady flow of water at a constant temperature. The purpose of this reservoir is to remove excess heat from the system. The cell is mounted horizontally on an optical bench and illuminated with a superluminescent diode with a central wavelength of 670 nm. The limited temporal coherence of the light source prevents interference caused by multiple reflections of the beam on the cell windows. The sensing device employed is a monochrome CCD camera (JAI CV-M300) with a resolution of 576x768 pixels and a depth of 8 bits, operating at a frame rate of 10 images per second. An achromatic doublet with a focal length of 30 cm is placed between the sample cell and the camera to image a plane at a distance of $z = -90.6 \pm 0.5$ cm from the sample in a shadowgraph configuration that enables visualization of the self-organized structures generated by the convective motions. The camera is remotely controlled by a computer through a National Instrument PCI-1407 frame-grabber

8.2.2 The sample

The experiment utilizes a colloidal suspension composed of distilled water and *LUDOXTM* TMA, a commercial colloid consisting of silica nanoparticles with an average diameter of 22 nm. The sample is used at concentrations of 4.0% w/w, and its thermophysical properties are provided in table 8.1. This particular sample has been selected as a model system to investigate thermophoresis at the mesoscopic scale in the absence of gravity, within the framework of the European Space Agency's Giant Fluctuations and TechNES space projects [1, 85]. The projects involve conducting experiments on the International Space Station to explore the non-equilibrium fluctuations resulting from the thermophoretic

TABLE 8.1: *LUDOXTM TMA thermo-physical properties [14].*

Diameter (nm)	D	D_{Th}	α
22	$2.2 \cdot 10^{-7} \text{cm}^2/\text{s}$	$1.52 \cdot 10^{-3} \text{cm}^2/\text{s}$	$2.97 \cdot 10^{-4} \text{K}^{-1}$
	ν	β	S_T
	$8.18 \cdot 10^{-3} \text{cm}^2/\text{s}$	0.57	$-4.7 \cdot 10^{-2} \text{K}^{-1}$

process. Initial studies performed under isothermal conditions on Earth demonstrated the existence of an unusual relaxation dynamic of non-equilibrium concentration fluctuations, characterized by anomalous diffusion at large wave vectors [41]. For this reason, it is crucial to achieve a complete understanding of the stability of this colloidal suspension in the presence of gravity.

8.3 Convection: Results

In this study, our focus is on investigating the phenomenon of transient Rayleigh-Bénard convection in a suspension of highly thermophilic nanoparticles with a large negative separation ratio $\Psi = -3.5$. The suspension is heated from below, under experimental conditions similar to those used in theoretical studies [24, 26]. Our findings reveal that after the sudden imposition of a thermal gradient to a suspension of uniformly distributed nanoparticles, transient localized states appear within the range of Rayleigh numbers $2200 < Ra < 3000$. These states rotate rapidly around their axis and gradually decrease in size until they disappear, and the system returns to a purely conductive state. We provide a quantitative analysis of the wave number and angular velocity of these localized states and compare our results with previous theoretical models and simulations. The study of spatially localized states is of great interest in the field of pattern formation, as they appear in a wide range of physical and biological systems

[47]. When these states are stationary and convective in nature, they are known as "convectons," and there is a growing body of research studying them from theoretical, computational, and experimental perspectives [2, 3, 57].

8.3.1 Pattern formation

The presence of thermophilic colloidal particles has a significant impact on heat conduction in fluids. Even a small amount of these particles can stabilize the suspension when heated from below, resulting in heat transfer through either a conductive or convective regime, depending on the initial condition (Fig. 8.1) [33, 5]. The conductive regime can be accessed by gradually imposing a temperature difference to the sample while heating from below, causing the thermophilic particles to accumulate at the bottom of the cell and stabilize the sample against Rayleigh-Bénard convection. On the other hand, the convective regime can be achieved by initially heating the sample from above to determine the accumulation of nanoparticles at the top of the cell, and then quickly reversing the temperature gradient by heating from below. This leads to the onset of Rayleigh-Bénard instability, preventing the accumulation of thermophilic particles at the bottom of the cell, due to the convective flow that keeps the particles mixed. Conversely, if the temperature gradient is slowly increased from below, thermophoresis triggers the rapid formation of a stable boundary layer at the bottom of the cell, resulting in the system ending up in the conductive regime.

The phenomenon of bistable heat transfer has been well established for strongly thermophilic nanoparticles [33, 5]. However, bistability is only observed for Rayleigh numbers Ra greater than 4000. Below this value of Rayleigh number and above the threshold for Rayleigh-Bénard convection, $Ra_c = 1708$, the system exhibits transient convective behavior when heated from below. Nonetheless, the stabilization determined by the particles ultimately dominates, and the system enters into a purely conductive regime.

To investigate the transient convective regime in the range of Rayleigh numbers of interest, we conducted experiments using the following procedure:

- The sample was heated from above for one hour, with a temperature difference of $\Delta T = 10.5$ K. This ensured that the strong thermophilic behavior

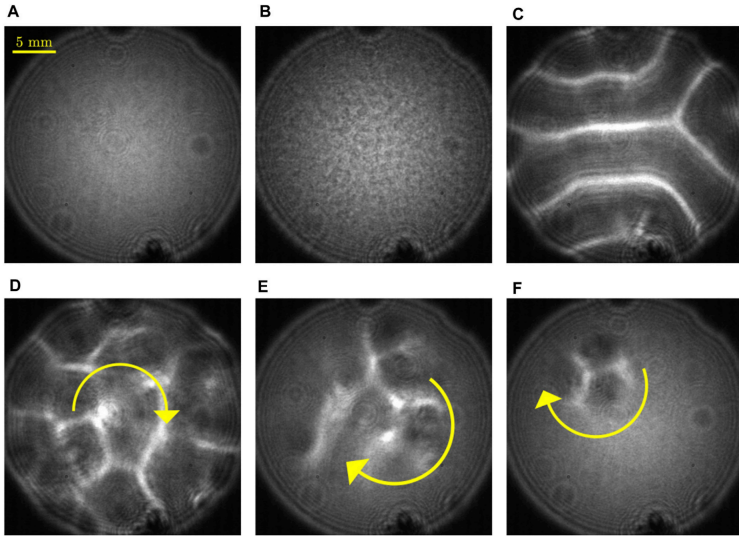


FIGURE 8.2: *The figure shows a sequence of images illustrating the evolution of convective instability in a 3.1 mm thick layer of LUDOXTM TMA 4% w/w. (A) At the beginning, the sample is heated from above with a temperature difference of 10.5 K, and no macroscopic motions are present. (B) After a time of the order of tens of minutes, solutal convection develops in the cell. (C) After one hour, the temperature difference is inverted and set to -4.13 K. In approximately three minutes, thermal convective rolls appear in the sample. (D) The rolls begin to rotate after a time that depends on the Rayleigh number. (E) They die out starting from the borders. (F) Finally, they gradually shrink in size until they disappear completely.*

of LUDOXTM TMA caused the colloidal particles to diffuse towards the upper plate, resulting in a solutal convective regime [19, 56, 39]. The time required to enter this regime was determined empirically and corresponds to the diffusive time $\tau_\delta = \delta^2/D$ needed for the formation of a thin and unstable boundary layer of thickness δ at the top of the cell. This time is influenced by the size of the nanoparticles through their diffusion coefficient D .

- The temperature gradient was abruptly reversed to a negative value. In our experiments, we used temperature differences of $\Delta T = -3.00$ K, -3.38

K, -3.75 K, and -4.13 K.

- Shadowgraph images of the sample were recorded with a frame rate of approximately 10 images per second.

Under the specified experimental conditions, heating the sample from above initiates solutal convection, leading to the destabilization of the suspension (as depicted in Fig. 8.2A). When the gradient is inverted, a convective instability emerges in the sample, even when it is below the threshold necessary for the development of stationary Rayleigh-Bénard convection in the nanofluid (as illustrated in Fig. 8.2). Initially, the convective patterns consist of the typical convective rolls that characterize Rayleigh-Bénard convection and span the entire area of the cell. Subsequently, these patterns start rotating around the vertical axis, either clockwise or anticlockwise, and eventually begin to die out from the borders of the cell, resulting in the formation of a single rotating localized pattern. The rotating pattern gradually shrinks in size until it vanishes completely, and the sample reaches a stationary conductive state. The entire phenomenon, from the inversion of the gradient, lasts between 1 and 3 hours, and this same phenomenon is observed for all temperature differences studied.

8.3.2 Pattern characteristic parameters

Through the analysis of sequences of images, we have extracted certain defining parameters of localized states as a function of Rayleigh number. Of particular interest are the wave vector k and angular velocity ω of the patterns, as well as the characteristic timescales t_{ap} required for the formation of the convective structure, t_{rot} needed for the onset of pattern rotation, and t_{ex} required for the patterns to dissipate. Our findings are presented in Figure 8.3, where we summarize the results.

The value of the characteristic wave vector k is consistent with the predicted value of 3.117 for Rayleigh-Bénard convection near the threshold [22]. The angular velocity of the patterns was determined by visually observing a large number of complete revolutions of the localized pattern, typically 10 – 20 revolutions. We determined the maximum number of revolutions to consider based on the need to preserve the structure of the rotating pattern, allowing us to track

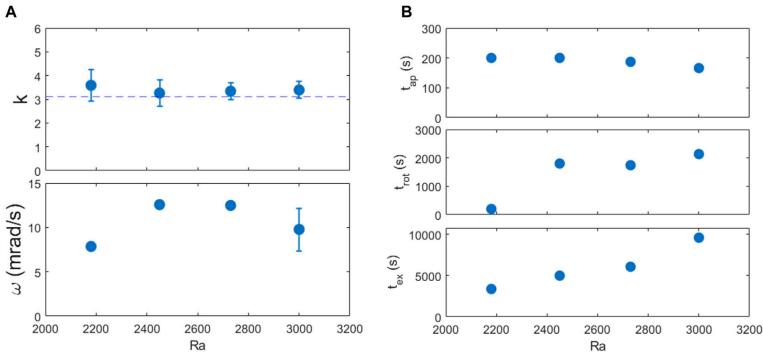


FIGURE 8.3: The figure displays two graphs depicting the relationship between Rayleigh number and two key variables of the patterns: the dimensionless wave number k (top) and angular velocity ω (bottom). The theoretical wave number $k_c = 3.117$ of Rayleigh-Bénard convection is represented by a dashed line close to the onset. Additionally, the plot illustrates the time required for the convective pattern to appear (t_{ap} , top), the beginning of the rotation of the pattern (t_{rot} , middle), and the extinction of the convective instability (t_{ex} , bottom) as a function of Rayleigh number. The time scale is measured from the point where the gradient is reversed ($t = 0$). These results are significant for understanding the behavior of Rayleigh-Bénard convection.

the motion of the spatial features of the patterns during rotation. This method proved to be more effective and less prone to errors than automatic processing of angular correlations.

The rotation of the patterns occurs very slowly, with a complete revolution taking between 500 – 800 seconds. The time tap required for the structures to appear is approximately 200 seconds, slightly decreasing as the Rayleigh number increases. The behavior of the time trot needed for the rotation to start is of significant interest, as it exhibits a factor 10 variation when the Rayleigh number is increased from 2180 to 3000. This range is of great significance as it reveals the occurrence of competition between Rayleigh-Bénard thermal convection and the stabilizing influence of colloidal particles. This competition results in the formation of traveling wave patterns, which become rotating patterns in a circular cell due to confinement from the lateral boundary. However, in the subcritical Rayleigh number regime explored in this study, Rayleigh-Bénard convection

prevails, and the stabilizing effect of colloid accumulation on the cell's bottom is hampered by the continuous remixing of particles. Under these conditions, sedimentation of particles is slowed, as are the appearance of traveling waves and the onset of rotation. The time required for convection to disappear also exhibits a significant dependence on the Rayleigh number and is in qualitative agreement with the results of simulations on suspensions of thermophilic nanoparticles with a large negative separation ratio heated from below [24].

Chapter 9

Conclusions

In these conclusions I will summarise the most important results, their implications for the search for non-equilibrium fluctuations and the next steps I plan to take with my research.

We show that non-equilibrium fluctuations in free diffusion under nonideal conditions, such as transient processes and large concentration differences, are characterized by a wide distribution of relaxation times determined by sample stratification. We propose a model based on a uniform distribution of relaxation times that allows us to describe the dynamics of non-equilibrium fluctuations during these processes. Comparison of the uniform distribution model with the Schulz model, commonly applied in dynamic light scattering to characterize the polydispersity of samples, confirms the better performance of the UD model in the presence of a wide range of relaxation times determined by strong stratification. For small concentration differences, in the presence of a moderate range of relaxation times, the effectiveness of the three models is comparable. Investigation of the influence of gravity on the dynamics of non-equilibrium fluctuations shows that the results obtained under all stratification conditions can be described by a universal power law governing the time evolution of the roll-off wave number below which the fluctuations are significantly influenced by gravity.

Furthermore, in the second part of the thesis, we observed the presence of transient and stationary traveling wave regimes in an aqueous solution of Ludox^{TMA}. This study was able to characterize the presence of transient and stationary traveling-wave regimes and to determine the threshold at which a transition from a transient to a stationary regime occurs at the Rayleigh number $Ra \sim 3400$. The study completed the bifurcation diagram of the Nusselt number as a function of

the Rayleigh number, which needed modifications determined by the presence of nanoparticles; finally, we characterized the lifetime diagram of traveling waves in the transient regime as a function of the Rayleigh number.

In particular, the most important result concerns the analysis of fluctuations occurring during the free diffusion of glycerol and water solutions in which varying concentration gradients are present. In particular, nine different initial concentrations were investigated (Fig. 9.1). In addition, we carried out measure-

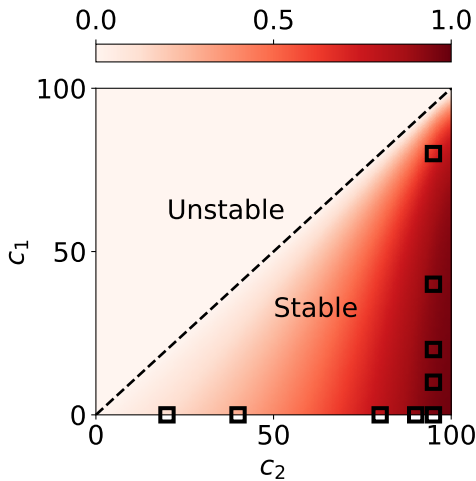


FIGURE 9.1: *Diagram of the concentration couples used in this work. The dashed line marks the boundary between the stable condition where a denser mixture of concentration c_2 is layered at the bottom of a less dense one of concentration c_1 , and the unstable condition where the denser mixture is at the top. The red shading indicates the predicted value of the stratification index SI . The stratification of the system increases in the horizontal direction towards the right and in the vertical direction towards the bottom.*

ments at various times in the evolution of the system to observe fluctuations in the concentration profile. The measurement conditions and timing are summarised in Table 6.1.

In order to establish the starting point for the experiment where two fluid phases

can be clearly separated by a well-defined interface, we utilised a flowing junction cell, as described in reference [29]. This cell was designed to hold a sample, with the interface between the two mixtures located precisely in the middle height of the sample.

Due to the strong stratification of the sample, the system is non-linear and requires an interpretative model to analyse the correlation properties of the non-equilibrium fluctuations. With regard to statics, it was evident from the computational predictions (Fig. 4.2) and the experimental data presented (Fig. 7.2c) that the integrated values of $S(q)$ for the entire thickness of the sample have a similar trend to those integrated on the central thin layers, which contribute more to the average. Therefore, the shape of the stratified static structure factor is not significantly influenced by the contributions of the different layers. A suitable model for the interpolation of the layered structure factor is given by equation 4.7:

$$\frac{S(q)}{S(0)} = \frac{1}{1 + \left(\frac{q}{q_{ro}}\right)^4} \quad (9.1)$$

This equation is identical to that of the ideal layer and allows us to estimate the effective roll-off wave number determined by the layering. A comparison of models interpolating the actual data also gives the same result, which therefore tells of a stratification-independent statics. In order to obtain an expression for the correlation function $g(q, \Delta t)$ for highly stratified systems, we averaged the contributions of the different layers, similarly to what was done for the Static Stratified Structure Factor. In the dynamic case, the stratification of the sample results in a dispersion of the relaxation rate of the non-equilibrium fluctuations at a fixed wave number q , due to the concentration dependence of the diffusion coefficient (Eqn. 4.2) and the roll-off wave number (Eqn. 2.38). After proposing the UD model, which is characterised by a uniform probability density $G(\gamma)$ of the decay rates, it was possible to obtain an analytical expression for the stratified correlation function:

$$g(q, \Delta t) = \exp(-\Gamma \Delta t) \cdot \frac{\sinh(\sigma \Delta t)}{\sigma \Delta t} \quad (9.2)$$

where Γ and σ are the mean value and the width, respectively, of the relaxation rates distribution.

The form of equation 9.2 is particularly interesting because the correlation function is expressed as a single exponential relaxation multiplied by a hyperbolic sine cardinal function that characterises the presence of a dispersion of the relaxation times. This means that for $\sigma \sim 0$, we obtain the ideal single exponential relaxation for a thin layer, in which the non-equilibrium fluctuations relax with a single characteristic time.

In order to evaluate the effectiveness of the proposed UD model in characterizing the dynamics of non-equilibrium fluctuations for stratified samples, we compared it to two alternative models. The first model is the thin-layer model, which assumes no dispersion and a single exponential relaxation of the correlation function. The second model incorporates dispersion of relaxation rates, as defined by the Schulz distribution, which gives rise to an analytic expression for the correlation function expressed in equation 5.10. Our analysis and validations included both simulations (Fig. 5.2) and experimental results (Fig. 7.2), which consistently demonstrated that the proposed UD model outperforms the other models in accurately characterizing the dynamics of non-equilibrium fluctuations for stratified samples. However, it was also experimentally verified that, in the presence of a moderate range of relaxation times and small differences in concentration, the three models perform similarly.

The characterization of the mean value and dispersion of relaxation rates with the UD model has opened up a promising area for further research, focusing on their trends as q changes. Theoretical calculations were carried out to determine these trends (as demonstrated in Equations 4.19 and 4.20), and their computational verification was subsequently conducted (as shown in Figure 4.3).

These trends are dependent on thermodynamic parameters that influence the dynamics of fluctuations, specifically on the dispersion and the mean value of the diffusion coefficient D (Eqns. 4.15 and 4.17) and roll-off wave vector q_{ro} (Eqns. 4.16 and 4.18) within the sample due to stratification.

Utilizing this information, we were able to characterize the mean value and width of the distribution of D , (D_Γ and D_σ , respectively), and the roll-off wave vector (q_Γ and q_σ , respectively).

Finally, the experimental data were compared with the theoretical values calculated using the diffusion coefficients obtained by empirical modelling from equation 4.2. It was observed that the average diffusion coefficient, D_T , decreases as the average concentration increases, consistent with the theoretical prediction (dashed line). However, the experimental values were systematically larger than the theoretical ones. The dispersion trend of the diffusion coefficient, D_σ , also agrees with the theoretical prediction, showing a peak at the maximum concentration difference ($c_1 = 0$, $c_2 = 0.95$). Although the experimental data are noisy and substantially different from the predicted values, this peak was nevertheless observed. These differences are also evident when comparing the stratification index SI predicted at each mean concentration with the experimental value.

On the other hand, concerning the impact of gravity on the dynamics of non-equilibrium fluctuations (i.e. q_T and q_σ), the results indicate that a universal power law can describe the temporal evolution of the roll-off wave number, which is the point below which the fluctuations are significantly affected by gravity, under all stratification conditions.

A potential application of the approach proposed in this study is the investigation of non-equilibrium fluctuations occurring during a free diffusion process in a binary liquid mixture near a consolute critical point of a second order phase transition. In this scenario, the diffusion coefficient of the mixture strongly depends on its concentration [40]. This approach could also be used to study other types of fluctuations occurring in stratified media, such as temperature fluctuations resulting from a temperature gradient. Such fluctuations could be influenced by large temperature gradients that have an impact on thermodynamic coefficients, such as the thermal diffusion coefficient and viscosity. This can lead to a dispersion of the relaxation times of non-equilibrium temperature fluctuations, similar to the phenomenon discussed in this article. This work was recently published in the scientific journal *The Journal of Chemical Physics* [15].

Moreover, the concluding part of this thesis focuses on exploring the stability diagram of an aqueous suspension of Ludox^{TMA} under the influence of high temperature gradients. This serves as an initial step in examining the Non-Equilibrium Fluctuations (NEFs) in colloidal suspensions in the presence of thermal gradients. The study is conducted on a suspension of highly thermophilic

nanoparticles, which are heated at the bottom and possess a negative separation ratio $\Psi = -3.5$. The complex stability diagram observed in this system arises from the interplay between the stabilizing flow of nanoparticles caused by thermophoresis and the destabilizing flow induced by thermal convection. We delved into the Rayleigh-Bénard convection and observed the emergence of transient states localized in the range of Rayleigh numbers $2200 < Ra < 3000$. These states exhibit rapid rotation around their axis and gradual decrease in size until the system reverts to a purely conductive state (Fig. 8.2). The discussion centers around the explanation of how these states emerge as a result of traveling waves that result from the competition between Rayleigh-Bénard convection and solute stabilization of the sample. The findings were published in [14].

Bibliography

- [1] P. Baaske et al. “The NEUF-DIX Space Project-Non-Equilibrium Fluctuations during Diffusion in complex Liquids”. In: *Eur. Phys. J. E* 39 (2016).
- [2] O. Batiste and E. Knobloch. “Simulations of Localized States of Stationary Convection in 3He-4He Mixtures”. In: *Phys. Rev. E* 95.2 (2005), p. 244501.
- [3] O. Batiste and E. Knobloch. “Simulations of Oscillatory Convection in 3He-4He Mixtures in Moderate Aspect Ratio Containers”. In: *Phys. Fluids* 17.6 (2005), p. 064102.
- [4] O. Batiste et al. “Spatially Localized Binary-Fluid Convection”. In: *Journal of Fluid Mechanics* 560 (2006), pp. 149–158. DOI: [10.1017/s0022112006000000](https://doi.org/10.1017/s0022112006000000)
- [5] M. Bernardin, F. Comitani, and A. Vailati. “Tunable Heat Transfer with Smart Nanofluids”. In: *Phys. Rev. E* 85.6 (2012), p. 066321.
- [6] N. N. Bogoliubov. “Problems of a Dynamical Theory in Statistical Physics”. In: *Studies in Statistical Mechanics I, Part A*. Ed. by J. de Boer and G. E. Uhlenbeck. Amsterdam: North-Holland, 1962, pp. 5–118.
- [7] J. P. Boon and S. Yip. *Molecular Hydrodynamics*. New York: Dover, 1990.
- [8] M. Born and E. Wolf. *Principles of Optics, 60th Anniversary Edition*. 2019.
- [9] A. Bouchaudy, C. Loussert, and J.-B. Salmon. “Steady microfluidic measurements of mutual diffusion coefficients of liquid binary mixtures”. In: *AIChE J.* 64 (2018), pp. 358–366.

- [10] D. Brogioli, F. Croccolo, and A. Vailati. “Correlations and scaling properties of non-equilibrium fluctuations in liquid mixtures”. In: *Phys. Rev. E* 94 (2016), p. 022142.
- [11] D. Brogioli and A. Vailati. “Diffusive mass transfer by nonequilibrium fluctuations: Fick’s law revisited”. In: *Phys. Rev. E* 63.1 I (2001), pp. 0121051–0121054.
- [12] D. Brogioli, A. Vailati, and M. Giglio. “Universal behavior of nonequilibrium fluctuations in free diffusion processes”. In: *Phys. Rev. E* 61.1 (2000), R1–R4.
- [13] M. Carpineti et al. “Kinetics of growth of non-equilibrium fluctuations during thermodiffusion in a polymer solution”. In: *Eur. Phys. J. E* 42.2 (2019), p. 25.
- [14] M. Carpineti et al. “Transient Localized Rotating Structures in a Suspension of Highly Thermophilic Nanoparticles”. In: *Front. Phys.* 10 (2022), p. 654.
- [15] S. Castellini et al. “Dynamics of non-equilibrium concentration fluctuations during free-diffusion in highly stratified solutions of glycerol and water”. In: *J. Chem. Phys.* 158 (2023), p. 244201.
- [16] S. Castellini et al. “Inclined convection in a layer of liquid water with poorly conducting boundaries”. In: *Phys. Rev. Res.* 2 (3 2020), p. 033481.
- [17] R. Cerbino and V. Trappe. “Differential dynamic microscopy: Probing wave vector dependent dynamics with a microscope”. In: *Phys. Rev. Lett.* 100 (2008), p. 188102.
- [18] R. Cerbino and A. Vailati. “Near-field scattering techniques: Novel instrumentation and results from time and spatially resolved investigations of soft matter systems”. In: *Curr. Opin. Colloid Interface Sci.* 14.5 (2009), pp. 416–427.
- [19] R. Cerbino, A. Vailati, and M. Giglio. “Soret driven convection in a colloidal solution heated from above at very large solutal Rayleigh number”. In: *Phys. Rev. E* 66.5 (2002), p. 055301.

- [20] R. Cerbino et al. “Dynamic scaling for the growth of non-equilibrium fluctuations during thermophoretic diffusion in microgravity”. In: *Sci. Rep.* 5 (2015), p. 14486.
- [21] G. Cerchiari et al. “Note: quasi-real-time analysis of dynamic near field scattering data using a graphics processing unit”. In: *Rev. Sci. Instrum.* 83 (2012), p. 036104.
- [22] S. Chandrasekhar. *Hydrodynamic and Hydromagnetic Stability*. 1961.
- [23] C. Chatfield. *The Analysis of Time Series: Theory and Practice*. Springer, 1975.
- [24] I. Cherepanov and B. Smorodin. “Traveling Waves of a Colloidal Suspension in a Closed Cell”. In: *Eur. Phys. J. E* 45.51 (2022), p. 51.
- [25] I. N. Cherepanov and B. L. Smorodin. “Convection of Strong Stratified Colloidal Suspension”. In: *Microgravity Sci. Technol.* 31.4 (2019), pp. 517–525.
- [26] I. N. Cherepanov and B. L. Smorodin. “Influence of Sedimentation Length on the Convective Stability of a Colloidal Suspension”. In: *J. Exp. Theor. Phys.* 125.6 (2017), pp. 1199–1207.
- [27] F. Croccolo, J. M. Ortiz de Zárate, and J. V. Sengers. “Non-local fluctuation phenomena in liquids”. In: *Eur. Phys. J. E* 39.125 (2016).
- [28] F. Croccolo, D. Brogioli, and A. Vailati. “Cylindrical flowing-junction cell for the investigation of fluctuations and pattern-formation in miscible fluids”. In: *Rev. Sci. Instrum.* 90 (2019), p. 085109.
- [29] F. Croccolo, D. Brogioli, and A. Vailati. “Cylindrical flowing-junction cell for the investigation of fluctuations and pattern formation in miscible fluids.” In: *Rev. Sci. Instrum.* 90 (2019), p. 085109.
- [30] F. Croccolo et al. “Nondiffusive decay of gradient-driven fluctuations in a free-diffusion process”. In: *Phys. Rev. E* 76.4 (2007), p. 041112.
- [31] F. Croccolo et al. “Shadowgraph analysis of non-equilibrium fluctuations for measuring transport properties in microgravity in the gradflex experiment”. In: *Microgravity Sci. Technol.* 28.5 (2016), p. 467.

- [32] G. D'Errico et al. "Diffusion Coefficients for the Binary System Glycerol + Water at 25 °C. A Velocity Correlation Study". In: *J. Chem. Eng. Data* 49.6 (2004), pp. 1665–1670.
- [33] G. Donzelli, R. Cerbino, and A. Vailati. "Bistable Heat Transfer in a Nanofluid". In: *Phys. Rev. Lett.* 102.10 (2009), p. 104503.
- [34] G. Eyink and A. Jafari. "High Schmidt-number turbulent advection and giant concentration fluctuations". In: *Phys. Rev. Res.* 4.2 (2022), p. 023246.
- [35] G. Eyink and A. Jafari. "The Kraichnan model and non-equilibrium statistical physics of diffusive mixing". In: *Ann. Henri Poincaré* (2022), pp. 1–37.
- [36] R. F. Fox and G. E. Uhlenbeck. "Contributions to non-equilibrium thermodynamics. I. Theory of hydrodynamical fluctuations". In: *Phys. Fluids* 13 (1970), p. 1893.
- [37] B. J. Frisken. "Revisiting the method of cumulants for the analysis of dynamic light-scattering data". In: *Applied Optics* 40 (2001), p. 4087.
- [38] L. García-Fernández et al. "Coupled non-equilibrium fluctuations in a polymeric ternary mixture". In: *Eur. Phys. J. E* 42 (2019), p. 124.
- [39] F. Giavazzi and A. Vailati. "Scaling of the spatial power spectrum of excitations at the onset of solutal convection in a nanofluid far from equilibrium". In: *Phys. Rev. E* 80.1 (2009), p. 015303.
- [40] F. Giavazzi et al. "Equilibrium and non-equilibrium concentration fluctuations in a critical binary mixture". In: *Eur. Phys. J. E* 39 (2016), p. 103.
- [41] F. Giavazzi et al. "Structure and dynamics of concentration fluctuations in a non-equilibrium dense colloidal suspension." In: *Soft Matter* 12 (2016), pp. 6588–6600.
- [42] M. Giglio, M. Carpineti, and A. Vailati. "Space Intensity Correlations in the Near Field of the Scattered Light: A Direct Measurement of the Density Correlation Function $g(r)$ ". In: *Phys. Rev. Lett.* 85.7 (2000), p. 1416.
- [43] R. Helmig, A. Mielke, and B. I. Wohlmuth, eds. *Multifield Problems in Solid and Fluid Mechanics*. Vol. 28. Lecture Notes in Applied and Computational Mechanics. Berlin: Springer-Verlag, 2006.

- [44] K. Kawasaki. “Kinetic equations and time correlation functions of critical fluctuations”. In: *Ann. Phys.* 61.1 (1970), p. 1.
- [45] T. R. Kirkpatrick, J. M. Ortiz de Zàrate, and J. V. Sengers. “Giant Casimir effect in fluids in Nonequilibrium Steady States”. In: *Phys. Rev. Lett.* 110.23 (2013), p. 235902.
- [46] T.R. Kirkpatrick, E.G.D. Cohen, and J.R. Dorfman. “Fluctuations in a nonequilibrium steady state; Basic equations”. In: *Phys. Rev. A* 26.2 (1982), p. 950.
- [47] E. Knobloch. “Spatially Localized Structures in Dissipative Systems: Open Problems”. In: *Nonlinearity* 21.4 (2008), T45–T60.
- [48] D. E. Koppel. “Analysis of macromolecular polydispersity in intensity correlation spectroscopy: the method of cumulants”. In: *J. Chem. Phys.* 57.10 (1972), pp. 4814–4820.
- [49] R. Kubo, M. Toda, and H. Hashitsume. *Statistical Physics II: Nonequilibrium Statistical Mechanics*. 1991.
- [50] L. D. Landau and E. M. Lifshitz. *Fluid Mechanics*. 1987.
- [51] B. M. Law and J. C. Nieuwoudt. “Noncritical liquid mixtures far from equilibrium: The Rayleigh line”. In: *Phys. Rev. A* 40.7 (1989), pp. 3880–3886.
- [52] K. Lerman, D. S. Cannell, and G. Ahlers. “Analysis of transients for binary mixture convection in cylindrical geometry”. In: *Phys. Rev. E* 59.3 (1999), pp. 2975–2985.
- [53] K. Lerman et al. “Transient Localized States in 2d Binary Liquid Convection”. In: *Phys. Rev. Lett.* 70.23 (1993), pp. 3572–3575.
- [54] P. J. Lu et al. “Characterizing concentrated, multiply scattering, and actively driven fluorescent systems with confocal differential dynamic microscopy”. In: *Phys. Rev. Lett.* 108 (2012), p. 218103.
- [55] A.G. Mailer, P.S. Clegg, and P.N. Pusey. “Particle sizing by dynamic light scattering: non-linear cumulant analysis”. In: *Journal of Physics: Condensed Matter* 27 (2015), p. 145102.

- [56] S. Mazzoni et al. “Mutual Voronoi tessellation in spoke pattern convection”. In: *Phys. Rev. Lett.* 100.18 (2008), p. 188104.
- [57] I. Mercader, A. Alonso, and O. Batiste. “Spatiotemporal dynamics near the onset of convection for binary mixtures in cylindrical containers”. In: *Phys. Rev. E* 77.3 (2008), p. 036313.
- [58] I. D. Morrison and S. Ross. *Colloidal Dispersions: Suspensions, Emulsions, and Foams*. New York: Wiley Interscience, 2002.
- [59] J.J. Niemela, G. Ahlers, and D.S. Cannell. “Localized Traveling-Wave States in Binary-Fluid Convection”. In: *Phys. Rev. Lett.* 64.12 (1990), pp. 1365–1368.
- [60] Y. Nishijima and G. Oster. “Diffusion in Glycerol-Water Mixture”. In: *Bull. Chem. Soc. Jpn.* 33.12 (1960), pp. 1649–1651.
- [61] M. Norouziadeh et al. “The modern structurator: increased performance for calculating the structure function”. In: *Eur. Phys. J. E* 44 (2021), p. 146.
- [62] R. Pecora. *Dynamic Light Scattering: Applications of Photon Correlation Spectroscopy*. Springer New York, 1985, pp. XIV, 420.
- [63] P.N. Pusey et al. “Intensity Fluctuation Spectroscopy of Laser Light Scattered by Solutions of Spherical Viruses”. In: *Biochemistry* 13 (1974), pp. 952–960.
- [64] J. Rauch and W. Köhler. “Diffusion and thermal diffusion of semidilute to concentrated solutions of polystyrene in toluene in the vicinity of the glass transition”. In: *Phys. Rev. Lett.* 88.18 (2002), p. 185901.
- [65] M. H. Rausch, A. Heller, and A. P. Fröba. “Binary Diffusion Coefficients of Glycol-Water Mixtures for Temperatures from 323 to 448 K by Dynamic Light Scattering”. In: *J. Chem. Eng. Data* 62.12 (2017), pp. 4364–4370.
- [66] D. Ronis and I. Procaccia. “Nonlinear resonant coupling between shear and heat fluctuations in fluids far from equilibrium”. In: *Phys. Rev. A* 26.4 (1982), p. 1812.

- [67] I. Pala Rosas et al. “Catalytic Dehydration of Glycerol to Acrolein over a Catalyst of Pd/LaY Zeolite and Comparison with the Chemical Equilibrium”. In: *Catalysts* 7 (2017), p. 73.
- [68] E.O. Schulz-DuBois and I. Rehberg. “Structure function in lieu of correlation function”. In: *Appl. Phys.* 24.4 (1981), pp. 323–329.
- [69] P. N. Segre, R. Schmitz, and J. V. Sengers. “Fluctuations in inhomogeneous and nonequilibrium fluids under the influence of gravity”. In: *Physica A* 195 (1993), p. 31.
- [70] P. N. Segre and J. V. Sengers. “Nonequilibrium fluctuations in liquid mixtures under the influence of gravity”. In: *Physica A* 198 (1993), p. 46.
- [71] P.N. Segrè, R.W. Gammon, and J.V. Sengers. “Light-scattering measurements of nonequilibrium fluctuations in a liquid mixture”. In: *Phys. Rev. E* 47.2 (1993), pp. 1026–1034.
- [72] J.V. Sengers and P.H. Keyes. “Scaling of the Thermal Conductivity near the Gas-Liquid Critical Point”. In: *Phys. Rev. Lett.* 26.2 (1971), p. 70.
- [73] G. S. Settles. *Schlieren and Shadowgraph Techniques: Visualizing Phenomena in Transparent Media*. 1st. Experimental Fluid Mechanics. Berlin/Heidelberg: Springer-Verlag, 2001. DOI: [10.1007/978-3-540-40018-1](https://doi.org/10.1007/978-3-540-40018-1).
- [74] M. I. Shliomis and B. L. Smorodin. “Onset of convection in colloids stratified by gravity”. In: *Phys. Rev. E* 71.3 (2005), p. 036312.
- [75] I. Srivastava et al. “Staggered scheme for the compressible fluctuating hydrodynamics of multispecies fluid mixtures”. In: *Phys. Rev. E* 107.1 (2023), p. 015305.
- [76] C.J. Takacs et al. “Thermal fluctuations in a layer of liquid CS₂ subjected to temperature gradients with and without the influence of gravity”. In: *Phys. Rev. Lett.* 106.24 (2011), p. 244502.
- [77] G. Ternström et al. “Mutual Diffusion Coefficients of Water + Ethylene Glycol and Water + Glycerol Mixtures”. In: *J. Chem. Eng. Data* 41.5 (1996), pp. 876–879.
- [78] W. J. Thomas and E. McK. Nichol. “The Application of the Wavefront Shearing Optical Interferometer to Diffusion Measurements”. In: *Appl. Opt.* 4.7 (1965), pp. 823–829.

- [79] A.M.S. Tremblay. “Theories of fluctuations in nonequilibrium systems”. In: *Recent Developments in Nonequilibrium Thermodynamics*. Ed. by J. Casas-Vazquez, D. Jou, and G. Lebon. Vol. 199. Lecture Notes in Physics. Berlin: Springer, 1984, pp. 267–317.
- [80] F. Balboa Usabiaga et al. “Multiscale modeling of complex fluids: a comparative review”. In: *Multiscale Model. Simul.* 10.4 (2012), pp. 1369–1413.
- [81] A. Vailati and M. Giglio. “Giant fluctuations in a free diffusion process”. In: *Nature* 390 (1997), p. 262.
- [82] A. Vailati and M. Giglio. “Nonequilibrium fluctuations in time-dependent diffusion processes”. In: *Phys. Rev. E* 58.4 (1998), pp. 4360–4371.
- [83] A. Vailati and M. Giglio. “q divergence of nonequilibrium fluctuations and its gravity-induced frustration in a temperature stressed liquid mixture”. In: *Phys. Rev. Lett.* 77.8 (1996), pp. 1484–1487.
- [84] A. Vailati et al. “Fractal fronts of diffusion in microgravity.” In: *Nat. Commun.* 2 (2011), p. 290.
- [85] A. Vailati et al. “Giant Fluctuations Induced by thermal Diffusion in Complex Liquids”. In: *Microgravity Sci. Technol.* 32 (2020), pp. 873–887.
- [86] R. Walden et al. “Traveling Waves and Chaos in Convection in Binary Fluid Mixtures”. In: *Phys. Rev. Lett.* 55.5 (1985), pp. 496–499.
- [87] M. Wu, G. Ahlers, and D. S. Cannell. “Thermally Induced Fluctuations below the Onset of Rayleigh-Bénard Convection”. In: *Phys. Rev. Lett.* 75.9 (1995), pp. 1743–1746.
- [88] D. Zapf, J. Kantelhardt, and W. Köhler. “Nonlinearities in shadowgraphy experiments on non-equilibrium fluctuations in polymer solutions”. In: *Eur. Phys. J. E* 45.6 (2022), p. 77.
- [89] D. Zapf, J. Kantelhardt, and W. Köhler. “Nonlinearities in shadowgraphy experiments on non-equilibrium fluctuations in polymer solutions”. In: *Eur. Phys. J. E* 45 (2022), p. 40.
- [90] J.M.O. de Zárata and J.V. Sengers. *Hydrodynamic Fluctuations in Fluids and Fluid Mixtures*. 2006.

Chapter 10





Publications

This chapter presents the scientific articles that I have produced over the past three years, which form an integral part of my doctoral dissertation. The research presented in these articles has been conducted with the aim of exploring the fundamental mechanisms underlying the transport phenomena in different systems. Specifically, this research delves into the dynamics of inclined convection in a layer of liquid water with poorly conducting boundaries, the emergence of transient localized rotating structures in a suspension of highly thermophilic nanoparticles, and the dynamics of non-equilibrium concentration fluctuations during free-diffusion in highly-stratified solutions of glycerol and water.

Each of these articles is a significant contribution to the field of transport phenomena, and together they demonstrate the breadth and depth of my research interests. The first paper [16], not discussed in this thesis, investigates the dynamics of inclined convection in a layer of liquid water with poorly conducting boundaries, which is a problem of fundamental importance in geophysical and industrial processes. The second paper [14], discussed briefly in the chapter 8, explores the emergence of transient localized rotating structures in a suspension of highly thermophilic nanoparticles, which is a unique phenomenon with potential applications in microfluidics, colloidal science, and biophysics. The third article, although not yet published, investigates the dynamics of non-equilibrium concentration fluctuations during free-diffusion in highly-stratified solutions of glycerol and water, which is a problem of relevance to both fundamental science and practical applications. The entire thesis has been focused on this article, delving into its aspects.

Overall, this collection of articles highlights the importance of understanding the underlying mechanisms of transport phenomena in various systems and provides new insights into the behavior of complex fluids. The results presented in these articles not only expand our knowledge of transport phenomena but also have the potential to inform the design of new materials, devices, and processes.

Inclined convection in a layer of liquid water with poorly conducting boundaries

Stefano Castellini ¹, Marina Carpineti ¹, Fabrizio Crococo ² and Alberto Vailati ^{1,*}

¹Dipartimento di Fisica A. Pontremoli, Università degli Studi di Milano, I-20133 Milano, Italy

²Université de Pau et des Pays de l'Adour, E2S UPPA, CNRS, TOTAL, LFCR UMR5150, Anglet, France



(Received 19 December 2019; accepted 10 September 2020; published 24 September 2020)

We investigate pattern formation in an inclined layer of liquid water with poorly conducting boundaries. We show that above the threshold for convection the presence of an inclination larger than 14 mrad determines a transition from a square pattern to longitudinal rolls, a behavior remarkably different than the one reported in the presence of inclined conducting boundaries, where transitions between convective planforms occur at inclination angles of the order of several degrees. The longitudinal rolls are characterized by a dimensionless wave vector $k \approx 1.8$, significantly smaller than $k \approx 3.117$ reported for conducting boundaries at large Prandtl number. The transition can be triggered by changing dynamically the inclination of the layer of fluid, and does not occur symmetrically in the two directions. By starting in the horizontal configuration, it develops slowly through the demolition of the square structure to form longitudinal rolls, while it develops rapidly in the other direction, through the formation of a cross-roll structure perpendicular to the longitudinal rolls.

DOI: [10.1103/PhysRevResearch.2.033481](https://doi.org/10.1103/PhysRevResearch.2.033481)

I. INTRODUCTION

A horizontal layer of fluid under the action of a temperature difference ΔT represents an archetypal model for the understanding of pattern formation in nonequilibrium systems [1]. When the fluid is heated from below and the temperature difference between the boundaries exceeds a threshold value, a macroscopic convective flow develops inside the fluid and, through a symmetry breaking mechanism, gives rise to self-organized convective patterns [2]. Significantly, the system can be parametrized entirely in terms of the dimensionless Rayleigh number $Ra = \alpha g \Delta T h^3 / (\nu \chi)$ and Prandtl number $Pr = \nu / \chi$, where α is the thermal expansion coefficient, g is the acceleration of gravity, ν the kinematic viscosity, h is the thickness of the sample, and χ the thermal diffusivity. By adopting dimensionless units the same set of equations can be used to describe pattern formation across a wide range of length scales, from a few microns up to astrophysical distances. The geometry and symmetry of the patterns formed are strongly influenced by the boundary conditions. Most of the research on convection in single component fluids has been performed in the presence of ideal boundary conditions, such as horizontal layers of fluid and perfectly conducting boundaries [3]. However, the cases where conditions are not ideal have a remarkable relevance for the understanding of the behavior of natural systems, where the boundaries are in general not horizontal and conduct heat poorly. For example, masses of water [thermal conductivity

$\kappa_w = 0.60$ W/(m K)] at the Earth's surface are frequently bound by silicates at the bottom [$\kappa_c = 3$ W/(m K)] and air at the top [$\kappa_a = 2.6 \times 10^{-2}$ W/(m K)], which conduct heat poorly. Therefore, a deeper understanding of the role of poorly conducting—nonhorizontal—boundaries is of great interest for the modeling of convective heat transfer in natural systems as oceans and the atmosphere.

A first important model system to understand the influence of nonideal boundaries is represented by an inclined layer of fluid with conducting boundaries. In the absence of inclination the pattern formation process is entirely determined by the buoyancy force, which close to the threshold of the instability $Ra_c = 1708$, gives rise to randomly oriented parallel rolls with wave number $k = 3.117$. An inclination of the layer determines the onset of a large-scale flow (LSF), where the upper half of the layer flows downhill parallel to the upper boundary in the direction of inclination, while the bottom half of the layer flows uphill, parallel to the lower boundary. The LSF determines a shear stress on the layer of fluid, which strongly affects the convective patterns generated by buoyancy in the absence of inclination. A first effect of the tilt of the liquid layer is that for small inclination angles the convective rolls align parallel to the direction of inclination [4–7]. At larger inclination angles, a transition from longitudinal rolls to transverse rolls occurs [6,7]. Depending on the inclination angle, the Rayleigh number, and the Prandtl number, a complex scenario of convective patterns appears [8,9]. This scenario comprises dynamical configurations such as Busse oscillations, subharmonic oscillations, undulation chaos, longitudinal and transverse bursts [6,10–17]. Under these conditions, transitions between patterns are observed at large inclination angles, at least of the order of a few degrees, when the component of the gravity force parallel to the layer of liquid becomes large enough to promote a strong LSF, able to compete effectively with the vertical flow determined by Rayleigh-Bénard convection.

*alberto.vailati@unimi.it

Published by the American Physical Society under the terms of the Creative Commons Attribution 4.0 International license. Further distribution of this work must maintain attribution to the author(s) and the published article's title, journal citation, and DOI.

A notable exception to this behavior occurs in binary liquid mixtures, where even an inclination of the sample as small as few milliradians strongly affects the convective planform [18–22]. This feature of binary mixtures can be qualitatively understood by taking into account that in the case of solutal convection the boundaries are impermeable. Therefore, a perturbation of the concentration field cannot be dissipated by the boundaries and persists for a long time, thus determining a large scale flow even for small inclinations.

A second relevant case of nonideal boundary conditions for Rayleigh-Bénard convection in a single component fluid is represented by poorly conducting boundaries. In this case experiments [23,24] and theoretical modeling [25–28] have shown that when the Prandtl number is large enough ($Pr \geq 1$) and the thermal conductivity of the boundaries is comparable or smaller than that of the fluid, the convective planform is made by square cells, which represent the configuration that maximizes the transfer of heat [25]. The wave number k of the instability is strongly influenced by the thickness and thermal conductivity of the boundaries in relation to those of the sample and varies in an ample range, the two limiting cases being represented by perfectly conducting boundaries ($k = 3.117$) and perfectly insulating boundaries ($k = 0$). A convective square planform has been reported also for solutal convection in a binary liquid mixture, where the impermeable boundaries are formally analog to perfectly insulating boundaries in the thermal case. So far, the influence of inclination on pattern formation with impermeable or poorly conducting boundaries has been investigated mostly in binary liquid mixtures [18–20,22], but not in single component fluids with poorly conducting boundaries.

In this work we investigate the pattern formation process in a layer of liquid water with poorly conducting boundaries. We show that when the layer is horizontal the convective planform is made of square cells of wave number $k = 1.8 \pm 0.15$, in agreement with theoretical predictions of Riahi [28]. We show that close to the threshold for convection and in the presence of inclination angles larger than the critical angle $\delta_c = 14$ mrad the pattern is made of longitudinal rolls aligned parallel to the direction of inclination. The transition between the two structures can be obtained by varying continuously the inclination of the liquid layer, and displays hysteresis. By starting with a horizontal layer of liquid, the imposition of an inclination larger than $\delta_c = 14$ mrad determines the demolition of the square pattern to create the longitudinal rolls. Conversely, by removing the inclination in the presence of longitudinal rolls, a cross roll structure develops perpendicularly to them, and gives rise to the square pattern. The two transition processes occur with well separated timescales, the first being a factor 3 slower than the second one.

II. EXPERIMENT

The sample is a layer of ultra-pure water (Chem-Lab H₂O-LF 1 μ S, 0.4 μ m UV filtered) confined laterally by an O-ring with an inner diameter $\Phi = 49$ mm and sandwiched between two plexiglass windows with a diameter of 75 mm and a thickness of 5.15 mm (Fig. 1). The O-ring determines a lateral boundary that is only approximately cylindrical. Indeed, the lateral surface bounding the sample has a slight hourglass

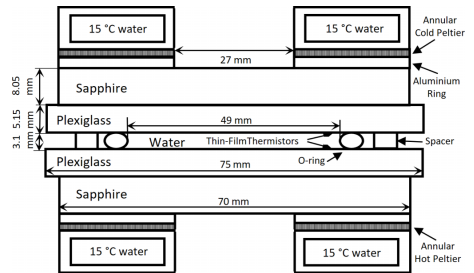


FIG. 1. Cross section of the thermal gradient cell. The two sapphire windows guarantee a uniform horizontal temperature distribution at the outer surface of the plexiglass windows, which confine a layer of liquid water in the vertical direction. The temperature difference imposed to the liquid layer is measured by using two thin-film thermistors thermally coupled to the inner surface of the plexiglass windows.

shape. However, due to the strong compression of the O-ring, the hourglass shape is not pronounced. We estimate that the maximum variation of the diameter of the sample as a function of height is less than 5%. This allows us to assume that the small deviation of the lateral boundary from a cylindrical shape does not influence the patterns significantly. The use of a circular lateral boundary guarantees that the square and roll patterns are not forced by a preferential orientation determined by the geometric shape of the lateral boundary, as it would happen in the presence of a rectangular geometry. The distance between the two plexiglass windows is determined by three calibrated spacers made of Delrin, with a thickness $h = 3.10$ mm. The relatively high aspect ratio $\Gamma = \Phi/(2h) = 7.9$ of the sample guarantees that the lateral boundaries do not affect significantly pattern formation at the center of the sample. The thermal conductivity of the plexiglass plates used to bound the sample is $\kappa_p = 0.18$ W/(m K), while for water $\kappa_w = 0.60$ W/(m K). Following previous theoretical work [25–28], the two dimensionless parameters that characterize the boundaries are the ratio of the thermal conductivities of the boundaries and of the sample $\zeta = 0.30$, and the ratio $\lambda = 3.3$ between the overall thickness of the boundaries and that of the sample. The fact that the sample and the boundaries have thermal conductivities of the same order of magnitude determines a deep penetration of the temperature field inside the plexiglass windows. The typical distance beyond which the imprint of the temperature field determined by the convective patterns is not felt any more inside the boundaries is of the order of the sample thickness h . The choice of boundaries with a thickness larger than h and a thermal conductivity smaller than that of the sample guarantees that the boundaries behave as poor conductors of heat [23].

The temperature of the sides of the plexiglass windows in contact with the sample is measured by two thin-film 10 k Ω thermistors, thermally coupled to the windows. Each of the two plexiglass windows is thermally and optically coupled to a sapphire window of thickness 8.05 mm and diameter of 70 mm by means of a thin layer of silicone oil with a

viscosity of 300 cSt (Dow Corning FS 1265). The temperature of the sapphire windows is controlled by two annular Thermo Electric Devices (TED), with an inner aperture that guarantees optical access to a circular region with a diameter of 27 mm. One side of each TED is thermally coupled to a sapphire window by means of an aluminium ring, while the other is in contact with an annular flange kept at a constant temperature of 15° by means of a water circulation thermostat. Due to their high thermal conductivity $\kappa_s = 36 \text{ W/(m K)}$ the sapphire windows guarantee a uniform temperature distribution on the sides of the plexiglass windows not in contact with the sample. Convective patterns are visualized by using the shadowgraph projection method [29]. All the optical components and the cell are fixed to a vertical optical bench rail with a length of 1.5 m, which can be inclined with an accuracy of 0.1 mrad by using tilt screws and a comparator to read the tilt angle. The leveling of the system is calibrated and checked regularly by using a precision frame level with an accuracy of $20 \mu\text{rad}$. In this way, the optical diagnostics and the thermal gradient cell can be tilted as a whole, and this avoids optical deformations of the visualized convective patterns. The light source is a super-luminous light emitting diode (Superlum SLD 261-MP-DIL-SM-PD) with a wavelength of 676.5 nm and a bandwidth of 14.1 nm, coupled to a monomode optical fiber. The output of the fiber lies in the focal plane of an achromatic doublet of focal length 500 mm, which collimates the light onto the cell. An achromatic doublet with a focal length of 300 mm placed after the cell conjugates a plane located at a distance $z = 135 \text{ cm}$ from the sample onto a Jai-CVM300 charge coupled array detector (CCD) with a resolution of 768×576 pixels. The defocusing distance z allows to work in a shadow configuration, where the propagation of light transforms phase modulations determined by the convective structures into amplitude modulations that can be recorded by the CCD [29,30]. A reference image taken in the absence of a temperature gradient was subtracted to each shadowgraph image to get rid of the optical background determined by spatial inhomogeneities in the illumination of the sample.

The features of the convective pattern depend on the Rayleigh number, the Prandtl number, and the boundary conditions. In our case the Prandtl number is fixed at $\text{Pr} = 7$, while the Rayleigh number and the boundary conditions can be varied. More in detail, as far as the boundary conditions are concerned, the aspect ratio $\Gamma = 7.9$ and the ratio of the thermal conductivity of the plexiglass windows and that of the water sample are fixed, while the inclination δ of the liquid layer can be changed as described above.

III. RESULTS

After leveling accurately the cell in the horizontal position, we performed a set of test measurements aimed at determining the experimental conditions needed to generate square patterns. An external temperature difference in the range 20–60 K was applied to the sample, and the effective temperature difference imposed to the sample was recorded by using the two thin-film thermistors. After a transient time of the order of 5000 s the rearrangement of the convective patterns gave rise to stable square patterns for Rayleigh numbers in the range $1500 < \text{Ra} < 2800$ [Fig. 2(a)], the upper limit being

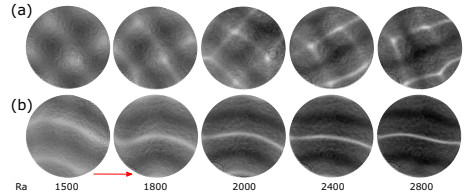


FIG. 2. Square patterns and longitudinal rolls formed in the absence and in the presence of inclination. (a) Stationary square patterns; (b) stationary longitudinal rolls formed in the presence of an inclination of 27 mrad. The arrow marks the projection of the direction of steepest ascent of the boundaries. The diameter of each panel corresponds to 27 mm.

determined by the performances of the TEDs. The stability of the square patterns in the absence of inclination was checked by performing measurements lasting as long as 12 h.

A similar set of measurements was performed by imposing an inclination angle of 27 mrad and applying to the sample the same temperature differences used to obtain the square pattern. Under these conditions, the patterns exhibited a longitudinal roll structure, aligned parallel to the direction of inclination [Fig. 2(b)].

A. Phase space

We investigated systematically the geometry of the convective patterns by preparing the sample at a fixed inclination and suddenly applying a stable temperature difference to it. The time needed for the stabilization of the vertical temperature profile through the boundaries and the sample is of the order of $\tau_T \approx 2800 \text{ s}$.

After a stabilization time of the order of 5000 s, of the same order of magnitude of τ_T , the patterns reached a stable configuration characterized either by the formation of a square pattern, or by longitudinal rolls aligned parallel to the direction of inclination of the sample. Figure 3 summarizes the phase space of the convective patterns, as a function of the Rayleigh number and inclination angle. Patterns become visible when the Rayleigh number exceeds the critical value $\text{Ra}_{c1} = 1300$, smaller than the critical Rayleigh number $\text{Ra}_c = 1708$ associated to Rayleigh-Bénard convection with conductive boundaries. From Fig. 3 one can appreciate the presence of a transition between square and roll patterns, occurring at a critical value of the inclination angle of the order of $\delta_c \approx 14 \text{ mrad}$ for Rayleigh numbers $\text{Ra} < 2400$. This transition occurs by increasing the inclination angle $\delta = 13 \text{ mrad}$ by about 2 mrad. This results in a tiny increase, of the order of $g/500$, of the in-plane component of the acceleration of gravity $g\sin(\delta) \approx g/80$. Measurements performed in the absence of inclination allowed us to perform a direct comparison with the dimensionless wave number of square structures determined theoretically for a horizontal layer of fluid with $\lambda = 1$ [26,27] and $\lambda = \infty$ [25,28] [Fig. 4(a)]. From the comparison one can appreciate that our experimental result $k = 1.8 \pm 0.15$, obtained with $\lambda = 3.3$, is fully compatible with the theoretical result $k = 1.76$, obtained for $\lambda = \infty$ [25,28]. Conversely, our

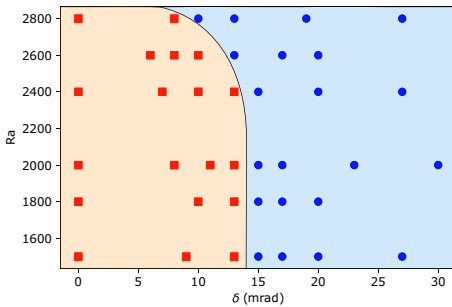


FIG. 3. Phase space. Geometry of the patterns plotted as a function of the inclination angle and of the Rayleigh number. Square symbols indicate square patterns, while circles represent longitudinal rolls. One can appreciate the presence of the transition between the two geometries, qualitatively indicated by the solid line separating the amber and a light blue regions.

results is not compatible with the theoretical value $k = 2.16$ obtained for $\lambda = 1$ [26,27]. These results suggest that a thickness ratio $\lambda = 3.3$ like the one adopted by us is large enough to mimic effectively the ideal condition of a insulating boundaries of infinite thickness.

Previous experiments reported square structures obtained in single components liquids with poorly conductive boundaries. However, these experiments were performed with boundary conditions that do not allow a fully quantitative comparison with theoretical predictions. The first evidence of

a square pattern was obtained by Legal and Croquette for a sample of liquid water ($Pr = 7$) [23]. They found $k = 2.5$ and they attempted a qualitative comparison with the theoretical predictions by Proctor [26] and Riahi [28]. A quantitative comparison was prevented by the complex boundary conditions adopted in the experiment, which made a straightforward estimation of ζ and λ not possible: A 4.0-mm-thick sample of water was bound by two plexiglass windows with a thickness of 8.0 mm sandwiched by two glass windows of thickness 12.7 mm flushed by thermostated water that allowed to control independently the temperature of each window. Shadid and Goldstein reported square structures in a sample of ethylene glycol ($Pr = 90$) [24]. They used a thermosensitive liquid crystal sheet to visualize the convective structures. This method allowed them to perform systematic measurements of the wave number of the square structures as a function of inclination angle. In the absence of inclination the wave number was found to be $k = 2.6 \pm 0.35$, fully compatible with the experimental result by Legal and Croquette [23]. However, the clever visualization method chosen by Shadid and Goldstein required to adopt asymmetric boundary conditions, where the bottom part of the fluid was in contact with a complex sandwich made by a transparent mylar sheet (0.10 mm), a liquid-crystal layer (0.10 mm), a polyester film coated with gold (0.12 mm), a thick lexan layer (22 mm), and a thick extruded polystyrene layer (50.8 mm); the top of the liquid layer was in contact with a high strength glass plate flushed with thermostated water. The complex geometry adopted in the experiment by Shadid and Goldstein also prevents the determination of the thermal conductivity ratio ζ and of thickness ratio λ , thus making a fully quantitative comparison with theoretical predictions impossible. To our knowledge, our results represent the first quantitative experimental confirmation of the theoretical model developed by Riahi for Rayleigh-Bénard convection in single component fluids with poorly conducting boundaries [28].

B. Wave number

We investigated systematically the dependence of the wave number from the inclination angle. Measurements performed by changing the inclination of the sample from 0 to 40 mrad showed that the wave number varies in the range $1.5 < k < 1.8$, and is not significantly affected by the transition from square patterns to longitudinal rolls occurring at $\delta \approx 14$ mrad [Fig. 4(b)]. As far as we know, the only other experimental results for convection in an inclined single component liquid with poorly conducting have been obtained by Shadid and Goldstein in the experiments with ethylene glycol ($Pr = 90$) detailed above [24]. In the range of very small inclination angles explored by us they found $2.5 < k < 2.8$ [Fig. 4(b)], a result that differs significantly from the one found by us, due to the different boundary conditions adopted. However, it must be stressed here that both our results and those of Shadid and Goldstein have been obtained with poorly conducting boundaries, a configuration that differs significantly from the one where the boundaries conduct heat well, a condition that has been investigated extensively, both theoretically and experimentally for $Pr = 1.07$ [8,9,16,17]. Experiments and theoretical models performed with perfectly conducting

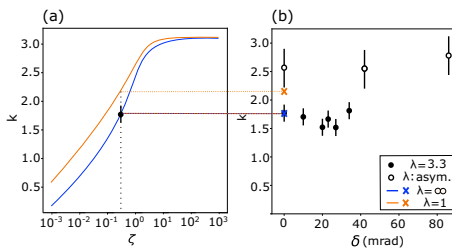


FIG. 4. Wave number of convective patterns. (a) Wave number of the pattern in the absence of inclination as a function of the ratio ζ of the thermal conductivities of the boundaries and of the sample. The orange and blue lines are the theoretical predictions of Proctor ($\lambda = 1$) [26,27], and Riahi ($\lambda = \infty$) [28], respectively. Full circles in panels (a) and (b) correspond to the wave numbers of square patterns measured by us in water ($\zeta = 0.3$, $\lambda = 3.3$ and $Pr = 7.0$) averaged in the range of Rayleigh numbers $1500 \leq Ra \leq 2800$. (b) Wave number of the convective patterns plotted as a function of the inclination angle. The orange and blue crosses represent the extrapolation at $\zeta = 0.3$ of the theoretical curves shown in panel (a). Open circles are the experimental results by Shadid and Goldstein [24] for ethylene glycol with $Pr = 90$ and asymmetric boundaries made by the superposition of layers of poorly conducting materials.

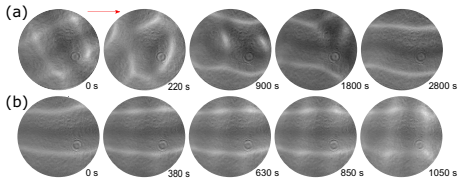


FIG. 5. Time evolution of the transition between the square and longitudinal roll patterns. (a) Transition from square to longitudinal roll pattern; (b) transition from longitudinal roll to square pattern. Time $t = 0$ corresponds to the instant where an inclination of 27 mrad was either imposed or removed from the layer of liquid to trigger a shear stress. During the measurements the Rayleigh number was kept at a constant value $Ra = 1800$. Each frame has a diameter of 27 mm. The arrow marks the projection of the direction of steepest ascent of the boundaries.

boundaries and in the absence of inclination show that the convective planform is made by parallel rolls with wave number $k = 3.117$. By tilting the liquid layer the rolls align parallel to the direction of inclination. As it will be discussed in more detail below, in contrast with our results, this reorientations of the rolls occurs in the absence of a threshold inclination.

C. Square-Longitudinal Roll Transition

To investigate the mechanism of the transition between square and longitudinal roll patterns, we recorded sequences of shadowgraph images by keeping the sample at a constant Rayleigh number and changing its inclination rapidly, in a time of the order of a few seconds. The sample was initially kept horizontal at $Ra = 1800$ [Fig. 5(a), 0 s] until a stable square pattern was obtained. The inclination was then suddenly changed from 0 to 27 mrad, and a first sequence of images was acquired until a stable roll pattern was obtained [Fig. 5(a), 220–2800 s]. The inclination was then removed and a second sequence of images was acquired [Fig. 5(b)]. From the two image sequences it is apparent that the mechanism of the square-to-roll transition is different from the one of the roll-to-square transition. In the first case, a first phase of the transition involves the complete demolition of the square pattern, which subsequently reorganizes to form the roll one. In the second case, a transverse roll structure grows perpendicularly to the longitudinal one, leading to the formation of a square pattern aligned to the roll one. The asymmetry between the two transitions is also reflected by their dynamics. In fact, the transition from the square pattern to longitudinal rolls is about three times faster than the one from longitudinal rolls to the square pattern. In the range of Rayleigh numbers $1500 \leq Ra \leq 2800$ that characterizes the transition we do not observe a significant variation of the timescales of the transition in the two directions. Conversely, when the inclination is applied the transition time appears to be affected by the depth of penetration into the longitudinal rolls region. More in detail, the sudden imposition or removal of a tilt angle of 56 mrad gives rise to transitions between squares and longitudinal rolls a factor 4.7 faster than the ones reported at an angle of 27 mrad. We point out that the

timescales involved in these transitions are strongly affected by the path in the phase space followed to reach the initial and final state. This prevents a fully quantitative investigation of the kinetics of the transition, because it would be in principle affected by a huge number of parameters.

IV. DISCUSSION AND CONCLUSIONS

The investigation of the effect of inclination on convection in single component fluids with $Pr \approx 1$ in the presence of conducting boundaries has shown that this system exhibits a rich phase space, which can be roughly divided into two main regions close to the threshold for Rayleigh-Bénard convection [8]: (i) for inclinations smaller than 77.5° the convective planform is made of longitudinal rolls. Longitudinal rolls are formed through the alignment of the roll pattern observed close to threshold in the absence of inclination, due to the symmetry breaking determined by the large scale flow induced by the inclination; (ii) drifting transverse rolls develop at inclination angles larger than 77.5° . Interestingly, the transition to randomly aligned rolls in the absence of inclination to longitudinal rolls in the presence of inclination is continuous, and occurs in the absence of a threshold inclination angle [8]. Conversely, our results in the presence of poorly conductive boundaries provide clear evidence of the presence of a transition between square and roll patterns determined by the inclination at a threshold inclination $\delta \approx 14$ mrad.

At such small inclination angles the component of the acceleration driving the large scale flow is about two orders of magnitude smaller than the acceleration of gravity itself. The fact that such a small component of the acceleration of gravity can induce a transition between convective planforms is a unique feature of the presence of poorly conducting boundaries. In fact, poorly conducting boundaries are not able to dissipate effectively heat, and a small temperature perturbation inside the fluid can survive for a long time and drive the large scale flow effectively, even in the presence of a small inclination. More quantitatively, in the presence of highly conductive boundaries the conductive dissipation of temperature inhomogeneities with the wave number of the convective structures would occur almost instantaneously close to the boundaries, leading to isothermal boundary layers. Conversely, in the presence of poorly conducting boundaries the temperature distribution at their surfaces becomes highly inhomogeneous in the presence of convection. This effect has been demonstrated experimentally by Shadid and Goldstein by using a thermosensitive liquid crystal layer in contact with the sample [24]. Under these conditions, the conductive dissipation of the temperature inhomogeneities would require a conduction time of the order of $\tau_c = [\kappa_w (kh)^2]^{-1} \approx 53\,000$ s ≈ 15 h, and even a small inclination of the liquid layer can drive a LSF.

This condition is qualitatively similar to the one encountered in a binary liquid mixture with positive Soret coefficient heated from below [31–33]. In fact, in this system the boundaries are impermeable to the transport of mass, a condition that mirrors insulating boundaries in Rayleigh-Bénard convection. In the absence of inclination, square patterns can develop in a horizontal layer of a binary mixture [18,32]. When subjected to a small tilt of the order of a few milliradians a transition

between the square pattern and a drifting centered-rectangular one occurs [18,21]. The drifting pattern is made by parallel rows of ascending and descending columns of fluid moving into opposite directions parallel to the inclination of the fluid layer, in a *superhighway convection* (SHC) configuration resembling alternate rows of traffic on a highway. The simulation of this kind of system by using Boussinesq Navier Stokes equations has shown that the large scale flow gives rise to the formation of a concentration gradient parallel to the direction of inclination, determined by the stratification of the concentration along the direction of inclination [20,34]. The periodic SHC solution found for a binary mixture is strictly related to the presence of this horizontal density gradient, which is not present in a single component fluid, and this explains why we do not observe these structures in a single component fluid.

A further understanding of pattern formation in inclined layers of fluid with poorly conducting boundaries would require the utilization of combinations of fluid samples and boundaries with a ratio ζ of thermal conductivities spanning several orders of magnitude. This kind of requirement is difficult to fulfill in real experiments, but could be implemented effectively by means of computer simulations.

ACKNOWLEDGMENTS

The authors acknowledge discussion with F. Scheffold. Work partially supported by the European Space Agency, CORA-MAP TechNES Contract No. 4000128933/19/NL/P.G.

-
- [1] M. Cross and P. Hohenberg, *Rev. Mod. Phys.* **65**, 851 (1993).
 - [2] S. Chandrasekhar, *Hydrodynamic and Hydromagnetic Stability* (Oxford University Press, Oxford, UK, 1961).
 - [3] E. Bodenschatz, W. Pesch, and G. Ahlers, *Annu. Rev. Fluid Mech.* **32**, 709 (2000).
 - [4] J. E. Hart, *J. Fluid Mech.* **47**, 547 (1971).
 - [5] J. E. Hart, *J. Fluid Mech.* **48**, 265 (1971).
 - [6] R. M. Clever and F. H. Busse, *J. Fluid Mech.* **81**, 107 (1977).
 - [7] K. Fujimura and R. E. Kelly, *J. Fluid Mech.* **246**, 545 (1993).
 - [8] K. E. Daniels, B. B. Plapp, and E. Bodenschatz, *Phys. Rev. Lett.* **84**, 5320 (2000).
 - [9] P. Subramanian, O. Brausch, K. E. Daniels, E. Bodenschatz, T. M. Schneider, and W. Pesch, *J. Fluid. Mech.* **794**, 719 (2016).
 - [10] F. H. Busse and R. M. Clever, *Phys. Fluids* **12**, 2137 (2000).
 - [11] K. E. Daniels and E. Bodenschatz, *Phys. Rev. Lett.* **88**, 034501 (2002).
 - [12] G. Seiden, S. Weiss, J. H. McCoy, W. Pesch, and E. Bodenschatz, *Phys. Rev. Lett.* **101**, 214503 (2008).
 - [13] K. E. Daniels, O. Brausch, W. Pesch, and E. Bodenschatz, *J. Fluid. Mech.* **597**, 261 (2008).
 - [14] A. Zebib and M. M. Bou-Ali, *Phys. Rev. E* **79**, 056305 (2009).
 - [15] O. Zier, W. Zimmermann, and W. Pesch, *J. Fluid. Mech.* **874**, 76 (2019).
 - [16] F. Reetz and T. Schneider, *J. Fluid Mechanics* **898**, A22 (2020).
 - [17] F. Reetz, P. Subramanian, and T. Schneider, *J. Fluid Mechanics* **898**, A23 (2020).
 - [18] F. Croccolo, F. Scheffold, and A. Vailati, *Phys. Rev. Lett.* **111**, 014502 (2013).
 - [19] M. Italia, F. Croccolo, F. Scheffold, and A. Vailati, *Eur. Phys. J. E* **37**, 101 (2014).
 - [20] A. Alonso, I. Mercader, and O. Batiste, *Phys. Rev. E* **97**, 023108 (2018).
 - [21] F. Croccolo, S. Castellini, F. Scheffold, and A. Vailati, *Phys. Rev. E* **98**, 063104 (2018).
 - [22] I. Mercader, O. Batiste, A. Alonso, and E. Knobloch, *Phys. Rev. E* **99**, 023113 (2019).
 - [23] P. Le Gal and V. Croquette, *Phys. Fluids* **31**, 3440 (1988).
 - [24] J. Shadid and R. Goldstein, *J. Fluid Mech.* **215**, 61 (1990).
 - [25] F. F. Busse and N. Riahi, *J. Fluid Mech.* **96**, 243 (1980).
 - [26] M. R. E. Proctor, *J. Fluid Mech.* **113**, 469 (1981).
 - [27] D. R. Jenkins and M. R. E. Proctor, *J. Fluid. Mech.* **139**, 461 (1984).
 - [28] N. Riahi, *J. Fluid. Mech.* **152**, 113 (1985).
 - [29] G. S. Settles, *Schlieren and Shadowgraph Techniques: Visualizing Phenomena in Transparent Media*, 1st ed., Experimental Fluid Mechanics (Springer-Verlag, Berlin/Heidelberg, 2001).
 - [30] F. Croccolo and D. Brogioli, *Appl. Optics* **50**, 3419 (2011).
 - [31] C. Jung, B. Huke, and M. Lücke, *Phys. Rev. Lett.* **81**, 3651 (1998).
 - [32] E. Moses and V. Steinberg, *Phys. Rev. Lett.* **57**, 2018 (1986).
 - [33] P. Le Gal, A. Pocheau, and V. Croquette, *Phys. Rev. Lett.* **54**, 2501 (1985).
 - [34] I. Mercader, O. Batiste, and A. Alonso, *Comput. Fluids* **39**, 215 (2010).



Transient Localized Rotating Structures in a Suspension of Highly Thermophilic Nanoparticles

Marina Carpineti, Stefano Castellini, Andrea Pogliani and Alberto Vallati*

Dipartimento di Fisica "A. Pontremoli", Università degli Studi di Milano, Milano, Italy

A thermophilic suspension of nanoparticles heated from below exhibits a complex stability diagram determined by the competition between the stabilizing flux of nanoparticles induced by thermophoresis and the destabilizing flux determined by thermal convection. We investigate Rayleigh-Bénard convection in a suspension of highly thermophilic nanoparticles with large negative separation ratio $\psi = -3.5$ heated from below. We show that transient localized states appear in the range of Rayleigh numbers $2200 < Ra < 3000$. These states rotate rapidly around their axis and gradually shrink in size until the system returns in a purely conductive state. We discuss how these states are originated by the travelling waves arising from the competition between Rayleigh-Bénard convection and the solutal stabilisation of the sample.

Keywords: thermophilic nanoparticles, Rayleigh-Bénard convection, travelling waves, localized structures, convectons

OPEN ACCESS

Edited by:

Ramon Castañeda-Priego,
University of Guanajuato, Mexico

Reviewed by:

Alokmay Datta,
University of Calcutta, India
Sutapa Roy,
Indian Institute of Technology
Gandhinagar, India

*Correspondence:

Alberto Vallati
alberto.vallati@unimi.it

Specialty section:

This article was submitted to
Soft Matter Physics,
a section of the journal
Frontiers in Physics

Received: 25 May 2022

Accepted: 22 June 2022

Published: 14 July 2022

Citation:

Carpineti M, Castellini S, Pogliani A and
Vallati A (2022) Transient Localized
Rotating Structures in a Suspension of
Highly Thermophilic Nanoparticles.
Front. Phys. 10:953067.
doi: 10.3389/fphy.2022.953067

1 INTRODUCTION

In the presence of a density stratification, a layer of fluid exhibits a rich phenomenology determined by the action of gravity that can lead to oscillations and wave propagation [1, 2]. A typical case is represented by a single component fluid heated from below, where the stratification is determined by the thermal dilation of the fluid, which can transfer heat either in a conductive or in a convective regime. The stability of the system is parametrized by the dimensionless Rayleigh number $Ra = \frac{\alpha g \Delta T h^3}{\nu \kappa}$, which quantifies the applied thermal stress. Here α is the thermal expansion coefficient, g the acceleration of gravity, ΔT the temperature difference, h the thickness of the layer, ν the kinematic viscosity, and κ the thermal diffusivity. The transfer of heat is parametrized by the Nusselt number Nu , which represents the ratio between the heat transferred by the fluid and the one transferred by conduction only. For a layer of fluid of infinite aspect ratio $r = \Phi/h$, where Φ is the diameter of the layer of fluid, the transfer of heat is conductive ($Nu = 1$) when the Rayleigh number is below the threshold value $Ra_c = 1708$, while it occurs by convection ($Nu > 1$) above the threshold (Figure 1). The addition of a second component to the fluid dramatically alters the stability of the layer. More in detail, the temperature gradient imposed to the fluid gives rise to a non-equilibrium mass flux determined by the Ludwig-Soret effect: $j = -\rho D [\nabla c - c(1-c)S_T \nabla T]$, where ρ is the density of the sample, D the diffusion coefficient, c the weight fraction concentration, and S_T the Soret coefficient. As a result, the density profile inside the sample becomes affected both by the vertical temperature and concentration profiles of the fluid. The case of a suspension of thermophilic particles heated from below is particularly interesting, because in this case the stabilizing flux of nanoparticles induced by thermophoresis competes with the destabilizing flux determined by thermal convection. The relative weight of these two contributions is expressed by the separation ratio $\psi = \Delta \rho_s / \Delta \rho_T$, which represents the ratio between the density differences $\Delta \rho_s$

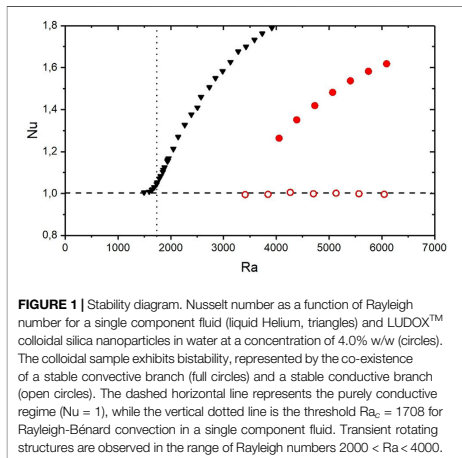


FIGURE 1 | Stability diagram. Nusselt number as a function of Rayleigh number for a single component fluid (liquid Helium, triangles) and LUDOX™ colloidal silica nanoparticles in water at a concentration of 4.0% w/w (circles). The colloidal sample exhibits bistability, represented by the co-existence of a stable convective branch (full circles) and a stable conductive branch (open circles). The dashed horizontal line represents the purely conductive regime ($Nu = 1$), while the vertical dotted line is the threshold $Ra_c = 1708$ for Rayleigh-Bénard convection in a single component fluid. Transient rotating structures are observed in the range of Rayleigh numbers $2000 < Ra < 4000$.

and $\Delta\rho_T$ determined by solutal and thermal expansion, respectively. In the case of a separation ratio in the range $-1 < \psi < 0$ this competition determines the onset of travelling waves, accompanied by the presence of localized pulses of convection, localized states and convectons [3–14]. The case $\psi < -1$ is particularly interesting, because in this case the stabilizing effect determined by the Soret flux dominates, and the transfer of heat occurs in the conductive regime, irrespectively of the magnitude of the imposed temperature gradient. However, experiments performed on suspensions of strongly thermophilic nanoparticles with $\psi = -3.5$ and $\psi = -7.5$ have shown that the behaviour of the system is strongly affected by the initial conditions [15, 16]. When the temperature gradient is imposed gradually, nanoparticles migrate towards the bottom of the fluid and give rise to a density profile that completely stabilizes the layer of fluid against Rayleigh-Bénard convection. Under this condition, the transfer of heat occurs by conduction. Conversely, when the temperature gradient is imposed rapidly and the particles are initially dispersed uniformly, convective motions set in and, provided that the Rayleigh number is large enough, keep the particles dispersed and convection lasts indefinitely. The theoretical investigation of the stability of a strongly thermophilic colloidal suspension with large negative separation ratio has shown that the competition between Rayleigh-Bénard convection and the stabilizing effect determined by the Soret effect leads to a transient oscillatory instability [17]. The analysis of the role of the settling of the nanoparticles showed that the presence of a sedimentation profile leads to the oscillatory onset of convection [18] and to the development of travelling waves [19, 20]. Under these conditions, an additional parameter affecting the stability of the system is represented by the sedimentation length $l_g = k_B T / (\Delta\rho V g)$, which characterizes the typical length scale of variation of the concentration profile (here $\Delta\rho$ is the density

mismatch between the particle and the carrier fluid, and V is the volume of the particle). The investigation of experimental conditions where the settling of particles is not strong and the sedimentation length l_g is comparable or larger than the sample thickness showed that a decrease of l_g is accompanied by a decrease of the convection threshold and of the frequency of neutral oscillations [21]. The analysis of the interplay between the combined effects of sedimentation, thermophoresis with negative separation ratio and convection led to the discovery of a new travelling wave solution, characterized by an anharmonic distribution of the vertical velocity across the sample layer [22]. Two dimensional simulations performed under conditions mirroring those adopted in experiments on a Hyflon MFA colloidal suspension [15], characterized by $\psi = -7.5$, showed recently that including the effect of gravitational sedimentation allows to achieve a quantitative estimate of the lifetime of the oscillatory flow as a function of Rayleigh number [20].

In this work we focus on the investigation of transient Rayleigh-Bénard convection in a suspension of highly thermophilic nanoparticles with large negative separation ratio $\psi = -3.5$ heated from below, under experimental conditions similar to those employed in theoretical studies [20–22]. We show that transient localized states appear in the range of Rayleigh numbers $2200 < Ra < 3000$ after the sudden imposition of a thermal gradient to a suspension of uniformly distributed nanoparticles. These states rotate rapidly around their axis, and gradually shrink in size, until they disappear and the system returns in a purely conductive state. We provide a quantitative characterization of the wave number and angular velocity of the localized states and we discuss our results in comparison with previous theoretical models and simulations summarized above.

The study of spatially localized states is of great interest in the field of pattern formation, as they appear in a great variety of physical and biological systems [23, 24]. In the case of localized stationary convective states, they take the name of *convectons*, and there is a growing number of works studying them from a theoretical, computational and experimental point of view [10, 23, 25–27].

2 METHODS

2.1 The Sample

The sample chosen for the experiment is a colloidal suspension made by distilled water and LUDOX™ TMA, a commercial colloid made of silica nanoparticle with an average diameter of 22 nm. In this work we have used concentrations of 4.0% w/w. The thermophysical properties are detailed in **Table 1**. This sample has been selected as a model system for the investigation of thermophoresis at the mesoscopic scale in the absence of gravity within the framework of the Giant Fluctuations and TechNES space projects of the European Space Agency [28, 29]. Within these projects, a series of experiments will be performed on the International Space Station to investigate the non-equilibrium fluctuations determined by the thermophoretic

TABLE 1 | LUDOX™ TMA thermo-physical properties.

Quantity	Diameter (nm)	D	D_T	α	ν	β	S_T
Value	22	$2.2\text{e-}7\text{cm}^2/\text{s}$	$1.52\text{e-}3\text{cm}^2/\text{s}$	$2.97\text{e-}4\text{K}^{-1}$	$8.18\text{e-}3\text{cm}^2/\text{s}$	0.57	$-4.7\text{e-}2\text{K}^{-1}$

process. Preliminary studies performed on Earth under isothermal conditions showed the presence of a peculiar relaxation dynamics of non-equilibrium concentration fluctuations, characterized by anomalous diffusion at large wave vectors [30]. For these reasons, it is very important to achieve a full understanding of the stability of this colloidal suspension in the presence of gravity.

2.2 Experimental System

The central element of the apparatus is a thermal gradient cell, consisting in a layer of fluid confined by two sapphire plates through which a thermal gradient can be applied. The heating elements are two ring-shaped Thermo Electric Devices (TED) thermally coupled to the sapphire plates. The other side of both the TED elements is in contact with a thermal reservoir, consisting of two annular aluminium chambers, inside which there is a steady flow of water at constant temperature. The purpose of this reservoir is to remove the excess heat. The cell is mounted on an optical bench in the configuration where the sample layer is horizontal, and is illuminated by a superluminescent diode (Superlum SLD-261) with central wavelength 670 nm. The limited temporal coherence of the source avoids interference determined by multiple reflections of the beam on the surfaces of the cell windows. The sensor employed is a monochrome CCD Camera (JAI CV-M300) with a resolution of 576×768 pixels and a depth of 8 bit, operating at a frame rate of 10 images per second. An achromatic doublet with focal length of 30 cm, placed between the sample cell and the camera images a plane at distance $z = -90.6 \pm 0.5$ cm from the sample in a shadowgraph configuration that allows to visualize the self-organized structures generated by the convective motions. The camera is controlled remotely by a computer through a National Instrument PCI-1407 frame-grabber.

3 RESULTS

Heat conduction in fluids is greatly affected by the presence of colloidal particles that exhibit a thermophilic behaviour. In particular, the presence of even a small amount of thermophilic particles has a stabilizing effect when the suspension is heated from below and, as a result, the sample can transfer heat either in a conductive or in a convective regime, depending on the initial condition (Figure 1) [15, 16]. The conductive regime can be accessed by imposing slowly a temperature difference to the sample heating from below, so that the thermophilic particles accumulate at the bottom of the cell and stabilize the sample against Rayleigh-Bénard convection. The convective regime can be accessed by first heating the sample from above to determine the accumulation of nanoparticles at the top of the cell, and then suddenly reversing the temperature

gradient by heating from below. Under these conditions a Rayleigh-Bénard instability starts and the accumulation of the thermophilic particles at the bottom of the cell is prevented by the convective flow that keeps the particles mixed. Conversely, if the temperature gradient is reversed by slowly heating from below thermophoresis determines the rapid formation of a stable boundary layer at the bottom of the cell and the system ends up in the conductive regime.

The bistable heat transfer is currently a well established feature of strongly thermophilic nanoparticles [15, 16], but bistability is apparent only for Rayleigh numbers $Ra > 4000$. Below this value of the Rayleigh number and above the threshold for Rayleigh-Bénard convection $Ra_c = 1708$ the system exhibits transient convective behaviour when heated from below, but eventually the stabilization determined by the particles dominates and the system enters into a purely conductive regime.

In order to study the transient convective regime in this range of Rayleigh numbers we have performed experiments according to the following procedure: i) The sample is heated from above for 1 h, applying a temperature difference $\Delta T = 10.5\text{K}$. This ensures that, because of the strong thermophilic behaviour of LUDOX™ TMA, the colloidal particles diffuse towards the upper plate, and the sample enters a regime of solutal convection [31–33]. The time needed to enter this solutal convective regime has been determined empirically. Physically, it corresponds to the diffusive time $\tau_\delta = \delta^2/D$ needed for the formation of a thin—unstable—boundary layer of thickness δ at the top of the cell, and is affected by the size of the nanoparticles through their diffusion coefficient D . ii) The temperature gradient is abruptly reverted to a negative value. In our tests we used temperature differences of $\Delta T = -3.00\text{K}$, -3.38K , -3.75K , -4.13K . iii) shadowgraph images of the sample are recorded with a frame rate of, approximately, 10 images/second.

Under these conditions, when the sample is first heated from above at the beginning of the experiment, solutal convection destabilizes the suspension (Figure 2A) so that, when the gradient is inverted, a convective instability develops in the sample, even when the sample is below the threshold needed for the development of stationary Rayleigh-Bénard convection in the nanofluid (Figure 2). At the beginning, the convective patterns are the usual convective rolls that characterize Rayleigh-Bénard convection, spanning all the area of the cell. After some time, the patterns begin to rotate around the vertical axis (clockwise or anticlockwise, indifferently). Subsequently, convection begins to die out starting from the borders of the cell, giving rise to the formation of a single rotating localized pattern. Eventually, the rotating pattern shrinks in size, until it disappears completely and the sample reaches the stationary conductive state. The duration of the entire phenomenon, measured from the inversion of the gradient, is of the order of

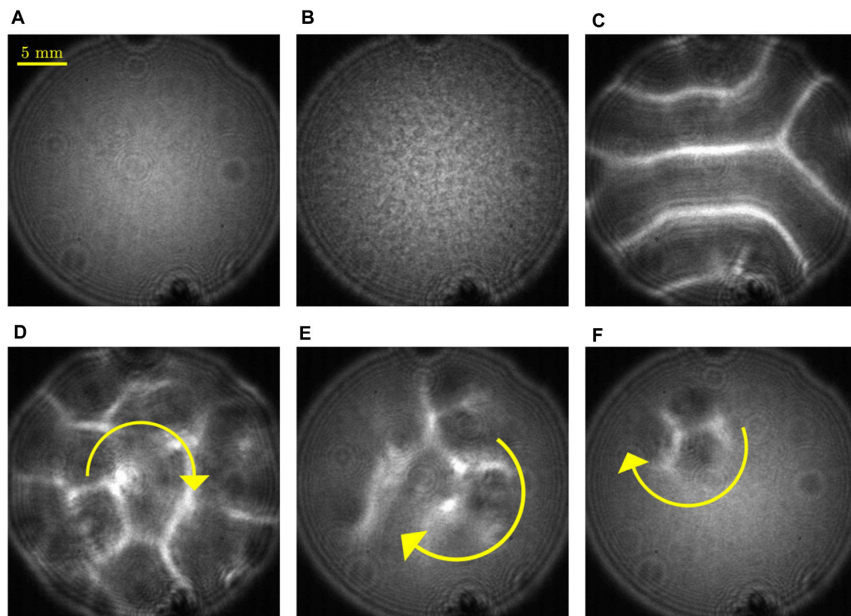


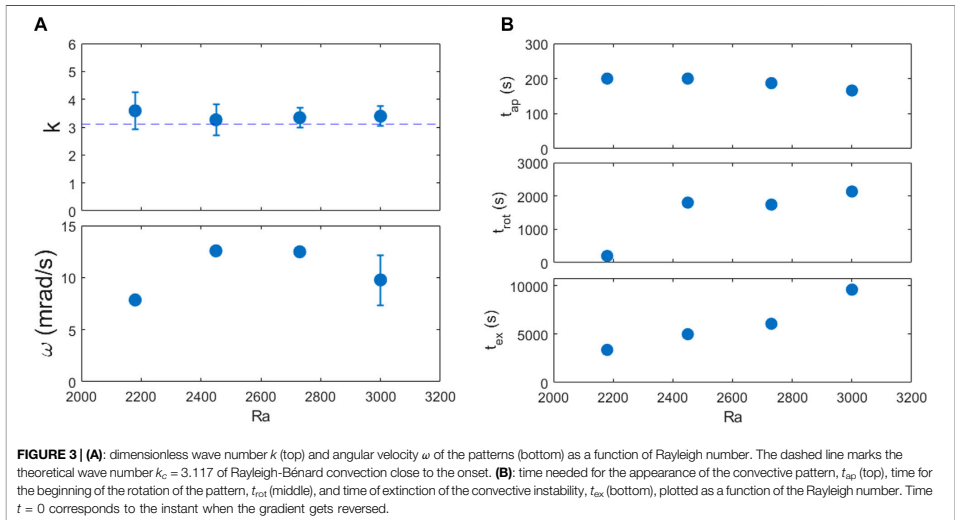
FIGURE 2 | Image sequence representing the evolution of the convective instability in a 3.1 mm thick layer of LUDOX™ TMA 4% w/w. **(A)** at the beginning, heating from above with a temperature difference of 10.5K, no macroscopic motions are present; **(B)** after a time of the order of tens of minutes solutal convection develops in the cell; **(C)** after 1 h, the temperature difference is inverted and set to -4.13 K. In, approximately 3 min thermal convective rolls appear in the sample; **(D)** the rolls, after a time that depends on the Rayleigh number, start to rotate; **(E)** they die out starting from the borders; **(F)** they gradually shrink in size, until they finally disappear.

1–3 h. The same phenomenology is observed for all temperature differences studied.

By looking at sequences of images, we measured some characteristic parameters of the localized states as a function of Rayleigh number. The interesting quantities are the wave vector k of the patterns and their angular velocity ω , and the typical timescales t_{ap} needed for the appearance of the convective structure, t_{rot} needed for the rotation of the pattern to start, and t_{ex} needed for the patterns to disappear. The results are summarized in **Figure 3**.

The characteristic wave vector k is compatible with the value 3.117 predicted for Rayleigh-Bénard convection close to the threshold. The angular velocity of the patterns has been determined from the visual observation of a large number of complete revolutions of the localized pattern (typically 10–20 revolutions). In selecting the maximum number of revolutions to consider for a reliable determination of the angular velocity we relied on the fact that the structure of the rotating pattern needed to be preserved, so that the motion of the spatial features of the patterns could be followed during their rotation. This method proved to be more effective and immune to errors than the automatic processing of the angular correlations.

The rotation of the patterns is very slow, a complete revolution taking a time in the range 500–800 s. The time t_{ap} needed for the appearance of the structures is of the order of 200 s, and slightly decreases as the Rayleigh number increases. The behaviour of the time t_{rot} needed for the rotation to start is of major interest, because it exhibits a variation of a factor 10 when the Rayleigh number is increased from 2180 to 3000, indicating that the range explored is extremely important and revealing. Indeed, in this range, as already noted, there is a competition between the Rayleigh-Bénard thermal convection and the stabilizing effect of the colloidal particles. This competition leads to the formation of travelling waves patterns, which, in a circular cell, become rotating patterns, due to the confinement determined by the lateral boundary. However, in the regime of subcritical Rayleigh numbers explored by us Rayleigh-Bénard convection prevails, and the stabilizing effect due to the accumulation of the colloid on the bottom of the cell is hampered by the continuous remixing of the particles. Under these conditions, the sedimentation of the particles is slowed down, and so are the appearance of travelling waves and the beginning of the rotation. The time needed for convection to disappear also exhibits a marked dependence on the Rayleigh number, and is in qualitative agreement with the



results of simulations on suspensions of thermophilic nanoparticles with large negative separation ratio heated from below [20].

4 DISCUSSION

Our system is different from most of those that, to our knowledge, have been previously characterized experimentally or theoretically and by means of simulations. In fact, a large number of studies has been devoted to the investigation of water-ethanol mixtures heated from below. Depending on the concentration of ethanol, this system can exhibit a negative separation ratio $\psi > -1$, leading to the oscillatory onset of a convective instability when the fluid is heated from below. Water-ethanol mixtures exhibit a multistable heat transfer at sufficiently small supercritical Rayleigh numbers [3, 5, 6, 8, 11, 12, 14], where depending on the initial condition and on the history of the system the transfer of heat can either occur by conduction or by steady overturning convection, similarly to the bistable behaviour reported by us. The investigation of transient behaviour during the onset of convection shows the development of localized pulses of travelling-wave convection in 1D [9, 23] and 2D geometries [10]. Under supercritical conditions, localized rotating structures develop, and gradually expand until they reach the boundaries of the cell [10, 27]. Conversely, bringing back the system in a subcritical condition after the onset of convection determines the formation of rotating structures that gradually shrink in time until they disappear [13, 34].

All these works deal with binary fluids with a negative separation ratio $-1 < \psi < 0$, a condition where the thermal contribution to the

density variation is larger than the solutal one. At variance, our system is a colloidal suspension of nanoparticles and has a separation ratio $\psi = -3.5$, so that the solutal contribution to the density profile largely dominates the thermal one. Indeed, many of the solutions studied in the cited works are travelling waves that don't die out, whereas the instability that we observed in the end disappears, notwithstanding the fact that the system is under supercritical conditions, due to the stabilization determined by the highly thermophilic particles.

The case of thermal convection in a suspension of thermophilic nanoparticles with a large negative separation ratio $\psi = -10$ has been investigated theoretically by Ryskin and Pleiner [17]. They studied the linear and nonlinear behaviour starting from a suspension with an initially uniform distribution of nanoparticles. They found that at small supercritical Rayleigh numbers $Ra < 1840$ the fluid exhibits a transient oscillatory instability, while at higher Rayleigh numbers the system exhibits bistability, characterized by the presence of a stationary instability and of a stable conductive state. The phenomenology reported is qualitatively very similar to the one reported by us, but the threshold for the transition from a transient oscillatory instability to a stationary one is much larger in our experiments.

Cherepanov and Smorodin have performed a detailed theoretical investigation of the stability of a colloidal suspension heated from below and with negative separation ratio $\psi = -0.8$, taking into account not only the Soret effect but also the effect of sedimentation induced by gravity [21,22]. The sedimentation length l_g becomes in this case an important parameter: for $l_g \ll h$ the colloid gets almost entirely accumulated at the bottom boundary, and the system behaves as a single component fluid. When $l_g \geq h$, the

threshold for Rayleigh-Bénard convection gradually increases to values of the order of several times the threshold for a single component fluid. While the parameters adopted in these studies partially mirror the ones of our sample, the separation ratio $\psi = -0.8$ adopted by Cherepanov and Smorodin corresponds to the condition where the Rayleigh-Bénard convection dominates over the solutal stabilization. By contrast, in the case investigated by us the sedimentation length is moderately high, $l_g/h = 20$, but the strong negative separation ratio $\psi = -3.5$ determines an accumulation of particles at the bottom boundary dominated by the Soret effect and affected only marginally by sedimentation.

Recent experimental studies have outlined the potentiality of the bistability of nanofluids with large negative separation ratio, like the one we studied in this work, to actively control heat transfer by switching between the conductive regime and the convective one (and vice-versa) exploiting the thermophilic behaviour of the nanoparticles [15, 16]. Cherepanov and Smorodin performed 2-dimensional simulations of thermophilic nanofluids with a separation ratio $\psi = -7.5$ heated from below mirroring the one used in these experiments. This study has been able to reproduce accurately the following quantitative aspects observed in experiments performed on a Hyflon MFA suspension of nanoparticles at a concentration of 4.0% w/w [15]: i) The presence of transient and stationary travelling wave regimes separated by a threshold Rayleigh number $Ra^* \approx 3400$; ii) the modifications determined by the presence of nanoparticles on the bifurcation diagram of the Nusselt number as a function of Rayleigh Number; iii) the diagram of the lifetime of travelling waves in the transient regime as a function of Rayleigh number.

REFERENCES

- Lighthill MJ. Waves in Fluids. *Comm Pure Appl Math* (2010) 20:267–93. doi:10.1002/cpa.3160200204
- Carpineti M, Crococo F, Vailati A. Levitation, Oscillations, and Wave Propagation in a Stratified Fluid. *Eur J Phys* (2021) 42:05011. doi:10.1088/1361-6404/ac0fba
- Walden R, Kolodner P, Passner A, Surko CM. Traveling Waves and Chaos in Convection in Binary Fluid Mixtures. *Phys Rev Lett* (1985) 55:496–9. doi:10.1103/physrevlett.55.496
- Kolodner P, Passner A, Surko CM, Walden RW. Onset of Oscillatory Convection in a Binary Fluid Mixture. *Phys Rev Lett* (1986) 56:2621–4. doi:10.1103/physrevlett.56.2621
- Moses E, Fineberg J, Steinberg V. Multistability and Confined Traveling-Wave Patterns in a Convecting Binary Mixture. *Phys Rev A* (1987) 35:2757–60. doi:10.1103/physreva.35.2757
- Heinrichs R, Ahlers G, Cannell DS. Traveling Waves and Spatial Variation in the Convection of a Binary Mixture. *Phys Rev A* (1987) 35:2761–4. doi:10.1103/physreva.35.2761
- Kolodner P, Bensimon D, Surko CM. Traveling-wave Convection in an Annulus. *Phys Rev Lett* (1988) 60:1723–6. doi:10.1103/physrevlett.60.1723
- Niemeela JJ, Ahlers G, Cannell DS. Localized Traveling-Wave States in Binary-Fluid Convection. *Phys Rev Lett* (1990) 64:1365–8. doi:10.1103/physrevlett.64.1365
- Kolodner P, Glazier JA, Williams H. Dispersive Chaos in One-Dimensional Traveling-Wave Convection. *Phys Rev Lett* (1990) 65:1579–82. doi:10.1103/PhysRevLett.65.1579
- Lerman K, Bodenschatz E, Cannell DS, Ahlers G. Transient Localized States in 2d Binary Liquid Convection. *Phys Rev Lett* (1993) 70:3572–5. doi:10.1103/physrevlett.70.3572
- Lerman K, Ahlers G, Cannell DS. Different Convection Dynamics in Mixtures with the Same Separation Ratio. *Phys Rev E* (1996) 53:R2041–R2044. doi:10.1103/physreve.53.r2041
- Porta AL, Surko CM. Dynamics of Two-Dimensional Traveling-Wave Convection Patterns. *Phys Rev E* (1996) 53:5916–34.
- Lerman K, Cannell DS, Ahlers G. Analysis of Transients for Binary Mixture Convection in Cylindrical Geometry. *Phys Rev E* (1999) 59:2975–85. doi:10.1103/physreve.59.2975
- Aegertner CM, Surko CM. Effect of Lateral Boundaries on Traveling-Wave Dynamics in Binary Fluid Convection. *Phys Rev E* (2001) 63:046301.
- Donzelli G, Cerbino R, Vailati A. Bistable Heat Transfer in a Nanofluid. *Phys Rev Lett* (2009) 102:104503. doi:10.1103/physrevlett.102.104503
- Bernardin M, Comitani F, Vailati A. Tunable Heat Transfer with Smart Nanofluids. *Phys Rev E Stat Nonlin Soft Matter Phys* (2012) 85:066321. doi:10.1103/PhysRevE.85.066321
- Ryskin A, Pleiner H. Thermal Convection in Colloidal Suspensions with Negative Separation Ratio. *Phys Rev E Stat Nonlin Soft Matter Phys* (2005) 71:056303. doi:10.1103/PhysRevE.71.056303

Simulations along the same lines of the ones performed by Cherepanov and Smorodin on suspensions of Hyflon MFA nanoparticles should be able to describe effectively the experimental results provided by us in this publication, in particular the bifurcation diagram (Figure 1), and the lifetime of transient convection (Figure 3) in a suspension of Ludox nanoparticles.

DATA AVAILABILITY STATEMENT

The raw data supporting the conclusion of this article will be made available by the authors, without undue reservation.

AUTHOR CONTRIBUTIONS

AV conceived the study and wrote the paper. AP performed measurements. MC and AV coordinated research. All the authors analysed results and contributed to the manuscript.

FUNDING

Work partially supported by the European Space Agency, CORA-MAP TechNES Contract No. 4000128933/19/NL/PG.

ACKNOWLEDGMENTS

We thank M. Allevi, M. Bernardin, R. Cerbino, F. Comitani, and G. Donzelli for early discussion.

18. Shliomis MI, Smorodin BL. Onset of Convection in Colloids Stratified by Gravity. *Phys Rev E Stat Nonlin Soft Matter Phys* (2005) 71:036312. doi:10.1103/PhysRevE.71.036312
19. Smorodin BL, Cherepanov IN, Myznikova BI, Shliomis MI. Traveling-wave Convection in Colloids Stratified by Gravity. *Phys Rev E Stat Nonlin Soft Matter Phys* (2011) 84:026305. doi:10.1103/PhysRevE.84.026305
20. Cherepanov I, Smorodin B. Traveling Waves of a Colloidal Suspension in a Closed Cell. *Eur Phys J E* (2022) 45. doi:10.1140/epjje/s10189-022-00192-4
21. Cherepanov IN, Smorodin BL. Influence of Sedimentation Length on the Convective Stability of a Colloidal Suspension. *J Exp Theor Phys* (2017) 125: 1199–207. doi:10.1134/s1063776117120020
22. Cherepanov IN, Smorodin BL. Convection of strong Stratified Colloidal Suspension. *Microgravity Sci Technol* (2019) 31:517–25. doi:10.1007/s12217-019-09726-6
23. Batiste O, Knobloch E, Alonso A, Mercader I. Spatially Localized Binary-Fluid Convection. *J Fluid Mech* (2006) 560:149–58. doi:10.1017/s0022112006000759
24. Knobloch E. Spatially Localized Structures in Dissipative Systems: Open Problems. *Nonlinearity* (2008) 21:T45–T60. doi:10.1088/0951-7715/21/A/t02
25. Batiste O, Knobloch E. Simulations of Localized States of Stationary Convection in 3he-4he Mixtures. *Phys Rev E* (2005) 95:244501. doi:10.1103/PhysRevLett.95.244501
26. Batiste O, Knobloch E. Simulations of Oscillatory Convection in 3he-4he Mixtures in Moderate Aspect Ratio Containers. *Phys Fluids* (2005) 17:064102. doi:10.1063/1.1920349
27. Mercader I, Alonso A, Batiste O. Spatiotemporal Dynamics Near the Onset of Convection for Binary Mixtures in Cylindrical Containers. *Phys Rev E Stat Nonlin Soft Matter Phys* (2008) 77:036313. doi:10.1103/PhysRevE.77.036313
28. Baaske P, Bataler H, Braibanti M, Carpinetti M, Cerbino R, Crocco F, et al. The NEUF-DIX Space Project - Non-Equilibrium Fluctuations during Diffusion in complex Liquids. *Eur Phys J E* (2016) 39. doi:10.1140/epjje/i2016-16119-1
29. Vailati A, Baaske P, Battaller H, Bolis S, Braibanti M, Carpinetti M, et al. Giant Fluctuations Induced by thermal Diffusion in Complex Liquids. *Microgravity Sci Technol* (2020) 32:873–87. doi:10.1007/s12217-020-09815-x
30. Giavazzi F, Savorana G, Vailati A, Cerbino R. Structure and Dynamics of Concentration Fluctuations in a Non-equilibrium Dense Colloidal Suspension. *Soft Matter* (2016) 12:6588–600. doi:10.1039/c6sm00935b
31. Cerbino R, Vailati A, Giglio M. Soret Driven Convection in a Colloidal Solution Heated from above at Very Large Solutal Rayleigh Number. *Phys Rev E Stat Nonlin Soft Matter Phys* (2002) 66:055301. doi:10.1103/PhysRevE.66.055301
32. Mazzoni S, Giavazzi F, Cerbino R, Giglio M, Vailati A. Mutual Voronoi Tessellation in Spoke Pattern Convection. *Phys Rev Lett* (2008) 100:188104. doi:10.1103/physrevlett.100.188104
33. Giavazzi F, Vailati A. Scaling of the Spatial Power Spectrum of Excitations at the Onset of Solutal Convection in a Nanofluid Far from Equilibrium. *Phys Rev E Stat Nonlin Soft Matter Phys* (2009) 80:015303. doi:10.1103/PhysRevE.80.015303
34. Alonso A, Mercader I, Batiste O. Pattern Selection Near the Onset of Convection in Binary Mixtures in Cylindrical Cells. *Fluid Dyn Res* (2014) 46:1–18. doi:10.1088/0169-5983/46/4/041418

Conflict of Interest: The authors declare that the research was conducted in the absence of any commercial or financial relationships that could be construed as a potential conflict of interest.

Publisher's Note: All claims expressed in this article are solely those of the authors and do not necessarily represent those of their affiliated organizations, or those of the publisher, the editors and the reviewers. Any product that may be evaluated in this article, or claim that may be made by its manufacturer, is not guaranteed or endorsed by the publisher.

Copyright © 2022 Carpinetti, Castellini, Pogliani and Vailati. This is an open-access article distributed under the terms of the Creative Commons Attribution License (CC BY). The use, distribution or reproduction in other forums is permitted, provided the original author(s) and the copyright owner(s) are credited and that the original publication in this journal is cited, in accordance with accepted academic practice. No use, distribution or reproduction is permitted which does not comply with these terms.

RESEARCH ARTICLE | JUNE 23 2023

Dynamics of non-equilibrium concentration fluctuations during free-diffusion in highly stratified solutions of glycerol and water **FREE**

Stefano Castellini ; Marina Carpineti ; Cédric Giraudet ; Fabrizio Croccolo ; Alberto Vailati  

 Check for updates

J. Chem. Phys. 158, 244201 (2023)
<https://doi.org/10.1063/5.0151752>


View
Online


Export
Citation

CrossMark



The Journal of Chemical Physics

Special Topic: Adhesion and Friction

Submit Today!

 AIP
Publishing

Dynamics of non-equilibrium concentration fluctuations during free-diffusion in highly stratified solutions of glycerol and water

Cite as: J. Chem. Phys. 158, 244201 (2023); doi: 10.1063/5.0151752

Submitted: 24 March 2023 • Accepted: 30 May 2023 •

Published Online: 23 June 2023



Stefano Castellini,¹ Marina Carpineti,¹ Cédric Giraudet,² Fabrizio Crococo,² and Alberto Vailati^{1,a)}

AFFILIATIONS

¹ Dipartimento di Fisica "A. Pontremoli," Università degli Studi di Milano, Milano, Italy

² Université de Pau et des Pays de l'Adour, LFCR UMR5150, E2S UPPA, CNRS, TotalEnergies, Anglet, France

^{a)} Author to whom correspondence should be addressed: alberto.vailati@unimi.it

ABSTRACT

We investigate the non-equilibrium fluctuations occurring during free diffusion between two solutions of glycerol and water with various concentration differences. The non-linearity of the system, determined by the strong stratification of the sample, requires introducing an interpretation model able to characterize the dependence of the correlation properties of the non-equilibrium fluctuations on the local thermophysical variables of the system. The proposed model allows us to characterize the dynamics of non-equilibrium fluctuations in the presence of a wide range of relaxation times determined by the strong stratification of the sample, at variance with the cumulant methods commonly used in dynamic light scattering experiments, which work well in the presence of a moderate dispersion of relaxation times.

Published under an exclusive license by AIP Publishing. <https://doi.org/10.1063/5.0151752>

I. INTRODUCTION

A layer of fluid under non-equilibrium conditions exhibits long-range fluctuations.^{1,2} Non-equilibrium conditions can be typically attained by imposing a macroscopic temperature or concentration gradient on the fluid. Non-equilibrium fluctuations (NEFs) arise from the coupling of velocity fluctuations to the macroscopic gradient. When a spontaneous velocity fluctuation determined by the thermal agitation of the fluid displaces a parcel of fluid, it generates a local vortex and, in turn, a local variation of the density, which is not the case under equilibrium conditions. The mean squared amplitude of the fluctuations diverges as $1/q^4$ at small wave numbers q , a feature that was first predicted theoretically³⁻⁵ and then verified experimentally.¹⁰⁻¹⁶ The divergence of the mean squared amplitude of fluctuations is inhibited by the gravity force.^{14,17,18} In fact, if the region of the fluid affected by the velocity fluctuation is large enough, buoyancy brings it back to the layer of fluid with the same density that originated the fluctuation before its dissolution by diffusion. Experiments performed in the absence of gravity have shown that in this case, the divergence of fluctuations is inhibited only by the finite physical size of the fluid.¹⁹⁻²¹ The experiments performed in space in the framework of the GRADFLEX project of the European

Space Agency (ESA) and National Aeronautics and Space Administration (NASA) have provided convincing evidence that linearized hydrodynamics achieves an accurate quantitative modeling of the static and dynamic properties of the fluctuations under ideal non-equilibrium conditions,¹⁹⁻²¹ such as steady state diffusion processes driven by small macroscopic density gradients.¹

The theoretical modeling of non-equilibrium fluctuations determined by transient diffusion processes in the presence of large density gradients is made difficult by the fact that under these conditions, an analytic description of the static and dynamic statistical properties of the fluctuations is not possible. However, the investigation of non-equilibrium fluctuations under these non-ideal conditions is highly desirable because most natural and technological diffusion processes occur under non-ideal transient conditions in the presence of large gradients. Theoretical advances in this direction have recently been obtained by investigating the role of giant fluctuations in turbulent flows at high Schmidt number at sub-Kolmogorov scales, with the aim of understanding whether thermal noise significantly affects the turbulent flow, as it was originally predicted in the 1960s by Bechov.²² Indeed, the outcome of recent studies is that the dissipation regime of the turbulent flow is strongly affected by thermal noise. The exact modeling of non-

ear advection of concentration fluctuations obtained by applying the methods from the Kraichnan model of turbulent advection showed that the static and dynamic structure functions reproduce exactly those obtained from linearized hydrodynamics.²³ As far as simulations of non-equilibrium fluctuations are concerned, traditional computational methods can hardly be applied to this kind of problem due to the presence of a range of length scales and timescales spanning several orders of magnitude. During the last 15 years, the solution to this challenging problem has come through the development of staggered schemes based on fluctuating hydrodynamics.²⁴ Very recently, these methods have also been extended to non-isothermal systems, thus allowing the computational investigation of non-equilibrium fluctuations driven by the Soret and Dufour effects.²⁵

Beyond nonlinear theoretical modeling, a quantitative characterization of non-equilibrium fluctuations under non-ideal conditions can be achieved by means of experiments and simulations. In this context, the Giant Fluctuations and TechNES projects of ESA will investigate the non-equilibrium fluctuations occurring in complex fluids during diffusion processes under microgravity conditions.^{26,27} These projects will typically investigate transient and stationary processes in multi-component fluids, whose stability on Earth is impaired by the presence of double diffusion processes that lead to the onset of convective motions even in the presence of an initially stable density profile.

Since the thermophysical properties of a fluid mixture depend on its concentration, the presence of a strong stratification gives rise to non-linear terms in the diffusion equation and, thus, to a superposition of modes with different amplitudes and relaxation times arising from different layers of fluid at any wave number. Non-equilibrium fluctuations are typically investigated by using static and dynamic light scattering techniques, including newly developed near-field techniques²⁸ such as near-field scattering,²⁹ dynamic shadowgraphy,³⁰ and differential dynamic microscopy.³¹ All these optical methods work by illuminating the sample with a beam of light and collecting, on a matrix sensor, the light scattered by the sample. As a result, the light collected by the sensor is the superposition of the contributions of the light scattered by different layers of the sample, which can be characterized by different thermophysical properties depending on the local concentration. In the presence of a small concentration gradient, the dependence of thermophysical properties on concentration can be neglected, while for larger gradients, the analysis of the signal requires a non-trivial modeling of the properties of the stratified fluid. As a first approximation, the contributions arising from the different layers can be assumed to be uncorrelated, and the modeling of the scattered intensity can be obtained by integrating the intensity of the scattered light across the sample thickness.³² This approximation is expected to hold when the wave numbers are significantly larger than the finite-size wave number $q_{\beta} = 2\pi/h$ associated with the finite thickness h of the sample, even in the presence of a significant dependence of the thermophysical properties on the temperature or the concentration.³³ More generally, non-equilibrium fluctuations are expected to be correlated also in the direction parallel to the gradient,³⁴ the correlation length being of the order of $1/q$. Therefore, a proper modeling of the light scattered at small wave numbers would require to take these long-range correlations into account.

Recently, Zapf *et al.*³³ have performed a thorough experimental investigation of the effect of non-linearities of the concentration gradient on non-equilibrium fluctuations induced by thermal diffusion in a polymer solution. Under the experimental conditions adopted by them, a temperature gradient imposed on the sample determines the formation of a concentration gradient through the Soret effect, leading to a stratification of the sample both in temperature and concentration. Taking into account the temperature and concentration dependence of the transport coefficients, the authors have shown that in the presence of temperature differences $\Delta T > 1/S_T$, the concentration profile exhibits marked non-linearity, where S_T is the Soret coefficient. The authors used dynamic shadowgraphy to characterize the relaxation of temperature and concentration non-equilibrium fluctuations under steady state conditions. The interpolation of the correlation functions was performed by assuming a simple bimodal exponential relaxation, where one exponential characterizes the decay of temperature fluctuations, and the other one characterizes the decay of concentration fluctuations. This method allows us to determine the average thermal diffusivity and diffusion coefficient (but not their dispersion) and to check whether they correspond to the reference values evaluated at the average temperature and concentration. The outcome of this analysis is that in the presence of strong non-linearity in the concentration gradient, the diffusion and Soret coefficients differ significantly from the reference values at the average concentration. Therefore, the analysis of experimental results requires a computational evaluation of the contributions of the different layers of fluid.

In this work, we investigate non-equilibrium concentration fluctuations during transient diffusion in mixtures of water and glycerol subjected to strong concentration gradients. Experiments are performed in an isothermal free-diffusion configuration, where two solutions of water and glycerol with different concentrations are initially brought into contact in the stable configuration, where the denser mixture lies at the bottom of the sample cell.³⁵ To perform these experiments, we take advantage of a unique three-dimensional flowing junction cell that is able to generate an interface between the two mixing phases free of spurious disturbances.³⁶ The strong dependence of the viscosity and diffusion coefficient of the mixture on the concentration of glycerol determines a highly non-linear concentration profile, which in turn determines a wide range of relaxation times of the non-equilibrium concentration fluctuations at any wave number, leading to a non-exponential relaxation of the time correlation function at a fixed wave number.³⁰ We develop an empirical model for the time correlation function of the scattered light, and we find that the assumption of uniformly distributed relaxation times provides a quantitatively accurate description of the deviation from a Single Exponential (SE) relaxation of the correlation function. Under these conditions, the dynamics of the system at each wave number can be completely described in terms of the fastest and slowest relaxation times of the system. We discuss this result in comparison with the traditional particle sizing methods commonly used in dynamic light scattering to characterize the dispersion of relaxation times in polydisperse samples, such as cumulant analysis³⁷ and the Schulz distribution.³⁸

This article is organized as follows: first, the theory of non-equilibrium fluctuations is presented, both for an ideal thin sample, for which the concentration gradient is uniform, and for a non-ideal thick stratified sample. Then, we develop an interpretative model

for the latter case, which is compared with numerical calculations, with the ideal model for a thin sample, and with the model based on the Schulz distribution. After explaining the theory in detail, we discuss results and we show that our proposed model provides a more accurate fitting of experimental results when compared to the other models discussed. Finally, we extract from the analysis of the experimental results the thermophysical coefficients describing the state of the sample and compare them with reference ones.

II. THEORY

The non-equilibrium mass flow induced by the presence of a macroscopic concentration gradient generates concentration fluctuations δc , whose amplitude is orders of magnitude larger than that of equilibrium fluctuations. A suitable theoretical modeling of these fluctuations under ideal conditions of small macroscopic concentration gradients has been achieved by using fluctuating hydrodynamics,³⁹ where the equations of hydrodynamics for a fluid at rest are linearized with respect to small perturbations of the hydrodynamic variables.^{1,6} Fluctuating hydrodynamics allows us to recover both the static and dynamic correlation properties of the fluctuations, which are accessible experimentally by performing light scattering experiments.²⁷ Most theoretical studies involve the investigation of systems under stationary non-equilibrium conditions, but it has been shown that the theoretical investigation of transient diffusion is made possible by the introduction of an adiabatic approximation into the hydrodynamic equations, which allows us to linearize them to obtain expressions for the static and dynamic correlation properties compatible with those for a system at the steady state.³²

A. Uniform concentration gradient

1. Static structure factor

Quite generally, we consider a layer of a binary mixture, characterized by a concentration c , a mass diffusion coefficient $D(c)$, and a kinematic viscosity $\nu(c)$. The layer is under the action of a vertical stabilizing concentration gradient ∇c , and we assume that the gradient is uniform across it. This is typically the case with a thin layer of fluid. Under these hypotheses, it can be shown that the static structure factor $\hat{S}(q)$ of the non-equilibrium concentration fluctuations is³²

$$\hat{S}(q) = S_{eq} \left[1 + \left(\frac{\nabla c}{\nabla c_{grav}} - 1 \right) \frac{1}{1 + \left(\frac{q}{q_{ro}} \right)^4} \right], \quad (1)$$

where the \sim sign over $\hat{S}(q)$ stands for the property in a layer of fluid with a uniform concentration gradient, and q_{ro} is the characteristic roll-off wave number below which the relaxation of fluctuations determined by buoyancy is faster than that determined by diffusion,

$$q_{ro}(c) = \left(\frac{\beta \mathbf{g} \cdot \nabla c}{\nu(c)D(c)} \right)^{1/4}, \quad (2)$$

where $\beta = (1/\rho)(\partial\rho/\partial c)$ is the solutal expansion coefficient, ρ is the density of the mixture, and \mathbf{g} is the gravitational acceleration;

$$\nabla c_{grav} = \beta \mathbf{g} \left(\frac{\partial c}{\partial \mu} \right)_{p,T} \quad (3)$$

represents the equilibrium concentration gradient induced by barodiffusion, and

$$S_{eq} = \frac{k_B T}{16\pi^3 \rho} \left(\frac{\partial c}{\partial \mu} \right)_{p,T} \quad (4)$$

is the q -independent static structure factor of equilibrium fluctuations, where T is the temperature of the isothermal sample, k_B is the Boltzmann constant, and $(\partial c/\partial \mu)_{p,T}$ is the osmotic compressibility. Equation (1) holds under the assumption of a large Schmidt number $Sc = \nu(c)/D(c) \gg 1$ and under the assumption that $(q_{ro}/q)^4 \ll Sc$. As far as the first assumption is concerned, for the glycerol–water mixtures under investigation in this work, the typical range of the mass diffusion coefficient is⁴⁰ $(1.02 \times 10^{-5} - 1.54 \times 10^{-7})$ cm²/s, while the range of the kinematic viscosity is⁴¹ $(0.009 - 1.29)$ cm²/s, and consequently, the large Schmidt number assumption holds in the explored concentration range. Due to the large Schmidt number, the second assumption also holds in the range of wave numbers explored by us, with the exception of very small wave numbers $q \ll q_{ro}$, where the strong gravitational stabilization can give rise to propagating modes.⁴²

2. Dynamic structure factor

The Onsager regression hypothesis and linearized hydrodynamics allow us to determine the dynamic properties of non-equilibrium fluctuations in a thin layer of fluid. A statistical characterization of these properties can be achieved through the time autocorrelation function of the fluctuations as follows:¹

$$\hat{S}(q, \Delta t) = \hat{S}(q) \cdot \exp(-\gamma \Delta t), \quad (5)$$

where the relaxation rate $\gamma = 1/\tau_c(q)$ is the reciprocal of the decay time of the fluctuations,

$$\gamma(q) = D(c)q^2 \cdot \left(1 + \left(\frac{q_{ro}(c)}{q} \right)^4 \right), \quad (6)$$

The relaxation rate exhibits a power-law dependence on q at small and large wave numbers.³² At large wave numbers, $\gamma(q) \approx D(c)q^2$, and the relaxation of fluctuations occurs diffusively. At small wave numbers, $\gamma(q) \approx D(c)q_{ro}^4/q^2$, and the relaxation process is governed by buoyancy, which determines a restoring force that brings back the fluctuations in the layer with the same density that originated them. The crossover between these two regimes occurs at the roll-off wave number q_{ro} , which represents the slowest mode of relaxation.⁴³ In a thin layer of fluid, the variation of $D(c)$ and q_{ro} , associated with the presence of the concentration gradient is small, and these two parameters can be assumed to be constant, while in the presence of a strongly stratified sample, like that dealt with in the present work, their dependence on concentration cannot be neglected, and the decay time of the fluctuations at a certain wave number becomes strongly dependent on concentration.

B. Stratified mixture with non-linear concentration profile

Having set out the expressions for $\hat{S}(q)$ and $\hat{S}(q, \Delta t)$ for a thin layer of a binary mixture with a uniform concentration gradient, we can now model the case of a strongly stratified sample

as a superposition of thin layers of fluid with different concentration gradients. The first aim is the numerical characterization of the macroscopic gradient and concentration profiles of the sample along the z -coordinate, which will allow us to calculate expressions for the static and dynamic structure factors of the stratified sample and to compare them with the experimental data.

1. Macroscopic state

In this section, our aim is to characterize quantitatively the time evolution of the macroscopic concentration profile $c(z, t)$ of a solution undergoing a free-diffusion process when two horizontal layers of a binary liquid mixture at different concentrations are brought into contact at time $t_0 = 0$. In the gravitationally stable configuration where the denser phase is layered at the bottom of the lighter one, the mixing occurs through a diffusive process.

To obtain quantitative information about the concentration profile $c(z, t)$ and the gradient profile $\nabla c(z, t)$ we can formalize the problem using the one-dimensional diffusion equation for the concentration since the process is uniform in the x and y directions. In the presence of a dependence of the diffusion coefficient on concentration, the non-linear diffusion equation can be written as

$$\frac{\partial c}{\partial t} = \frac{\partial}{\partial z} \left(D(c) \cdot \frac{\partial c}{\partial z} \right). \quad (7)$$

To solve this equation, we need to explicit the dependence of $D(c)$ on c and define the initial and boundary conditions. In the case of $D(c)$, we have used a polynomial law that accurately describes the concentration dependence in a glycerol–water mixture of interest in this paper as follows:⁴⁰

$$D(c) = (10.25 - 13.08 \cdot c + 8.62 \cdot c^2 - 17.65 \cdot c^3 + 11.98 \cdot c^4) \cdot 10^{-06} \text{ cm}^2/\text{s}. \quad (8)$$

In the case of a free-diffusion process, the initial condition is a step function:

$$c(z, t_0) = \begin{cases} c_1, & z \in \left(0, \frac{h}{2}\right), \\ c_2, & z \in \left(\frac{h}{2}, h\right), \end{cases} \quad (9)$$

where $t_0 = 0$ is the initial time and h is the thickness of the two superimposed layers. To finish setting up the problem, we need to specify the boundary conditions. In our case, the walls of the sample are impermeable to the mass flow, which results in the following condition:

$$\frac{\partial c}{\partial z} = 0|_{z=0,h}. \quad (10)$$

To obtain the time evolution of the concentration profile during the diffusion process, we used the MatLab PDE solver to solve numerically Eq. (7) with the initial and boundary conditions specified by Eqs. (9) and (10), respectively. In the case of an extremely large initial gradient (95% glycerol against pure water), the concentration and gradient profiles develop a strong asymmetry during their time evolution, determined by the non-linearity of Eq. (7) [Figs. 1(a) and 1(c)].

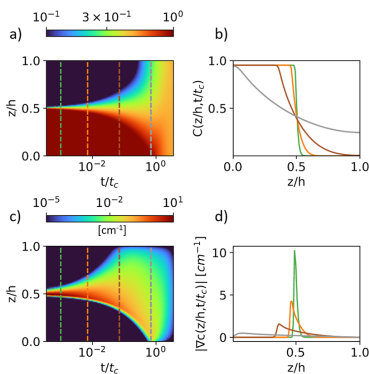


FIG. 1. Time evolution of concentration $c(z, t)$ and gradient $|\nabla c|$ profiles with initial conditions: $c_1 = 95\%$ and $c_2 = 0\%$. (a) $c(z, t)$ represented by a color map ranging from blue (low concentration) to red (high concentration). The color scheme (top color bar) is on a logarithmic scale; the time is normalized to $t_c = 3.16 \times 10^3$ s, while the z -coordinate is normalized to the height of the sample h . (b) Vertical sections of (a) at four different times $t/t_c = 10^{-3}$ (green); 7×10^{-3} (orange); 7×10^{-2} (burgundy); and 7×10^{-1} (gray), marked in panel (a) with the same color scheme. (c) $|\nabla c|$ corresponding to the concentration profile plotted in (a) (same horizontal and vertical axes). The color map (top color bar) is logarithmic. (d) Vertical sections of (c) at the same times marked in panel (a) with the same color scheme.

This result is remarkably different from the one that can be calculated in the presence of small gradients, where the diffusion equation is solved assuming that $D(c)$ is constant. In this last case, Eq. (7) would have reduced to Fick's second law, $\partial c/\partial t = D(\partial^2 c/\partial z^2)$, and would present symmetry around the position of the interface $z/h = 1/2$ at any time. Instead, in our case, one can clearly see that while for small times, the concentration and the gradient profiles actually show symmetry along the z -coordinate, as the evolution of the macroscopic state advances, this symmetry is lost.

After a time larger than the mean diffusive time t_c , defined by

$$t_c = \frac{h^2}{\langle D(c) \rangle \pi^2}, \quad (11)$$

the system reaches an equilibrium state, characterized by a uniform concentration profile. From Fig. 1, one can also appreciate how, as time passes, the thickness of the region involved in diffusive remixing grows until it affects the whole sample. This modeling of the macroscopic state is fundamental to describe the case of a strongly stratified sample and to interpret the results.

2. Static stratified structure factor

Experiments on non-equilibrium fluctuations are usually performed by means of light scattering or shadowgraphy, in a configuration where a beam of light crosses the sample parallel to the concentration gradient. In this configuration, the light impinging on the detector is the superposition of the light scattered by the layers of fluid inside the stratified sample.

The evaluation of the static structure factor of the thick layer of a strongly stratified fluid can be achieved by combining the results of Secs. II A 1 and II B 1 and adding up the contributions to the static power spectrum determined by the different layers, which are characterized by different thermophysical properties. For this reason, it is useful to define a structure factor averaged across the thickness of the sample because this quantity can be easily compared to experimental results. An expression for the average structure factor can be obtained by integrating $\tilde{S}(q)$ across the sample thickness. Assuming that our system is far from equilibrium, so that $S_{eq} \ll S(q)$ and $\nabla c_{grav} \ll \nabla c$, the static stratified structure factor is defined by the relation

$$S(q) = \int_0^h \frac{dz}{h} \tilde{S}(q) = \int_0^h \frac{dz}{h} \frac{S_{eq}}{\nabla c_{grav}} \left[\frac{\nabla c}{1 + \left(\frac{q}{q_0}\right)^4} \right]. \quad (12)$$

The ratio $S_{eq}/\nabla c_{grav}$ is constant along the z -coordinate, so that it is possible to numerically integrate the static structure factor obtaining the result shown in Fig. 2, where we have also highlighted how the different layers contribute to the final result.

One can clearly see that $\tilde{S}(q)$ integrated over the whole sample thickness (black data points) presents a very similar trend when it is integrated over the central thin layers only (purple data points), which provide the largest contributions to the average. For this reason, the shape of the stratified static structure factor is not particularly affected by the contributions of the different layers, and a suitable model for the interpolation of the stratified structure factor is

$$\frac{S(q)}{S(0)} = \frac{1}{1 + \left(\frac{q}{q_0}\right)^4}, \quad (13)$$

which allows us to estimate the effective roll-off wave number determined by the stratification.

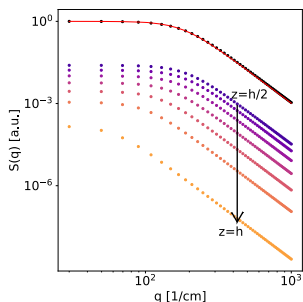


FIG. 2. Numerically calculated static structure factor $\tilde{S}(q)$ as a function of wave number q for initial conditions $c_1 = 95\%$ and $c_2 = 0\%$ and at diffusion time $t/t_c = 0.07$ (~350 min after the start of evolution). Different colors represent $\tilde{S}(q)$ at different z -coordinates (as indicated by the arrow). The black data are the integral of $\tilde{S}(q)$ layer by layer, over z , Eq. (12), the red solid line is the fit with the model of Eq. (13).

As a word of caution, we notice that when we have written Eq. (12), we have assumed that each layer provides an independent contribution to the integrated structure factor, which implies that non-equilibrium fluctuations are not correlated in the direction of the macroscopic gradient, which in this case is the vertical direction. This is not true in general, as it can be shown that the non-equilibrium fluctuations are indeed also correlated in the vertical direction, with a correlation length very similar to that in the direction orthogonal to the concentration gradient.³⁴ However, when the condition $q \gg 2\pi/h$ holds, one can assume that the correlation between contributions to the integrated structure factor determined by different layers is negligible.³³ For the results shown in Fig. 2, the largest wave number is 50 cm^{-1} , which is much larger than $2\pi/h \approx 6 \text{ cm}^{-1}$ associated with the finite size of the sample.

3. Dynamic stratified structure factor

In order to derive an expression for the dynamic stratified structure factor $S(q, \Delta t)$, we can average contributions coming from different layers with an approach similar to that adopted for the static stratified structure factor. In the dynamic case, the stratification of the sample determines a dispersion of the relaxation rate of non-equilibrium fluctuations at a fixed wave number q due to the dependence on the concentration of the diffusion coefficient and the roll-off wave number in Eq. (6).

For this reason, it is convenient to use the relaxation rate γ as a suitable integration variable for the stratified structure factor rather than the z coordinate,

$$S(q, \Delta t) = S(q) \cdot \int_{\gamma_m}^{\gamma_M} G(\gamma) \exp(-\gamma \Delta t) d\gamma, \quad (14)$$

where $G(\gamma)$ is the probability density function of decay rates γ within the sample, while γ_m and γ_M are the minimum and maximum decay rates within the sample, respectively.

We can then write the dynamic stratified structure factor in the form $S(q, \Delta t) = S(q) \cdot g(q, \Delta t)$, where we have defined the stratified correlation function as follows:

$$g(q, \Delta t) = \int_{\gamma_m}^{\gamma_M} G(\gamma) \exp(-\gamma \Delta t) d\gamma. \quad (15)$$

Physically, this function results from the superposition of all $\tilde{S}(q, \Delta t)$ describing the correlation dynamics of NEFs occurring at different layers and consequently at different relaxation rates γ . To find a model representing $g(q, \Delta t)$, it is necessary to identify the function $G(\gamma)$ that provides an adequate description of the experimental results. In the following, we will adopt a Uniform Distribution (UD) model, where we assume that $G(\gamma)$ is uniformly distributed between a minimum γ_m and maximum γ_M relaxation rate. Due to the discussion made in the section on the macroscopic state, the assumption of a uniform distribution is not strictly compatible with the asymmetry of the concentration profiles; however, this simple approximation provides a remarkably better agreement between the theoretical and experimental time correlation functions, much better than the one that can be achieved with the thin-layer model where the concentration gradient is uniform, Eq. (5).

The integration of Eq. (15) with the UD model allows us to find an analytic expression for the stratified correlation function $g(q, \Delta t)$ as follows:

$$g(q, \Delta t) = \frac{-e^{-\gamma_M \Delta t} + e^{-\gamma_m \Delta t}}{\Delta t (\gamma_M - \gamma_m)} \\ = \exp(-\Gamma \Delta t) \cdot \frac{\sinh(\sigma \Delta t)}{\sigma \Delta t}, \quad (16)$$

where

$$\Gamma = \frac{\gamma_M + \gamma_m}{2}, \quad (17)$$

$$\sigma = \frac{\gamma_M - \gamma_m}{2}. \quad (18)$$

The form of Eq. (16) is particularly appealing because the correlation function is written in terms of a single exponential relaxation multiplied by a hyperbolic sine cardinal function that characterizes the presence of a dispersion of relaxation times. With this form, it is apparent that for $\sigma \sim 0$, we return to the ideal single exponential relaxation for a thin layer of Eq. (5), where non-equilibrium fluctuations relax with a single characteristic time.

To extract quantitative parameters characterizing the sample, it is necessary to investigate the theoretical dependence of Γ and σ on q . For the thin-layer case, the two parameters that determine the quantitative dependence of γ on q are the diffusion coefficient D and the roll-off wave number q_{ro} [Eq. (6)]. For the thick sample case, the new variables $\Gamma(q)$ and $\sigma(q)$ are linear combinations of the decay rates $\gamma_m(q)$ and $\gamma_M(q)$, which have the same dependence on q as the thin layer, Eq. (6). Therefore, a linear combination of these rates does not change the dependence on q . By combining Eqs. (17) and (18) with Eq. (6), it is possible to determine the dependence of Γ and σ on q as follows:

$$\Gamma(q) = \left(\frac{D_M + D_m}{2} \right) q^2 \cdot \left[1 + \frac{D_M \cdot q_M^4 + D_m \cdot q_m^4}{(D_M + D_m) \cdot q^4} \right], \quad (19)$$

$$\sigma(q) = \left(\frac{D_M - D_m}{2} \right) q^2 \cdot \left[1 + \frac{D_M \cdot q_M^4 - D_m \cdot q_m^4}{(D_M - D_m) \cdot q^4} \right], \quad (20)$$

where D_M and q_M are the diffusion coefficient and roll-off wave number of the thin layer with the maximum decay rate γ_M , while

D_m and q_m are those for the layer with the minimum decay rate γ_m . It is possible to simplify the notation by introducing the parameters

$$D_\Gamma = \left(\frac{D_M + D_m}{2} \right), \quad (21)$$

$$q_\Gamma^4 = \frac{D_M \cdot q_M^4 + D_m \cdot q_m^4}{(D_M + D_m)}, \quad (22)$$

$$D_\sigma = \left(\frac{D_M - D_m}{2} \right), \quad (23)$$

$$q_\sigma^4 = \frac{D_M \cdot q_M^4 - D_m \cdot q_m^4}{(D_M - D_m)} \quad (24)$$

so that Eq. (20) becomes

$$\Gamma(q) = D_\Gamma q^2 \cdot \left(1 + \left(\frac{q_\Gamma}{q} \right)^4 \right), \quad (25)$$

$$\sigma(q) = D_\sigma q^2 \cdot \left(1 + \left(\frac{q_\sigma}{q} \right)^4 \right). \quad (26)$$

D_Γ and D_σ represent, respectively, the mean value and the width of the distribution of the true diffusion coefficients present in the stratified sample, Eq. (8), as confirmed by both numerical calculations (Fig. 3) and experimental data (Fig. 9). The wave number q_Γ represents an average of the two wave numbers q_m and q_M , weighted by the smallest and largest diffusion coefficients of the systems D_m and D_M , while q_σ is analogously related to the wave numbers difference.

Figure 3 shows the trends of $\Gamma(q)$ and $\sigma(q)$, calculated by fitting the numerically generated data of dynamic stratified structure factor, Eq. (14) with the model of Eq. (16). The results of the fit are shown at three different initial concentrations; the different panels represent data calculated numerically at the instants $t/t_c = 0.07$, $t/t_c = 0.7$, and $t/t_c = 2$.

For large concentration differences between the two initial mixtures (green symbols) and small times $t/t_c < 1$ the values of σ (triangles) are perfectly superimposed on those of Γ (circles) (left and center panels of Fig. 3). This means that for each q , the

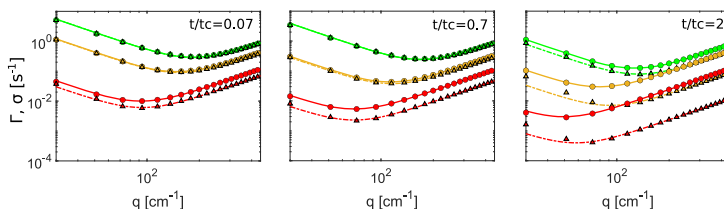


FIG. 3. Numerically calculated mean relaxation rate plotted as a function of q of the Γ (circles) and of its dispersion σ (triangles). Data are evaluated at the instants $t/t_c = 0.07$ (left) as in Figs. 2 and 4, $t/t_c = 0.7$ (center) and $t/t_c = 2$ (right). The different colors represent different initial conditions: $c_1 = 95\%$ and $c_2 = 80\%$ (red); $c_1 = 95\%$ and $c_2 = 40\%$ (orange); and $c_1 = 95\%$ and $c_2 = 0\%$ (green). The solid lines are the fit of $\Gamma(q)$ with Eq. (25), while the dashed lines are the fit of $\sigma(q)$ with Eq. (26).

dispersion of $G(\gamma)$ is so large that it is comparable to the mean value Γ . As the difference between the initial concentration conditions decreases (orange and red data), the difference between Γ and σ increases. This becomes particularly evident for $c_1 = 95\%$ and $c_2 = 80\%$ (red symbols) (center and right panel of Fig. 3), where the mean value of Γ relaxation rates is lower than in the green case and where σ dispersion (red triangles) is distinctly lower than Γ (red circles).

In order to compare the dispersion of samples with different initial concentration conditions in a quantitative way, a significant dimensionless parameter is the stratification index,

$$SI \equiv \frac{D\sigma}{D\Gamma}. \quad (27)$$

The values of the stratification index extracted from the data shown in the left panel of Fig. 3 are $SI_{95\%0\%} = 0.96$, $SI_{95\%40\%} = 0.90$, and $SI_{95\%80\%} = 0.66$. The stratification index can also be determined using the reference values of the diffusion coefficient calculated via Eq. (8), leading to $SI_{95\%0\%}^{ref} = 0.96$, $SI_{95\%40\%}^{ref} = 0.90$, and $SI_{95\%80\%}^{ref} = 0.67$, in complete agreement with the values evaluated from the data in the left panel of Fig. 3.

4. Cumulant methods and Schulz distribution

Several methods have been devised to characterize the distribution of relaxation times in dynamic light scattering experiments from the time correlation function of the scattered light. Cumulant methods work well only in the presence of a moderate dispersion of relaxation times with respect to an underlying monomodal distribution, starting from a nearly exponential time correlation function. Conversely, the CONTIN method developed by Provencher⁴⁴ is a powerful method based on the inverse Laplace transform that allows us to characterize systems that exhibit a multimodal distribution of decay times, and, in general, to determine the distribution of relaxation times starting from a correlation function that can differ significantly from a single exponential relaxation. CONTIN also exhibits some well-known limitations arising from the ill-posed mathematical nature of the inversion problem, which makes it sensitive to noise, and a small change in the experimental data can lead to a large change in the distribution of relaxation times.⁴⁵ In our work, the aim is to determine the deviations of the time correlation function from a purely exponential relaxation using dynamic shadowgraphy, which relies on the determination of correlation functions at thousands of different wavenumbers by using the Compute Unified Device Architecture (CUDA) platform and programming interface for the parallel processing of sequences of thousands of shadowgraph images.^{46,47} This method is intrinsically different from the one adopted in a traditional light scattering setup, where the time correlation function is determined at a single wave vector. The thousands of correlations functions obtained with our dynamic shadowgraphy method need to be fitted automatically, and this requires a reliable fitting model not affected much by the presence of noise in the data. For these reasons, our choice was to rely on a method that allows us to achieve a robust characterization of the distribution of decay times through the determination of the average decay time and its variance through an analytic empirical modeling of the correlation function. This kind of conceptual approach bears several similarities with the cumulant methods, and with the Schulz model, which are

frequent choices for the analysis of dynamic light scattering results in several different fields due to their effectiveness and reliability. For these reasons, in the following we will focus the discussion of the method proposed by us in comparison to cumulant methods and the Schulz model. The cumulant methods rely on the fact that for a reasonably narrow distribution of the decay rates $G(\gamma)$ and for a reasonable range of the normalized delay time $\gamma\Delta t$, it is possible to write the time autocorrelation function as a product of a purely exponential term representative of the dynamics of a monodisperse system of particles with a polynomial in the delay time^{48,49}

$$g(q, \Delta t) = \exp(-\Gamma\Delta t) \cdot \left(1 + \frac{1}{2}\mu_2\Delta t^2 - \frac{1}{3!}\mu_3\Delta t^3 + \dots\right), \quad (28)$$

where the coefficients $\mu_2, \mu_3, \mu_4, \dots$ allow characterizing the dispersion of relaxation times and, in turn, the size polydispersity of the system. An analytical expression for the time correlation function equivalent to the cumulant expansion of Eq. (28) can be found by assuming that the decay rates follow a Schulz distribution,

$$G(\gamma) = \frac{1}{\Gamma} \frac{(1/\sigma_n^2)^{1/\sigma_n}}{(1/\sigma_n - 1)!} \left(\frac{\gamma}{\Gamma}\right)^{1/\sigma_n - 1} \exp\left(-\frac{\gamma}{\Gamma\sigma_n}\right), \quad (29)$$

where Γ is the mean value and σ_n is the normalized standard deviation of the distribution. Combining Eqs. (15) and (29), the expression for the correlation function is

$$g(q, \Delta t) = (1 + \sigma_n^2\Gamma\Delta t)^{-1/\sigma_n^2}. \quad (30)$$

A comparison between this correlation function and that obtained for the UD model can be achieved by comparing Eq. (28) with that obtained from a Taylor expansion of the hyperbolic sine cardinal function of the UD model, Eq. (16), as follows:

$$g(q, \Delta t) = \exp(-\Gamma\Delta t) \cdot \left(1 + \frac{\sigma^2}{3!}\Delta t^2 + \frac{\sigma^4}{5!}\Delta t^4 + \dots\right). \quad (31)$$

The comparison between the two expansions shows that in the case of the UD model, the first three terms are of even degree, while in the case of the expansion obtained from the Schulz distribution, a term of degree three is present. In general, the cumulant method is known to be effective in the presence of a relatively narrow distribution with $\sigma_n \leq 0.6$.³⁸ In the case of the free-diffusion experiments described in this paper, the dispersion can largely exceed this value. For example, in the case of the most extreme initial conditions ($c_1 = 0$ and $c_2 = 0.95$) found in our experiments, $\sigma_n \sim 1$. Moreover, numerical calculations performed by us under these conditions show that the distribution $G(\Gamma)$ is substantially flat. For this reason, in this work we adopted a uniform distribution of relaxation times, which gives rise to a time autocorrelation conceptually simpler than that obtained with the Schulz distribution, Eq. (29), due to the fact that when $\sigma_n = 0$, one immediately recovers a purely exponential relaxation.

To compare the effectiveness of the correlation function obtained with the UD model of Eq. (16) and that obtained from the Schulz model of Eq. (30), we checked which one best interpolates the correlation function data generated numerically. These data are calculated by integrating Eq. (15) on the non-linear macroscopic

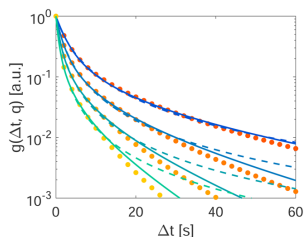


FIG. 4. Numerically calculated stratified correlation functions $g(q, \Delta t)$ (circles) as a function of delay time Δt for a sample with $c_1 = 95\%$ and $c_2 = 0\%$, at a diffusion time $t/t_c = 0.07$ (as in Figs. 3 and 7). Results are shown for different wave numbers $q = 285, 390, 495,$ and 600 cm^{-1} , with colors ranging from red (lowest q) to yellow (highest q). The data are fitted with the uniform model Eq. (16) (solid lines) and with the Schulz model Eq. (30) (dashed lines).

state discussed in Sec. II B 1, so as to take into account the actual distribution of the relaxation times inside the sample.

We plot in Fig. 4 the correlation function $g(q, \Delta t)$ calculated at four wave-numbers by integrating Eq. (15) across the non-linear concentration profile shown in Fig. 1. The semilogarithmic scale emphasizes that $g(q, \Delta t)$ is, in general, not a simple exponential as in the thin layer case, which would result in a straight line. The data are, therefore, fitted with the approximated model proposed in Eq. (16) (solid lines) and with the Schulz function of Eq. (30) (dashed lines).

It can be noticed that, for the extreme conditions considered, the interpolation obtained with the Schulz function presents large deviations from the numerically calculated data as Δt and q increase, while the fit with the model of Eq. (16) is in good agreement with the numerically calculated data for wave numbers $285 < q < 600 \text{ cm}^{-1}$ and delay times $0 < \Delta t < 60 \text{ s}$, up to values of the correlation function of the order of 0.01. Although outside these limits it might be necessary to find a less stringent approximation for $G(\gamma)$, the results shown in Fig. 4 demonstrate that in the presence of a large dispersion of decay times ($St^{diff} = 0.96$), the UD correlation

function introduced in Eq. (16) is more effective than the Schulz function, Eq. (30), in describing the numerically calculated dynamics of non-equilibrium fluctuations in a strongly stratified system.

III. EXPERIMENTAL METHODS

A. Setup

Performing the free-diffusion experiments discussed in this work requires bringing into contact a mixture of glycerol and water at a weight fraction concentration c_1 with a mixture at concentration c_2 under controlled conditions that avoid the generation of spurious disturbances. Gravity stabilizes the system because the latter is prepared in the configuration where the bottom layer of fluid has the highest concentration ($c_1 > c_2$) and density. We performed experiments on different couples of glycerol solutions in water, as expressed in Table I.

To create the initial condition where the two miscible phases are separated by a sharp, flat interface we used a flowing junction cell.⁴⁶ The cell is made up of two superimposed chambers, shown in light blue and violet in Fig. 5. In the initial stage, the two mixtures are injected continuously, the denser one in the bottom chamber and the lighter one in the top chamber. Injection occurs at room temperature (an average temperature of 27°C) through two annular porous septa, which favor a radial distribution of the inlet flow. The two mixtures come into contact at the mid-height of the cell. To maintain a sharp interface between them, the mixing fluid phases at the interface are continuously sucked out of the cell through a thin annular slit. Once the system is prepared in the condition just described, an experimental run can be started by interrupting the fluid flow at time $t = 0$, so that the two phases can diffuse one into the other through a free-diffusion process. Under these conditions, the concentration profile evolves as shown in Fig. 1. The cell contains a 3.36 cm thick sample, and the interface between the two mixtures is placed exactly in the middle, at a height of 1.68 cm.

To visualize concentration NEFs during the experiments, we used a quantitative dynamic shadowgraphy technique (Fig. 6) that is used in our laboratories both for studying NEFs^{43,50} and convection.^{51–54} The light is emitted by using a superluminescent

TABLE I. Index of measurements. Columns c_1 and c_2 are the initial bottom and top concentrations of glycerol, respectively. t_c identifies the diffusive time across the thickness of the sample, after which the system exits the free-diffusion regime. The other columns represent dimensionless times, relative to t_c , when measurements have been performed during the free-diffusion process.

c_1 (%)	c_2 (%)	t_c (s)	t_1	t_2	t_3	t_4	t_5	t_6	t_7	t_8	t_9	t_{10}	t_{11}	t_{12}
20	0	1.32×10^5	0.009	0.018	0.036	0.073	0.145	0.509						
40	0	1.60×10^5	0.008	0.015	0.034	0.060	0.120	0.357	0.490					
80	0	2.54×10^5	0.005	0.010	0.019	0.038	0.043	0.064	0.076	0.268	0.296	0.358	0.615	
90	0	2.92×10^5	0.004	0.008	0.016	0.033	0.051	0.066	0.107	0.220	0.240	0.250	1.130	1.180
95	0	3.16×10^5	0.004	0.008	0.015	0.030	0.060	0.191	0.244	0.425	0.801			
95	10	3.50×10^5	0.003	0.007	0.014	0.027	0.055	0.110	0.211	0.241	0.278	1.040	1.290	
95	20	3.92×10^5	0.003	0.006	0.012	0.049	0.098	0.195	0.216	0.303	0.418	0.542	0.737	0.877
95	40	5.14×10^5	0.002	0.005	0.009	0.013	0.019	0.026	0.037	0.086	0.150	0.194	0.340	0.810
95	80	1.26×10^6	0.002	0.004	0.008	0.015	0.030	0.055	0.063	0.130	0.170			

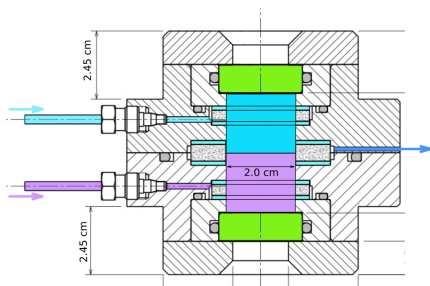


FIG. 5. Vertical cross section of the flowing junction cell. Green parts: sapphire plates that determine the upper and lower boundaries of the sample. Dotted regions: porous septa, needed for maintaining a radial inlet and outlet flow of the mixtures inside the cell. Cyan region: solution with the lowest concentration injected from the top inlet. Violet region: solution with the highest concentration injected from the bottom inlet. The presence of an annular slit at the interface where the two liquid phases adjoin allows us to avoid their mixing in the initial condition where fluid flow through the slit is allowed (blue outlet arrow).

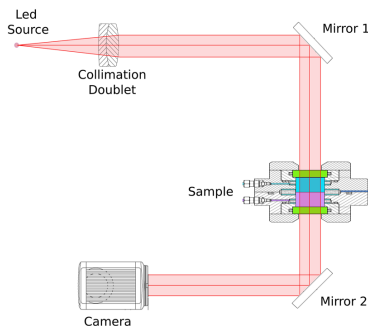


FIG. 6. Outline of the optical shadowgraph setup used during the experiments. The light beam emitted by the LED source is shown in red. After being collimated by the lens, the beam is reflected by a first mirror, passes through the sample and is reflected by a second mirror on the camera sensor. This folded optical configuration allowed us to optimize the space occupied by the setup.

light emitting diode (Superlum, SLD-MS-261-MP2-SM) with a wavelength of $\lambda = (675 \pm 13)$ nm, placed in the focal plane of an achromatic doublet with a focal length of $f = 150$ mm, which collimates the beam. Dynamic shadowgraph images are then acquired using a scientific CMOS camera (Hamamatsu C13440, ORCA-Flash 4.0 V3).

B. Dynamic shadowgraphy

Measurements are performed with dynamic shadowgraphy, a differential method based on the processing of shadowgraph

images previously subtracted one from the other to get rid of their static components.⁴³ The power spectrum of the difference between two images taken at different times allows us to calculate the Structure Function $P(\mathbf{q}, \Delta t) = \langle |I(\mathbf{q}, t) - I(\mathbf{q}, t + \Delta t)|^2 \rangle$, where the brackets identify a time average. Time averaging is done on a thousand pairs of images, taken at different instants of time but spaced by fixed Δt . Since the fluctuations are isotropic in the horizontal plane, the structure functions have a circular symmetry and have been averaged over the azimuth angle of the wave number,

$$P(q, \Delta t) = T(q)S(q) \cdot (1 - g(q, \Delta t)) + B(q) + \alpha \cdot \Delta t^2. \quad (32)$$

Here, the transfer function $T(q)$ characterizes the response of the optical system to a point-like perturbation of the refractive index inside the sample, and $S(q)$ is the static stratified structure factor. For our experiments, we have used an empirical expression for $T(q)$ borrowed from that determined by performing an accurate calibration of the transfer function using a reference sample.²⁰ $B(q)$ is the power spectrum of the background noise, and $g(q, t)$ is the stratified correlation function, defined by Eqs. (13) and (16), respectively. We had to add an empirical quadratic contribution in time because the system is in a non-stationary state, a condition that determines a slow drift of the optical background, which modifies the structure function with the term $\alpha \cdot \Delta t^2$.

In Sec. IV, the results of the interpolation of data $P(q, \Delta t)$ acquired using the shadowgraph technique with the UD, Schulz, and SE models are shown and compared with each other. Furthermore, our aim is to determine the thermophysical coefficients D_T , D_s , q_T , and q_s . The fit procedure consists of two steps. First, experimental data of $P(q, \Delta t)$ is interpolated at fixed q as a function of Δt to extract $A(q) = T(q)S(q)$, $B(q)$, and $\alpha(q)$; by fixing q , it is possible to consider these functions as simple parameters, the only independent variable being Δt . Second, we compute the q -independent parameters D_T , D_s , q_T , and q_s , by performing a new fit in two variables ($q, \Delta t$), where the parameters extracted from step one $A(q)$, $B(q)$, and $\alpha(q)$ are used as input parameters. This procedure allows us to use as little computing power as possible to increase the performance of the fit. The two steps are applied for the UD, Schulz, and SE models described in the previous paragraphs, which we will compare with each other: for the UD model, the correlation function $g(q, \Delta t)$ is described in Eq. (16); in the second step of the fit procedure, Γ and σ are written in the form Eqs. (25) and (26), respectively; for the Schulz model, the correlation function in Eq. (30) is used, having substituted $\sigma_n = \sigma/\Gamma$, for Γ and σ the dependence is still that expressed in Eqs. (25) and (26); for the SE model, the correlation function is that in Eq. (5) in which the trend of γ in Eq. (6) is substituted.

We have acquired data for samples prepared under different initial concentration conditions. Furthermore, to observe the evolution of the fluctuations during the evolution of the concentration profile, we acquired measurements at different times in the evolution of the system ($t_i = t/t_c$). The conditions for measurements and the timeline are summarized in Table I.

For each of these times and for each of the analyzed concentration pairs, two sets of 2000 images were acquired at two different frame rates (10 and 100 fps). Due to the wide range of relaxation rates contributing simultaneously to the signal, we have adopted a processing procedure that makes use of concatenated frame rates to

reduce the amount of images and make the datasets more manageable: a faster one, at 100 fps, to investigate the relaxation occurring at the smallest scales, and a slower one, at 10 fps.

Considering the rather large diffusion times in our experiments, the system can be assumed to be in quasi steady state conditions within one measurement run, i.e., at a given t_i time. The images taken have a resolution of 2048×2048 pixels at 16 bits. The whole procedure has been repeated three times at every initial concentration to check the repeatability of experiments and to enlarge the statistical sample of results.

IV. RESULTS

In this section, we present the experimental results and check the effectiveness of the UD correlation function by providing an accurate evaluation of the experimental parameters.

A. Validation of the model

A first important verification involves the validation of the effectiveness of the model correlation function Eq. (16) to fit the experimentally determined structure functions in the form described by Eq. (32). Figures 7(a)–7(c) show $P(q, \Delta t)$ for three different initial concentration conditions. Data acquired with the shadowgraph technique at three different wave numbers q are interpolated with the SE, UD, and Schulz models discussed in this work.

To evaluate the effectiveness of each model, it is useful to determine the residuals $R(q, \Delta t)$, defined as the difference between the expected value from each model and the measured data, normalized to the expected value. To better quantify the information contained in the residuals, we introduce the summation over all the time delays,

$$R(q) = \sum_{\Delta t} [R(q, \Delta t)]^2. \quad (33)$$

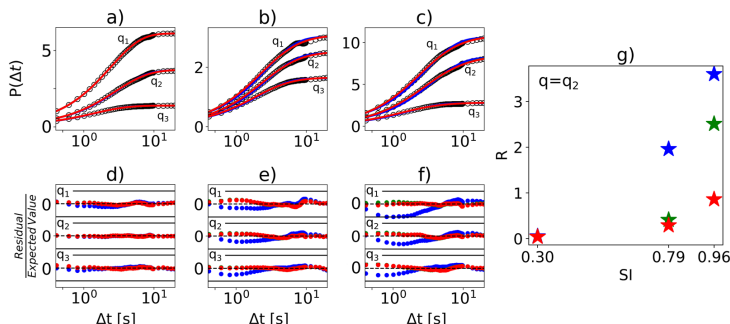


FIG. 7. (a)–(c): $P(q, \Delta t)$ as a function of Δt , at $q_1 = 140 \text{ cm}^{-1}$, $q_2 = 200 \text{ cm}^{-1}$, and $q_3 = 300 \text{ cm}^{-1}$; all measurements are made after 320 min from the start of the diffusion process, for different initial conditions: (a) $c_1 = 40\%$, $c_2 = 0\%$; (b) $c_1 = 80\%$, $c_2 = 0\%$; (c) $c_1 = 95\%$, $c_2 = 0\%$; black circles: $P(q, \Delta t)$; Red solid line: UD model; green solid line: Schulz model (not visible due to the close superposition to the red line); blue solid line: SE model; (d)–(f): relative residuals corresponding to the plots above. Dashed line: value 0; horizontal solid lines: $+0.1$ and -0.1 values; residuals resulting from different models are shown with the same color scheme as in the graphs above. (g): $R(q_2)$ for the three values of SI^{act} , plotted with the same color scheme as the other panels.

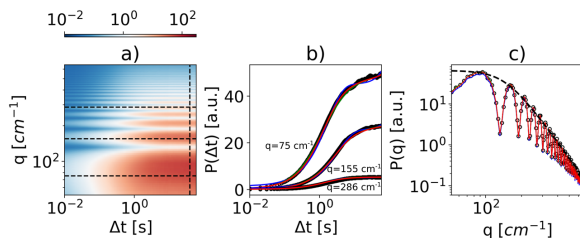


FIG. 8. (a) $P(q, \Delta t)$ (color scale indicated in the top bar) acquired for the initial condition $c_1 = 95\%$, $c_2 = 0\%$, after 320 min from the start of diffusion. (b) Black dots: Structure functions corresponding to the horizontal sections of panel (a). Red solid line: our two-variable model interpolating the data; green solid line: two-variable Schulz model; blue solid line: two-variable simple exponential model. (c) Black dots: section (a) at the vertical dashed line. Red continuous line: $S(q)T(q)$ of our two-variable model; green continuous line: $S(q)T(q)$ two-variable Schulz model; blue continuous line: $S(q)T(q)$ two-variable simple exponential model; Dashed black line: theoretical result for $S(q)$.

on all wave numbers in the observed range. Figure 8(a) shows the experimentally determined structure function $P(q, \Delta t)$ plotted in two dimensions as a function of all wave numbers q (vertical-axis) and of the delay time Δt (horizontal-axis) in the cases $c_1 = 95\%$ and $c_2 = 0\%$. In Fig. 8(b), it is possible to observe the function $P(\Delta t)$, at three different fixed q corresponding to the horizontal sections indicated by the dashed lines in Fig. 8(a), interpolated by the three models.

To provide an integrated parameter that gives overall information about the effectiveness of fit, we introduce the relative overall square residual averaged across all wave numbers and delay time ranges

$$R_m = \frac{1}{N} \sum_q \sum_{\Delta t} [R(q, \Delta t)]^2, \quad (34)$$

where N is the number of independent values of $R(q, \Delta t)$ used in the summations. For the case shown in the figure, we obtain $R_m = 0.0021$ for the UD model, $R_m = 0.0032$ for the Schulz model, and $R_m = 0.0037$ for the SE model.

TABLE II. Comparison between the relative mean square residuals obtained with the UD, Schulz, and SE models. c_1 and c_2 identify the concentrations of the bottom and top phases, respectively.

c_1 (%)	c_2 (%)	SI	R_m UD	R_m Schulz	R_m SE
20	0	0.132	0.0011	0.0011	0.0007
40	0	0.296	0.0014	0.0015	0.0017
80	0	0.795	0.0015	0.0016	0.0022
90	0	0.915	0.0021	0.0028	0.0032
95	0	0.956	0.0021	0.0032	0.0037
95	10	0.951	0.0020	0.0024	0.0030
95	20	0.943	0.0031	0.0037	0.0049
95	40	0.921	0.0028	0.0034	0.0055
95	80	0.674	0.0120	0.0120	0.0122

Table II shows the values of R_m for all the initial conditions analyzed. These data confirm that for small differences in concentration, the three models perform equivalently. As the difference between c_1 and c_2 increases, the difference between the models becomes more and more evident.

Finally, the static power spectrum obtained with the three models can be observed in Fig. 8(c). As predicted by the numerical calculations and detailed in the previous chapters, the UD, Schulz, and SE models show the same result for the static part. In the figure, the three static curves representing the term $S(q)T(q)$ are perfectly superimposed and in excellent agreement with the experimental $P(q, \Delta t)$ for $\Delta t = 90$ s.

B. Thermophysical parameters and discussion

The two-dimensional fitting procedure adopted in this work allows us to determine a single value of the average diffusion coefficient and of its dispersion for each experimental run. For times $t < t_c$, the system evolves under free-diffusion conditions, and the concentrations at the boundaries of the sample does not change in time. Under these conditions, the time evolution of the concentration profile does not influence significantly the values of D_T and D_σ , allowing the diffusion coefficients to be averaged over all tests and times for each experimental concentration. The fitting of the experimental data allows us to estimate the values of D_M and D_m , and, using Eqs. (21) and (23), to evaluate D_σ and D_T , which are plotted in Fig. 9(a) as a function of the average concentration. To achieve a meaningful statistical relevance of the results, we have performed three measurements for each of the nine couples of concentrations shown in Table I.

Experimental data are compared with the theoretical values calculated from Eqs. (21) and (23), using the theoretical values of the diffusion coefficients obtained with the empirical modeling of Eq. (8). It can be observed that the average diffusion coefficient D_T decreases as the average concentration increases, in agreement with the theoretical prediction (dashed line), although the experimental values are systematically larger than the theoretical ones. The trend for the dispersion of the diffusion coefficient D_σ is also in

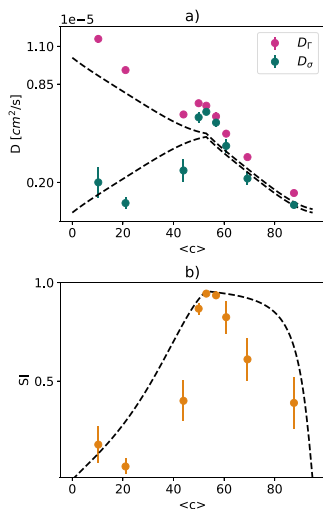


FIG. 9. (a) Values of D_T and D_σ as a function of the average mass concentration of the system. (b) Values of SI as a function of the average mass concentration of the system. For both panels, the error bars are the standard deviations determined from the three repetitions of the experiments, which in some cases are smaller than the point size; the dashed black lines represent the theoretical predictions for D_T , D_σ , and SI .

agreement with the theoretical predictions, and a peak at the maximum concentration difference ($c_1 = 0$, $c_2 = 0.95$) is observed, even if the experimental data are noisy and differ substantially from the predicted ones. This difference can also be evidenced by comparing the predicted stratification index at each average concentration, with the experimental value, Fig. 9(b). Although our Fick diffusivity data do not match exactly with the reference ones on the empirical concentration-dependence of the diffusion coefficient at 298 K derived from Bauchaudy *et al.*,⁴⁰ see Eq. (8), the trend of D_T , D_σ , and SI as a function of the average mass fraction of glycerol are in very good agreement with those derived from reference data. The deviations observed in Fig. 9 can be associated with the slight difference in the temperature as well as the correlation itself. As shown in the literature, one can expect deviations up to 70% between Fick diffusivity data at large mass fractions of glycerol.^{55–58} Propagating these deviations in the reference values depicted by the dashed lines on Fig. 9, not shown for legibility purposes, will lead to matching diffusivity and SI data across the complete range of mass fractions of glycerol used in our study.

Analogously to the analysis performed for D_T and D_σ , it is possible to extract from the experimental data the values of q_T and q_σ defined in Eqs. (22) and (24), which are a linear combination of the roll-off wave numbers q_m and q_M for the largest and smallest concentrations present inside the sample. The investigation of these

two parameters allows us to characterize the influence of gravity on NEFs in the presence of a significant stratification of the sample. Quite interestingly, we notice that results for time evolution of the roll-off wave number q_i obtained with all the initial conditions investigated in this work can be scaled onto a single curve, once they are normalized with an arbitrary constant, Fig. 10. To understand the physical origin of this common behavior, we notice that the only time-dependent term in Eq. (2) is the gradient ∇c , which decreases with time proportionally to $t^{-1/2}$. Therefore, we expect that q_T and q_σ evolve in time according to the following expressions:¹⁸

$$q_T = a_T \cdot \left(\frac{t}{t_c}\right)^{-1/8}, \quad (35)$$

$$q_\sigma = a_\sigma \cdot \left(\frac{t}{t_c}\right)^{-1/8}, \quad (36)$$

where a_T and a_σ are two characteristic wave numbers that can be obtained by interpolating the time evolution of the roll-off wave numbers with Eqs. (35) and (36) for each experimental run. One can appreciate that the measured values of $q_T(t)/a_T$ are well approximated by the theoretical curve, providing an indication of the consistency of the interpretative model proposed by us. On the other hand, the trend of $q_\sigma(t)/a_\sigma$ follows the predictions only for large concentration differences (0 vs 90, 0 vs 95, 10 vs 95, and 20 vs 95), while for the small ones, the values are very noisy, Fig. 10(b). This result can be understood by taking into account that q_σ represents the dispersion of roll-off wave numbers, which differs significantly from zero only in the presence of a significant stratification of the sample. This condition is met by the experimental results clustered around the theoretical prediction in Fig. 10(b). Under all the other experimental conditions, the value of q_σ should be close to zero, and the fitting procedure becomes very noisy because, under these conditions, q_σ is not a relevant parameter to describe the system.

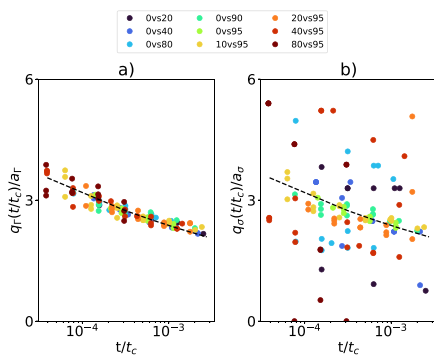


FIG. 10. (a) q_T/a_T , and (b) q_σ/a_σ , plotted as a function of time. Different colors correspond to measurements performed under different initial concentration conditions (top legend). The dashed black line represents the theoretical prediction $t^{-1/8}$.

V. CONCLUSIONS

Non-equilibrium fluctuations in free diffusion under non-ideal conditions, such as transient processes and large concentration differences, are characterized by a wide distribution of relaxation times determined by the stratification of the sample. We propose a model based on a uniform distribution of the relaxation times that allows us to describe the dynamics of non-equilibrium fluctuations during these processes. The comparison of the uniform distribution model with the Schulz model commonly applied in dynamic light scattering to characterize the polydispersity of samples confirms the better performance of the UD model in the presence of a wide range of relaxation times determined by a strong stratification. For small concentration differences, in the presence of a moderate range of relaxation times, the effectiveness of the three models is comparable. The investigation of the influence of gravity on the dynamics of non-equilibrium fluctuations shows that results obtained under all the stratification conditions can be described by a universal power law that rules the time evolution of the roll-off wave number below which the fluctuations are affected by gravity significantly.

A notable case where the proposed approach can be useful is the investigation of non-equilibrium fluctuations during a free-diffusion process occurring between two phases of a binary liquid mixture close to a consolute critical point,^{18,59,60} where the diffusion coefficient of the mixture exhibits a strong dependence on the concentration. The conceptual framework proposed in this work could also be applied to other types of fluctuations in stratified media, such as temperature fluctuations occurring in fluids under the action of a temperature gradient. Indeed, large temperature gradients could affect thermodynamic coefficients, such as the thermal diffusion coefficient and viscosity, resulting in a dispersion of relaxation times for non-equilibrium temperature fluctuations similar to that discussed in this paper.

ACKNOWLEDGMENTS

This work was supported by the European Space Agency through the CORA-MAP TechNES project, Contract No. 4000128933. This work was supported by the CNES, focused on the Giant Fluctuations future mission on the ISS. This research was partially carried out under the framework of the E2S UPPA Hub Newpores and Industrial Chair CO2ES supported by the Investissements d'Avenir French program managed by ANR (No. ANR16IDEX0002).

AUTHOR DECLARATIONS

Conflict of Interest

The authors have no conflicts to disclose.

Author Contributions

Stefano Castellini: Conceptualization (supporting); Data curation (equal); Formal analysis (lead); Investigation (lead); Methodology (equal); Software (equal); Validation (equal); Visualization (lead); Writing – original draft (lead); Writing – review & editing (equal).

Marina Carpineti: Conceptualization (supporting); Formal analysis (supporting); Funding acquisition (supporting); Investigation (supporting); Methodology (equal); Supervision (supporting); Validation (equal); Visualization (supporting); Writing – original draft (supporting); Writing – review & editing (equal). **Cédric Giraudet:** Conceptualization (supporting); Data curation (equal); Formal analysis (supporting); Investigation (supporting); Supervision (supporting); Validation (supporting); Writing – original draft (supporting); Writing – review & editing (supporting). **Fabrizio Croccolo:** Conceptualization (lead); Data curation (supporting); Formal analysis (supporting); Funding acquisition (lead); Investigation (supporting); Methodology (equal); Resources (lead); Software (supporting); Supervision (lead); Validation (equal); Visualization (supporting); Writing – original draft (supporting); Writing – review & editing (equal). **Alberto Vailati:** Conceptualization (lead); Data curation (equal); Formal analysis (supporting); Funding acquisition (equal); Investigation (supporting); Methodology (equal); Resources (supporting); Supervision (lead); Validation (equal); Visualization (supporting); Writing – original draft (lead); Writing – review & editing (equal).

DATA AVAILABILITY

The data that support the findings of this study are available within the article.

REFERENCES

- ¹J. M. Ortiz de Zárate and J. V. Sengers, *Hydrodynamic Fluctuations in Fluids and Fluid Mixtures* (Elsevier, Amsterdam, 2006).
- ²F. Croccolo, J. M. Ortiz de Zárate, and J. V. Sengers, “Non-local fluctuation phenomena in liquids,” *Eur. Phys. J. E* **39**, 125 (2016).
- ³T. R. Kirkpatrick, E. G. D. Cohen, and J. R. Dorfman, “Fluctuations in a nonequilibrium steady state: Basic equations,” *Phys. Rev. A* **26**, 950–971 (1982).
- ⁴T. R. Kirkpatrick, E. G. D. Cohen, and J. R. Dorfman, “Light scattering by a fluid in a nonequilibrium steady state. I. Small gradients,” *Phys. Rev. A* **26**, 972–994 (1982).
- ⁵T. R. Kirkpatrick, E. G. D. Cohen, and J. R. Dorfman, “Light scattering by a fluid in a nonequilibrium steady state. II. Large gradients,” *Phys. Rev. A* **26**, 995–1014 (1982).
- ⁶D. Ronis and I. Procaccia, “Nonlinear resonant coupling between shear and heat fluctuations in fluids far from equilibrium,” *Phys. Rev. A* **26**, 1812 (1982).
- ⁷R. Schmitz and E. G. D. Cohen, “Fluctuations in a fluid under a stationary heat flux. II. Slow part of the correlation matrix,” *J. Stat. Phys.* **40**, 431–482 (1985).
- ⁸R. Schmitz, “Fluctuations in nonequilibrium fluids,” *Phys. Rep.* **171**, 1–58 (1988).
- ⁹R. Schmitz, “Fluctuations in a nonequilibrium colloidal suspension,” *Physica A* **206**, 25–57 (1994).
- ¹⁰B. M. Law, R. W. Gammon, and J. V. Sengers, “Light-scattering observations of long-range correlations in a nonequilibrium liquid,” *Phys. Rev. Lett.* **60**, 1554–1557 (1988).
- ¹¹B. M. Law and J. V. Sengers, “Fluctuations in fluids out of thermal equilibrium,” *J. Stat. Phys.* **57**, 531–547 (1989).
- ¹²B. M. Law, P. N. Segrè, R. W. Gammon, and J. V. Sengers, “Light-scattering measurements of entropy and viscous fluctuations in a liquid far from thermal equilibrium,” *Phys. Rev. A* **41**, 816–824 (1990).
- ¹³P. N. Segrè, R. W. Gammon, J. V. Sengers, and B. M. Law, “Rayleigh scattering in a liquid far from thermal equilibrium,” *Phys. Rev. A* **45**, 714–724 (1992).
- ¹⁴P. N. Segrè, R. W. Gammon, and J. V. Sengers, “Light-scattering measurements of nonequilibrium fluctuations in a liquid mixture,” *Phys. Rev. E* **47**, 1026–1034 (1993).

- ¹⁵W. B. Li, P. N. Segrè, R. W. Gammon, and J. V. Sengers, "Small-angle Rayleigh scattering from nonequilibrium fluctuations in liquids and liquid mixtures," *Physica A* **204**, 399 (1994).
- ¹⁶W. B. Li, P. N. Segrè, R. W. Gammon, and J. V. Sengers, "Nonequilibrium fluctuations in liquids and liquid mixtures subjected to a stationary temperature gradient," *J. Phys.: Condens. Matter* **6**, A119 (1994).
- ¹⁷A. Vailati and M. Giglio, "q divergence of nonequilibrium fluctuations and its gravity-induced frustration in a temperature stressed liquid mixture," *Phys. Rev. Lett.* **77**, 1484–1487 (1996).
- ¹⁸A. Vailati and M. Giglio, "Giant fluctuations in a free diffusion process," *Nature* **390**, 262–265 (1997).
- ¹⁹C. J. Takacs, A. Vailati, R. Cerbino, S. Mazzoni, M. Giglio, and D. S. Cannell, "Thermal fluctuations in a layer of liquid CS₂ subjected to temperature gradients with and without the influence of gravity," *Phys. Rev. Lett.* **106**, 244502 (2011).
- ²⁰A. Vailati, R. Cerbino, S. Mazzoni, C. J. Takacs, D. S. Cannell, and M. Giglio, "Fractal fronts of diffusion in microgravity," *Nat. Commun.* **2**, 290 (2011).
- ²¹F. Crococo, C. Giraudet, H. Bataller, R. Cerbino, and A. Vailati, "Shadowgraph analysis of non-equilibrium fluctuations for measuring transport properties in microgravity in the gRadflex experiment," *Microgravity Sci. Technol.* **28**, 467 (2016).
- ²²G. Eyink and A. Jafari, "High Schmidt-number turbulent advection and giant concentration fluctuations," *Phys. Rev. Res.* **4**, 023246 (2022).
- ²³G. Eyink and A. Jafari, "The Kraichnan model and non-equilibrium statistical physics of diffusive mixing," *Ann. Henri Poincaré* (published online 2022).
- ²⁴F. B. Usabiaga, J. B. Bell, R. Delgado-Buscalioni, A. Donev, T. G. Fai, B. E. Griffith, and C. S. Peskin, "Staggered schemes for fluctuating hydrodynamics," *Multiscale Model. Simul.* **10**, 1369 (2012).
- ²⁵I. Srivastava, D. R. Ladiges, A. J. Nonaka, A. L. Garcia, and J. B. Bell, "Staggered scheme for the compressible fluctuating hydrodynamics of multispecies fluid mixtures," *Phys. Rev. E* **107**, 015305 (2023).
- ²⁶P. Baaske, H. Bataller, M. Braibanti, M. Carpineti, R. Cerbino, F. Crococo, A. Donev, W. Köhler, J. M. Ortiz de Zárate, and A. Vailati, "The NEUF-DIX space project—Non-Equilibrium Fluctuations during Diffusion in complex liquids," *Eur. Phys. J. E* **39**, 119 (2016).
- ²⁷A. Vailati, P. Baaske, H. Bataller, S. Bolis, M. Braibanti, M. Carpineti, R. Cerbino, F. Crococo, J.-L. Dewandel, A. Donev, L. García-Fernández, F. Giavazzi, R. Haslinger, S. Hens, M. Knauer, W. Köhler, E. Kufner, J. M. Ortiz de Zárate, J. Peeters, C. J. Schwarz, I. Silkina, S. Xu, and D. Zapf, "Giant fluctuations induced by thermal diffusion in complex liquids," *Microgravity Sci. Technol.* **32**, 873–887 (2020).
- ²⁸R. Cerbino and A. Vailati, "Near-field scattering techniques: Novel instrumentation and results from time and spatially resolved investigations of soft matter systems," *Curr. Opin. Colloid Interface Sci.* **14**, 416 (2009).
- ²⁹M. Giglio, M. Carpineti, and A. Vailati, "Space intensity correlations in the near field of the scattered light: A direct measurement of the density correlation function," *Phys. Rev. Lett.* **85**, 1416–1419 (2000).
- ³⁰F. Crococo, D. Brogioli, A. Vailati, M. Giglio, and D. S. Cannell, "Nondiffusive decay of gradient-driven fluctuations in a free-diffusion process," *Phys. Rev. E* **76**, 041112 (2007).
- ³¹R. Cerbino and V. Trappe, "Differential dynamic microscopy: Probing wave vector dependent dynamics with a microscope," *Phys. Rev. Lett.* **100**, 188102 (2008).
- ³²A. Vailati and M. Giglio, "Nonequilibrium fluctuations in time-dependent diffusion processes," *Phys. Rev. E* **58**, 4361–4371 (1998).
- ³³D. Zapf, J. Kantelhardt, and W. Köhler, "Nonlinearities in shadowgraphy experiments on non-equilibrium fluctuations in polymer solutions," *Eur. Phys. J. E* **45**, 40 (2022).
- ³⁴D. Brogioli, F. Crococo, and A. Vailati, "Correlations and scaling properties of non-equilibrium fluctuations in liquid mixtures," *Phys. Rev. E* **94**, 022142 (2016).
- ³⁵D. Brogioli, A. Vailati, and M. Giglio, "Giant fluctuations in diffusion processes," *J. Phys.: Condens. Matter* **12**, A39–A46 (2000).
- ³⁶F. Crococo, D. Brogioli, and A. Vailati, "Cylindrical flowing-junction cell for the investigation of fluctuations and pattern-formation in miscible fluids," *Rev. Sci. Instrum.* **90**, 085109 (2019).
- ³⁷B. J. Berne and R. Pecora, *Dynamic Light Scattering: With Applications to Chemistry, Biology, and Physics* (Courier Dover Publications, 2000).
- ³⁸A. G. Mailer, P. S. Clegg, and P. N. Pusey, "Particle sizing by dynamic light scattering: Non-linear cumulant analysis," *J. Phys.: Condens. Matter* **27**, 145102 (2015).
- ³⁹L. D. Landau and E. M. Lifshitz, *Fluid Mechanics* (Pergamon, New York, 1959).
- ⁴⁰A. Bouchaud, C. Lousset, and J.-B. Salmon, "Steady microfluidic measurements of mutual diffusion coefficients of liquid binary mixtures," *AIChE J.* **64**, 358–366 (2018).
- ⁴¹N.-S. Cheng, "Formula for the viscosity of a glycerol-water mixture," *Ind. Eng. Chem. Res.* **47**, 3285–3288 (2008).
- ⁴²F. Crococo, L. García-Fernández, H. Bataller, A. Vailati, and J. M. Ortiz de Zárate, "Propagating modes in a binary liquid mixture under thermal stress," *Phys. Rev. E* **99**, 012602 (2019).
- ⁴³F. Crococo, D. Brogioli, A. Vailati, M. Giglio, and D. S. Cannell, "Effect of gravity on the dynamics of nonequilibrium fluctuations in a free-diffusion experiment," *Ann. N. Y. Acad. Sci.* **1077**, 365 (2006).
- ⁴⁴S. W. Provencher, "CONTIN: A general purpose constrained regularization program for inverting noisy linear algebraic and integral equations," *Comput. Phys. Commun.* **27**, 229–242 (1982).
- ⁴⁵A. Scotti, W. Liu, J. S. Hyatt, E. S. Herman, H. S. Choi, J. W. Kim, L. A. Lyon, U. Gasser, and A. Fernandez-Nieves, "The CONTIN algorithm and its application to determine the size distribution of microgel suspensions," *J. Chem. Phys.* **142**, 234905 (2015).
- ⁴⁶G. Cerchiari, F. Crococo, F. Cardinaux, and F. Scheffold, "Note: Quasi-real-time analysis of dynamic near field scattering data using a graphics processing unit," *Rev. Sci. Instrum.* **83**, 106101 (2012).
- ⁴⁷M. Norouziadeh, M. Chraga, G. Cerchiari, and F. Crococo, "The modern strukturer: Increased performance for calculating the structure function," *Eur. Phys. J. E* **44**, 146 (2021).
- ⁴⁸P. N. Pusey, D. E. Koppel, D. E. Schaefer, R. D. Camerini-Otero, and S. H. Koenig, "Intensity fluctuation spectroscopy of laser light scattered by solutions of spherical viruses. R17, Qbeta, BSV, PM2, and T7. I. Light-scattering technique," *Biochemistry* **13**, 952–960 (1974).
- ⁴⁹B. J. Frisken, "Revisiting the method of cumulants for the analysis of dynamic light scattering data," *Appl. Opt.* **40**, 4087 (2001).
- ⁵⁰F. Crococo, F. Scheffold, and H. Bataller, "Mass transport properties of the tetrahydrofuran/*n*-dodecane mixture measured by investigating non equilibrium fluctuations," *C. R. Mec.* **341**, 378 (2013).
- ⁵¹R. Cerbino, S. Mazzoni, A. Vailati, and M. Giglio, "Scaling behavior for the onset of convection in a colloidal suspension," *Phys. Rev. Lett.* **94**, 064501 (2005).
- ⁵²S. Mazzoni, F. Giavazzi, R. Cerbino, M. Giglio, and A. Vailati, "Mutual Voronoi tessellation in spoke pattern convection," *Phys. Rev. Lett.* **100**, 188104 (2008).
- ⁵³F. Crococo, F. Scheffold, and A. Vailati, "Effect of a marginal inclination on pattern formation in a binary liquid mixture under thermal stress," *Phys. Rev. Lett.* **111**, 014502 (2013).
- ⁵⁴P. Fruton, A. Nauruzbaeva, H. Bataller, C. Giraudet, A. Vailati, and F. Crococo, "Convective dissolution of carbon dioxide into brine in a three-dimensional free medium," *Phys. Rev. Fluids* **8**, 023503 (2023).
- ⁵⁵Y. Nishijima and G. Oster, "Diffusion in glycerol-water mixture," *Bull. Chem. Soc. Jpn.* **33**, 1649–1651 (1960).
- ⁵⁶G. Ternström, A. Sjöstrand, G. Aly, and Å. Jernqvist, "Mutual diffusion coefficients of water + ethylene glycol and water + glycerol mixtures," *J. Chem. Eng. Data* **41**, 876–879 (1996).
- ⁵⁷G. D'Errico, O. Ortona, F. Capuano, and V. Vitagliano, "Diffusion coefficients for the binary system glycerol + water at 25 °C. A velocity correlation study," *J. Chem. Eng. Data* **49**, 1665–1670 (2004).
- ⁵⁸M. H. Rausch, A. Heller, and A. P. Fröba, "Binary diffusion coefficients of glycerol-water mixtures for temperatures from 323 to 448 K by dynamic light scattering," *J. Chem. Eng. Data* **62**, 4364–4370 (2017).
- ⁵⁹P. Cicuta, A. Vailati, and M. Giglio, "Capillary-to-bulk crossover of nonequilibrium fluctuations in the free diffusion of a near-critical binary liquid mixture," *Appl. Opt.* **40**, 4140–4145 (2001).
- ⁶⁰F. Giavazzi, A. Fornasier, A. Vailati, and R. Cerbino, "Equilibrium and non-equilibrium concentration fluctuations in a critical binary mixture," *Eur. Phys. J. E* **39**, 103 (2016).